A Model of bubble nucleation efficiency for bubble chamber detector

by

Xiang Li

A thesis submitted in partial fulfillment of the requirements for the degree of

Master of Science

Department of Physics
University of Alberta

© Xiang Li, 2023

Abstract

Bubble chambers using fluorocarbons or noble liquids gases are promising tools for detecting low-energy nuclear recoils caused by the elastic scattering of weakly interacting massive particles (WIMPs), a type of dark matter. These chambers comprise a vessel filled with a superheated liquid, which is controlled in terms of pressure and temperature. Bubble formation occurs when the energy deposition surpasses a specific threshold defined by the "heat-spike" Seitz Model. The efficiency of bubble nucleation from low-energy nuclear recoils in superheated liquids is a crucial factor in interpreting results obtained from direct searches for WIMPs as dark matter. This study aims to develop a physics model capable of explaining the observed disparities between experimental outcomes and the current Seitz model. Molecular dynamics simulations were utilized to investigate the bubble nucleation threshold, and a Monte Carlo simulation employing SRIM was performed to obtain the energy transfer in the target medium. The model also incorporates Lindhard's theory to enhance accuracy and improve predictions of bubble nucleation efficiency. By applying nucleation efficiency, we can estimate the cross-section exclusion limit for experiments. The model has been tested with existing experimental data and shows similar detector responses.

Preface

The research presented in this thesis was completed by Xiang Li, with contributions towards bubble chamber technology in general, including PICO and SBC experiments. The work was done under the guidance and supervision of Dr. Marie-Cécile Piro at the University of Alberta. My colleague Daniel Durnford conducted experimental analysis of C_3F_8 in the PICO-60 and liquid xenon in the SBC bubble chamber. The molecular dynamic simulation code was created using the same method used by Tetiana Kozynets and builds upon previous studies done by Freyja Wang.

Acknowledgements

Two years of Master study ran fast, and I couldn't have these work done without many people's help. First and foremost, I extend my deepest appreciation to my supervisor, Dr. Marie-Cécile Piro, for her unwavering support and guidance throughout this journey. Her acceptance as my master's supervisor not only gave me the opportunity to continue my academic pursuits but also inspired my passion for continuing studying physics. I am grateful for her invaluable guidance and the perfect balance of encouragement and challenge she provided. I appreciate the contributions made by Tetiana Kozynets and Freyja Wang in their previous work, which facilitated the commencement of my current study. I would also like to thank my colleague, Daniel Durnford, for his suggestions and encouragement during this time. I am grateful to the entire Piro Group for their support and engaging discussions. The collaborative and stimulating environment within the group has been instrumental in shaping my research. I would like to acknowledge Simon Gravelle from Grenoble Alpes University for his assistance and troubleshooting in using molecular dynamics simulations in LAMMPS. His expertise was invaluable in overcoming the challenges I encountered. I extend my gratitude to the McDonald Institute for funding our research and providing the necessary resources to carry out this study. I would like to acknowledge the Digital Research Alliance of Canada (https://www.alliancecan.ca) for their essential support in conducting the simulations for this research.

Last but not least, I would like to express my heartfelt thanks to my friends, both online and in real life, for their unwavering support during challenging times. I am especially grateful to my parents, whose unwavering belief in me and support

have been the foundation of my academic journey. Their support enabled me to come to Canada, opening my eyes to a vast and expansive world of opportunities and possibilities.

Contents

List of Tables

List of Figures

Abbreviations

ADMX Axion Dark Matter eXperiment.

BCA Binary Collision Approximation.

CDMS Cryogenic Dark Matter Search.

CG Coarse-Graining.

CMB Cosmic Microwave Background.

COUPP Chicagoland Observatory for Underground Particle Physics.

DM Dark Matter.

LAr Liquid Argon.

LHC Large Hadron Collider.

LXe Liquid Xenon.

MC Monte Carlo.

MCMC Markov Chain Monte Carlo.

MD Molecular Dynamics.

MOND Modified Newtonian Dynamics.

NEST Noble Element Simulation Technique.

PICASSO Project In CAnada to Search for Supersymmetric Objects.

PICO Merger of two similar experiments, PICASSO and COUPP.

PMT Photomultiplier tubes.

QCD Quantum Chromodynamics.

SBC Scintillating Bubble Chamber.

SD Spin-Dependent.

SI Spin-Independent.

SRIM Stopping and Range of Ions in Matter.

TRIM Transport of Ions in Matter.

WIMP Weakly Interacting Massive Particle.

Chapter 1

Introduction

One of the most challenging mysteries for physicists to solve is the existence and nature of dark matter. Although its presence is elusive, dark matter's gravitational influence on galaxies and the large-scale structure of the universe are undeniable. Its abundance, estimated to account for about 85% of the matter in the universe, has profound implications for our understanding of fundamental physics. Weakly Interacting Massive Particles (WIMPs) are among the most intriguing candidates for dark matter particles. These hypothetical particles, predicted by various theoretical frameworks, have the potential to elucidate supersymmetric models. Direct detection experiments use a variety of technologies to search for WIMPs with low-energy thresholds. A detailed discussion on WIMPs and their detection will be presented in Chapter. 2.

The primary focus of this work revolves around the bubble chamber detector technology. In Chapter 3, the principle of operation and an overview of bubble chamber experiments will be introduced. Notably, the disparity between conventional bubble nucleation theory and experimental observations serves as the motivation for the present study, which aims to understand the underlying factors affecting the efficiency of bubble nucleation.

This study employs molecular dynamics (MD) simulations to investigate bubble formation at the microscopic scale. Chapter. 4 will provide an in-depth analysis of the

simulation methodology, including detailed descriptions of the simulations conducted and the resulting outcomes. Furthermore, in Chapter 5, Monte Carlo (MC) simulations will be used to estimate the energy transfer from nuclear recoils to the target medium as recoiling ions travel through it. By combining the results from both MD and MC simulations, we can determine the bubble nucleation efficiency as a function of nuclear recoil energy. The outcomes of this modeling approach are found to be consistent with experimental analysis, which is presented in Chapter.6.

Chapter 2

Dark matter overview

Dark matter has been an intriguing topic in astrophysics and cosmology for several decades. The concept of dark matter originated in the 1930s, when Swiss astronomer Fritz Zwicky [1] noted that the observable mass of galaxy clusters couldn't explain their gravitational behavior.

The term "dark matter" refers to matter that's invisible to telescopes because it doesn't interact with light or other forms of electromagnetic radiation. However, its gravitational effects on visible matter, like stars and galaxies, allow us to infer its existence.

Over the years, several theoretical models have been proposed to explain what dark matter is. One of the most popular theories suggests that dark matter could be made up of exotic particles beyond the standard model, such as Weakly Interacting Massive Particles (WIMPs) or axions [2]. Despite extensive research, the true nature of dark matter remains unknown.

To solve this mystery, various experimental techniques have been developed. One such technique is indirect detection, which involves detecting cosmic rays such as gamma and neutrino rays that result from dark matter annihilation and decay. Another approach is to look for direct detection evidence of dark matter particles in laboratory experiments. This area of research is constantly evolving, and remains an active field in both astro and particle physics. In this chapter, readers will gain

an overview of the history of dark matter evidence discovery, explore the theoretical models and candidates, and delve into the latest developments in direct detection of dark matter, with a particular focus on WIMPs [3].

2.1 Evidence

The existence of dark matter has been inferred from its gravitational effects on visible matter, such as stars and galaxies. Several pieces of evidence that indicate the presence of dark matter in the universe. In this subchapter, we will discuss some of the most compelling evidence, including galaxy rotation curves, gravitational lensing, and the cosmic microwave background.

2.1.1 Galaxy rotation curves

One of the earliest pieces of evidence for dark matter came from the study of galaxy rotation curves. The rotation curve of a galaxy is a measure of its orbital velocity as a function of distance from the center. According to Newton's laws of motion, the orbital velocity of stars and gas in a galaxy should decrease as the distance from the center increases. However, observations of galaxy rotation curves showed that the orbital velocity remains constant or even increases with distance from the center. As Fig. 2.1 shows, the rotational velocity distributions of galaxies do not match the observable matter (disk and gas) at increasing galactic radii. This indicates the presence of extra invisible mass (halo) that contributes to the galaxies' rotational velocity. Moreover, the invisible mass in the galaxy is more than can be accounted for by visible matter alone. This extra, invisible mass is believed to be dark matter [4].

The observed phenomenon is not limited to individual galaxies; rotation curves of galaxies within galaxy clusters also indicate the presence of dark matter [4]. In some cases, the total mass of dark matter inferred from the rotation curve outweighs the visible mass by a factor of up to 10 to 1 [6]. While the rotation curve is a crucial piece

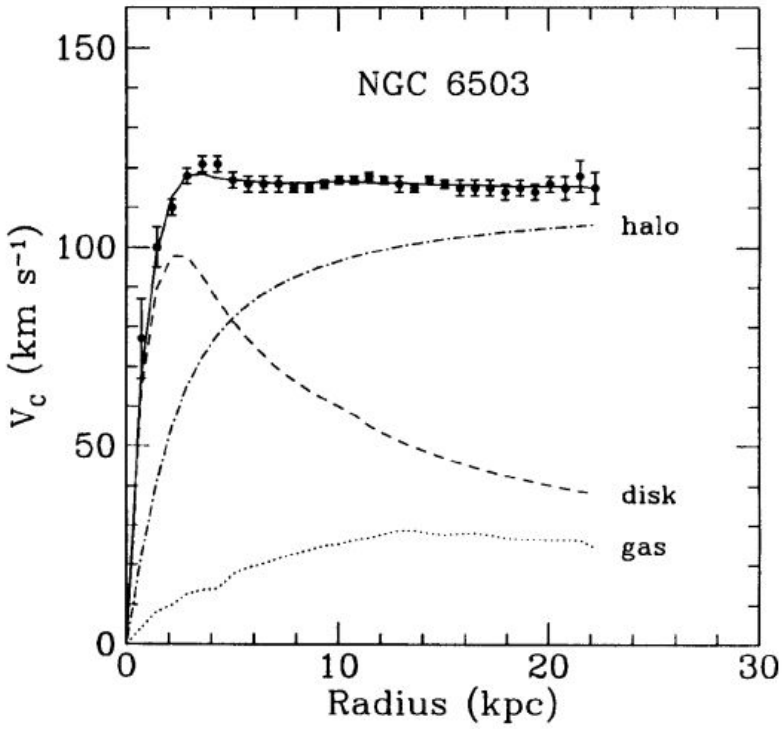

Figure 2.1: Observed rotation speed of the NGC 6503 galaxy according to the distance from its center compared to that predicted by the theory [5]. The disk component represents the visible mass contribution to the rotational velocity, while the gas component represents the interstellar gas contribution. The halo component represents the contribution of the elusive dark matter halo.

of evidence in the search for dark matter, it is just one of many methods used to infer its presence in the universe. In addition to rotation curves, other observation such as gravitational lensing and the cosmic microwave background have provided additional independent evidence for the existence of dark matter. These complementary approaches have allowed scientists to better understand the elusive nature of dark matter and its role in shaping the structure of the cosmos.

2.1.2 Gravitational lensing

Gravitational lensing is one of the most convincing pieces of evidence for the existence of dark matter [7]. This phenomenon occurs when the path of light from a distant object is bent by the gravitational field of a massive object, such as a galaxy. The degree of bending is directly proportional to the mass of the object, enabling scientists to use gravitational lensing to infer the distribution of matter in the intervening galaxy cluster, including the distribution of elusive dark matter. The observed lensing effects are consistent with the presence of dark matter around galaxies and in galaxy clusters [8]. The distribution of dark matter can be mapped out by measuring the lensing effects on the light from background galaxies. These maps have revealed that dark matter is distributed in a web-like structure, forming large filaments and clusters of galaxies [9]. As depicted in Fig. 2.2, the galactic dark matter halo mass creates gravitational lensing that amplifies further galaxies, including those that were observable during a time when the universe was less than a billion years old [10].

Gravitational lensing has also been used to study the properties of dark matter. By comparing the lensing effects with computer simulations, scientists can infer the properties of dark matter, such as its density and clustering properties [11]. One interesting result from these studies is that dark matter appears to be less concentrated in the centers of galaxies than previously thought, which has led to new questions about the nature of dark matter and its interactions with visible matter [12].

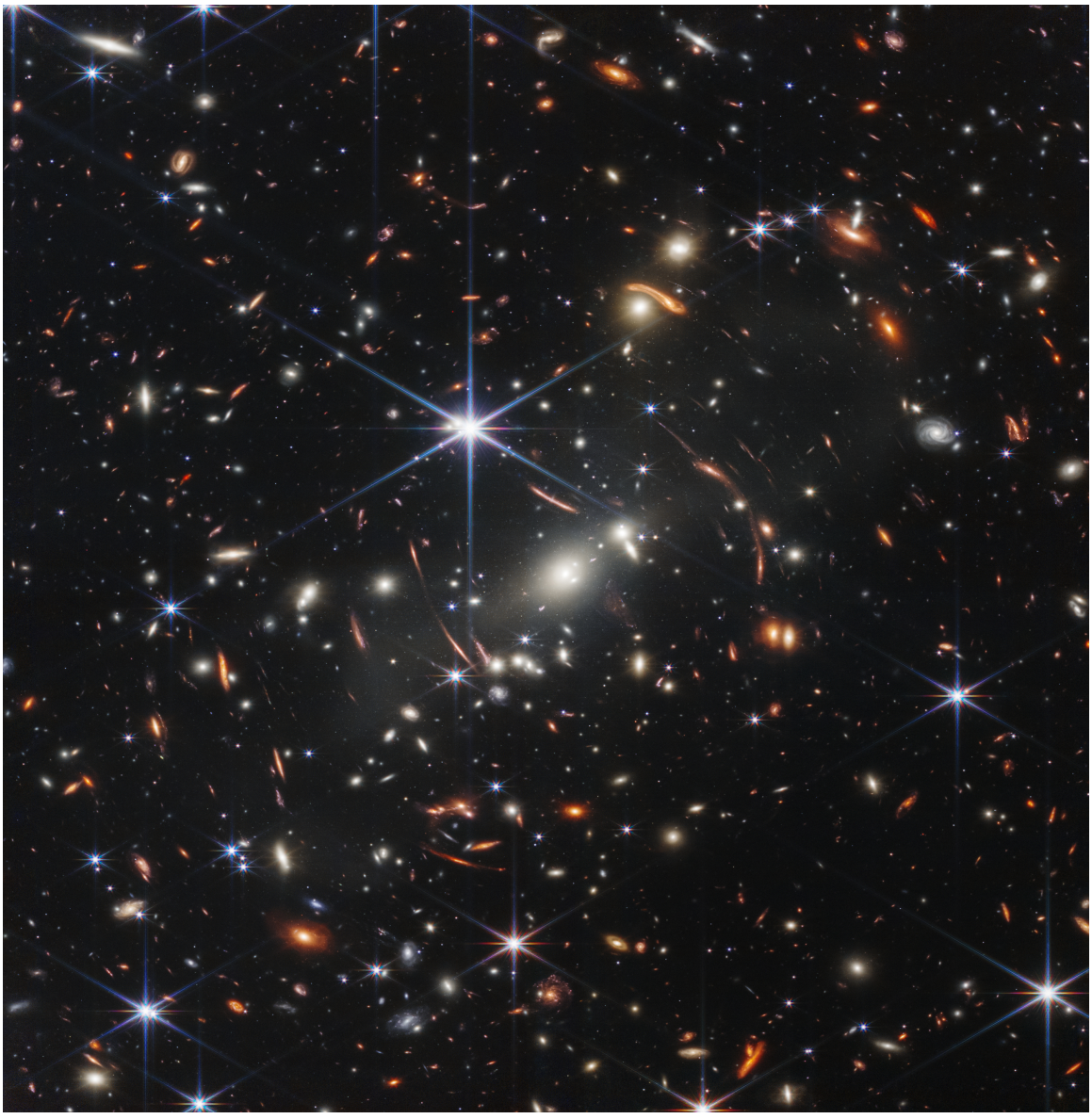

Figure 2.2: The first science image from the James Webb Space Telescope (JWST) was of a gravitational lens, specifically the galaxy cluster SMACS 0723. Gravitational lenses magnify the light from background galaxies and create multiple images.[10]

2.1.3 Cosmic microwave background

The cosmic microwave background (CMB) is a form of radiation that was leftover from the Big Bang. It has been used to study the large-scale structure of the universe, and its fluctuations provide strong evidence for the presence of dark matter. The CMB is a relic radiation that was emitted when the universe was only 380,000 years old, and it has been traveling through space ever since. Two of the most prominent experiments used to observe the cosmic microwave background (CMB) are the Wilkinson Microwave Anisotropy Probe (WMAP) and the Planck experiment.

WMAP was one of the first experiments to produce a detailed map of the CMB. Its data provided strong evidence for the existence of dark matter in the universe. The fluctuations in the CMB that WMAP observed were consistent with the presence of dark matter, which is believed to have played a key role in the formation of large-scale structures like galaxies and galaxy clusters. The WMAP mission provided important data on the CMB that has been used to estimate the total amount of matter in the universe, including dark matter [13]. The Planck experiment has also provided data on the CMB. Its latest data confirmed the presence of dark matter in the universe and provided more precise estimates of its properties [14].

WMAP and Planck measured the temperature differences of the cosmic microwave background at different angular scales, as shown in Fig. 2.3. This data enables us to determine the density of ordinary matter and dark matter in the universe. Baryonic matter density is denoted by Ω_b, while dark matter density is denoted by Ω_{dm}. In this graph, a higher baryon density corresponds to a higher power spectrum. The best-fit result of the data indicates that the density of dark matter is $\Omega_{dm} = 0.222 \pm 0.026$, and the baryon mass is $\Omega_b = 0.0449 \pm 0.0028$, as published in WMAP's seven-year publication [16]. These results suggest that dark matter accounts for about 85% of the universe's mass.

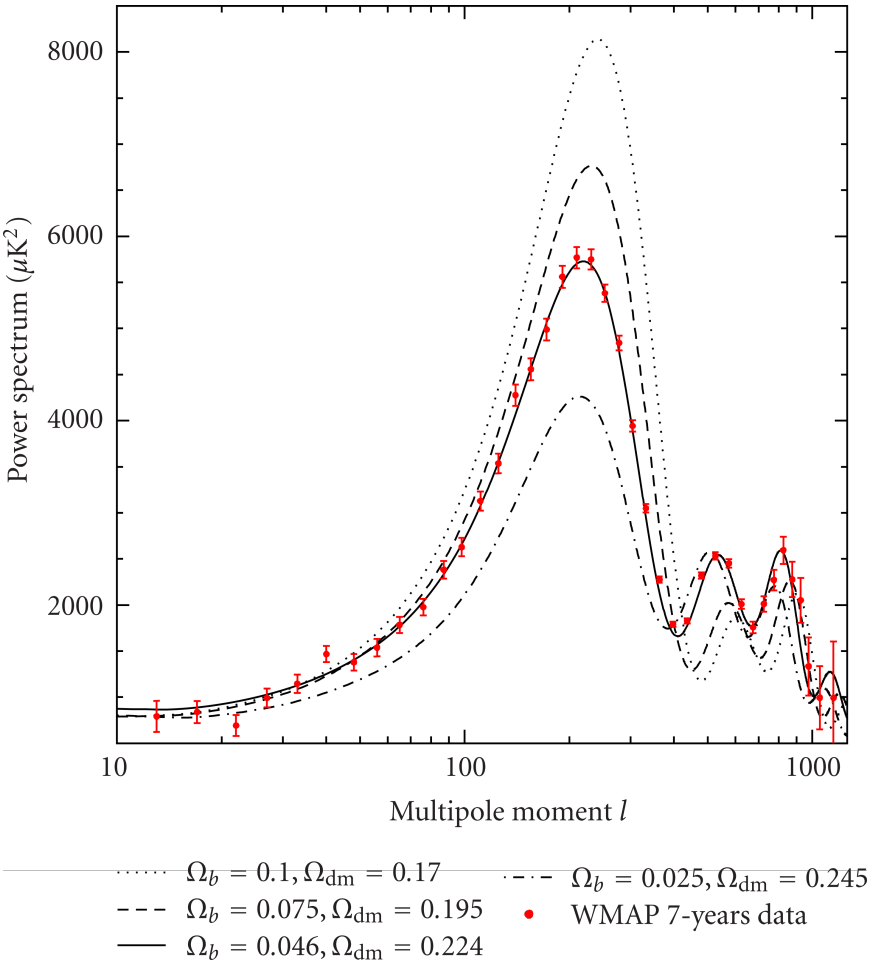

Figure 2.3: The power spectrum of in the WMAP experiment with different baryon density Ω_b and dark matter density Ω_{dm}. The anisotropy power spectrum gives the level of temperature fluctuations in different angular scales, where a spherical Fourier transform gives multipoles l, where $l \approx 180°/\theta$ [15]. The higher baryon density correspond to higher power spectrum.

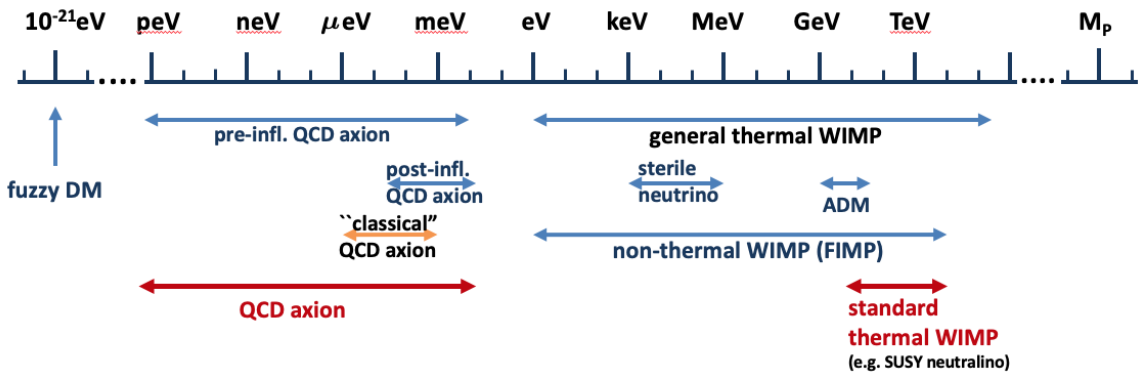

Figure 2.4: The graph presents different types of dark matter particle candidates across a wide range of mass scales. SUSY thermal WIMPs and QCD axions are shown in red, general thermal WIMPs and specific classes of axions are shown in blue, and the "classical" QCD axion mass regime is shown in orange. [17]

2.2 Dark matter candidates

Several models have been proposed to explain dark matter, including the particle dark matter model and the Modified Newtonian Dynamics (MOND). MOND is a modified gravity theory that attempts to explain the observed phenomena attributed to dark matter by changing the laws of gravity at low accelerations. This theory was originally aimed at clarifying the constant velocity observed in spiral galaxies' rotation curves from the Section. 2.1.1. However, MOND cannot explain other cosmological phenomenon such as gravitational lensing [8]. Therefore, only the particle dark matter model is currently the most widely accepted explanation for dark matter.

The particle dark matter model proposes that dark matter consists of one or more types of particles that interact weakly with ordinary matter, as Fig. 2.4 show. Two of the most popular candidates for dark matter particles are Weakly Interacting Massive Particles (WIMPs) and axions.

2.2.1 QCD axion

Axions are a hypothetical particles that could constitute dark matter. They were first proposed in the 1970s as a solution to the strong CP problem in particle physics [18]. The strong CP problem arises from the fact that the strong nuclear force, one

of the four fundamental forces of nature, should violate CP symmetry, but it doesn't. Axions were proposed as a solution because they could cancel out the CP-violating effects of the strong nuclear force. Axions were predicted to be very light, with masses ranging from 10^{-6} to 10^{-3} eV [19]. They are also predicted to be weakly interacting, like WIMPs, and would interact with ordinary matter only through the weak nuclear force.

Axions are one of the promising candidates for dark matter, and several experiments have been designed to search for them. These experiments include the Axion Dark Matter eXperiment (ADMX), which is designed to detect axions using a resonant cavity, and the CERN Axion Solar Telescope (CAST), which searches for axions produced in the sun [20]. Despite extensive searches, no conclusive evidence for axions as dark matter has been found yet.

2.2.2 Weakly Interacting Massive Particles

WIMPs are hypothetical particles that were first proposed in the 1980s by Goodman and Witten [21]. They are called weakly interacting because they interact with ordinary matter only through the weak nuclear force, one of the four fundamental forces of nature. The mass of WIMPs is typically predicted to be in the range of 10 to 1000 times the mass of a proton [22].

The most popular theoretical model for WIMPs is the supersymmetric model. Supersymmetry is a theoretical framework that extends the standard model of particle physics and predicts the existence of new particles, including WIMPs [22]. In the supersymmetric model, WIMPs are the lightest supersymmetric particles and are stable because they cannot decay into lighter particles. The supersymmetric model provides a natural explanation for the observed abundance of dark matter in the universe. The properties of WIMPs, such as their weak interaction with ordinary matter and their stable nature, make them excellent candidates for the elusive dark matter particles.

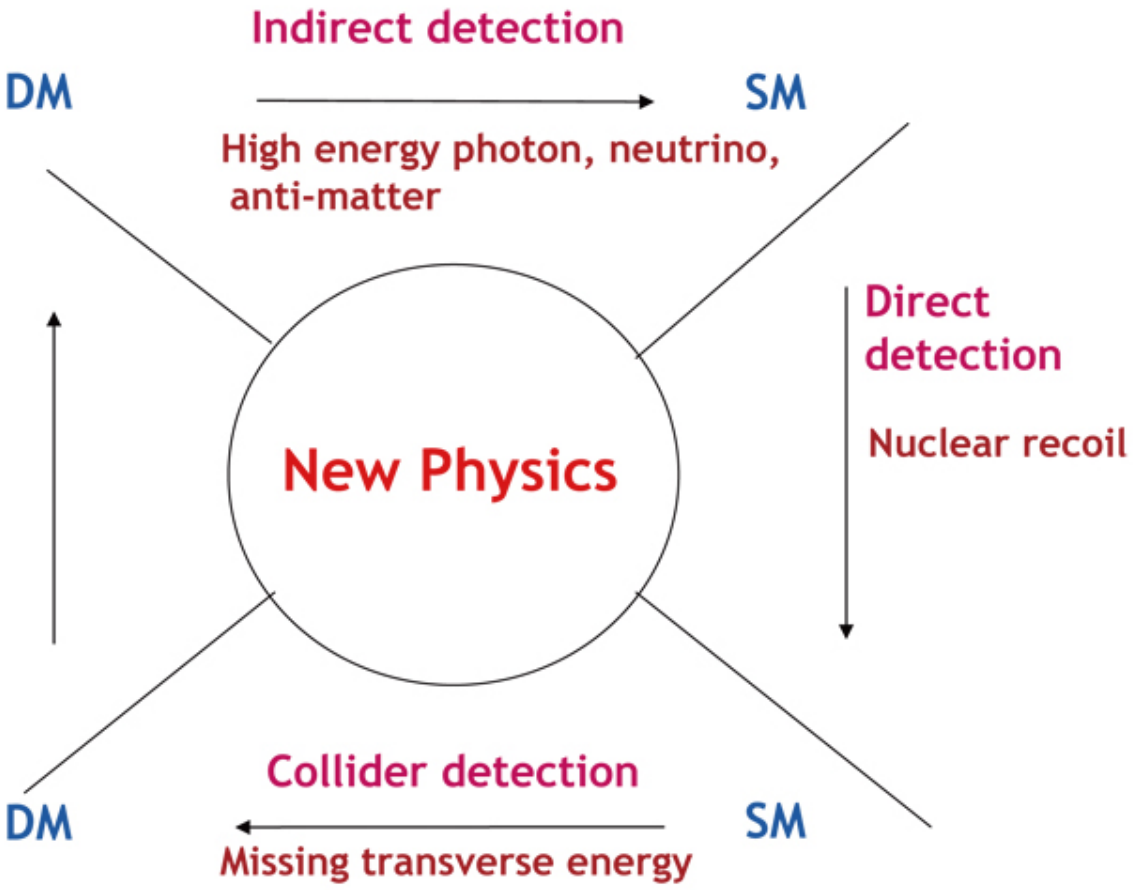

Figure 2.5: The diagram depicts the three main processes in which WIMPs could potentially interact with particles in the Standard Model (SM), namely indirect detection (annihilation), collider experiments (production), and direct detection (scattering).[24]

WIMPs are one of the most promising dark matter candidates, and direct detection experiments have been designed to search for them. These experiments look for the nuclear recoil of atoms that result from collisions with WIMPs [23].

2.3 Direct detection of WIMPs

The search for dark matter is a multifaceted effort that includes three types of experiments: collider, indirect, and direct detection, as illustrated in Fig. 2.5. Collider experiments, such as the Large Hadron Collider (LHC) at CERN, have also been employed in the search for dark matter particles. The goal of these experiments is

to produce dark matter particles by colliding high-energy protons with one another. If dark matter particles are produced, they would escape the detector without interacting with it, resulting in an energy or momentum imbalance in the collision event. One technique involves looking for missing transverse energy (MET) in the collision events, which would indicate the presence of an invisible particle, such as a dark matter particle, escaping the detector [25]. Another technique involves looking for the production of dark matter particles in association with standard model bosons, such as Higgs or Z bosons [26].

Indirect detection of WIMPs is another technique used to search for dark matter. This method involves looking for the products of WIMP annihilation, such as gamma rays, neutrinos, and cosmic rays. These products can be detected by telescopes and other detectors. However, indirect detection is challenging because it requires distinguishing the products of WIMP annihilation from other astrophysical sources.

Direct detection experiments aim to detect the scattering of WIMPs off nuclei in a detector. The signature of a WIMP-nucleus interaction would be a small recoil energy deposited in the detector. The recoil energy spectrum is expected to peak at low energies, typically below 100 keV, making the detection of WIMPs challenging, as many other background sources can produce similar signals.

2.3.1 Elastic scattering of the nuclei

Observations in cosmology have suggested the existence of a dark matter halo enveloping the Milky Way. This halo potentially interacts with detectors through elastic scattering, which makes the detection of WIMPs reliant on the event rate and the energy spectrum following an elastic collision on a target nucleus. The differential energy spectrum can be expressed as [27]:

$$\frac{dR}{dE_{nr}} = \frac{R_0}{E_0 r}\frac{k_0}{k_1}\left\{\frac{\sqrt{\pi}}{4}\frac{v_0}{v_E}\left[\mathrm{erf}\left(\frac{v_{\min}+v_E}{v_0}\right) - \mathrm{erf}\left(\frac{v_{\min}-v_E}{v_0}\right)\right] - e^{-v_{esc}^2/v_0^2}\right\} \quad (2.1)$$

where $r = 4\frac{m_N m_\chi}{(m_N+m_\chi)^2}$, m_N is the mass of the target nucleus and m_χ is the mass of the WIMP, $E_0 = 1/2 m_\chi v_0^2$ is the kinetic energy of the dark matter when $v = v_0 = 230$ km/s, E_{nr} is the nuclear recoil energy and v_E is the velocity of the earth relative to the galactic frame. k_1 corresponds to the truncated velocity distribution due to v_{esc}, where $v_{esc} = v_{max} = 533$ km/s is the escape velocity of the Milky Way. The ratio k_0/k_1 equals 0.9965, which implies that only 0.35% of the WIMPs have a velocity greater than the escape velocity. Moreover, v_{min} is the minimum velocity that causes nuclear recoil of energy E_{nr}, given by:

$$v_{min} = \sqrt{\frac{E_{nr} m_N}{2} \frac{1}{\mu^2}} \tag{2.2}$$

Here, μ is the reduced mass of the WIMP-nucleus scattering interaction, defined as:

$$\mu = \frac{m_N m_\chi}{m_N + m_\chi} \tag{2.3}$$

The event rate per unit mass when $v_E = 0$ and $v_{esc} = \infty$ is defined as R_0, which given by:

$$R_0 = \frac{2}{\sqrt{\pi}} \frac{N_A}{m_N} \frac{\rho_\chi}{m_\chi} \sigma v_0 \tag{2.4}$$

where N_A is Avogadro's number, ρ_χ is the local dark matter density, m_χ is the mass of WIMPs, and σ is the WIMP-nucleus scattering cross-section.

Then we can integrate the Eq. 2.1 over the energy to get the events rate.

$$R_{obs} = \int_{E_{\min}}^{E_{\max}} \varepsilon\left(E_{nr}, m_\chi\right) \frac{dR}{dE_{nr}} dE_{nr} \tag{2.5}$$

where R_{obs} is the observed event rate, ε is the detector efficiency, E_{min} and E_{max} are the lower and upper energy limits of region of interest.

$$\frac{d\sigma}{dE_{nr}} = \frac{\sigma_0 F^2(E_{nr})}{4\mu^2 v^2} \tag{2.6}$$

where $F^2(E_{nr})$ is the nuclear form factor. σ_0 is the zero-momentum cross-section for a WIMP of arbitrary spin and general Lorentz-invariant WIMP-nucleus cross-section may be written in terms of a $\sigma_{0,SI}$ spin-independent (mostly scalar) and a spin-dependent $\sigma_{0,SD}$ (mostly axial vector) term, given by:

$$\sigma_0 = \sigma_{0,SI} + \sigma_{0,SD} = \frac{4\mu^2}{\pi}\left[Zf_{\mathrm{p}} + (A-Z)f_{\mathrm{n}}\right]^2 + \frac{32G_{\mathrm{F}}^2\mu^2}{\pi}\frac{J+1}{J}\left(a_{\mathrm{p}}\left\langle S_{\mathrm{p}}\right\rangle + a_{\mathrm{n}}\left\langle S_{\mathrm{n}}\right\rangle\right)^2 \tag{2.7}$$

where A is the atomic mass, Z is the atomic number, f_p and f_n (a_p and a_n) are effective spin-independent (spin-dependent) couplings of the WIMP to the proton and neutron respectively, G_F is the Fermi constant, J is the total nuclear spin, $\langle S_p\rangle$ and $\langle S_n\rangle$ are the expectation values of proton and neutron spins. The values of spin and expectation values of proton and neutron spins for some selected elements are shown in Table. 2.1. For spin-independent (SI) cross-section, the couplings are considered to be the same $f_p \approx f_n$, therefore

$$\sigma_{0,\mathrm{SI}} \approx \frac{4\mu^2}{\pi} f_{\mathrm{n}}^2 A^2 \tag{2.8}$$

For the spin-dependent (SD) component, the complete expression is composed of two terms multiply with its "scaling factors" $4\left\langle S_p\right\rangle^2(J+1)/3J$ and $4\left\langle S_n\right\rangle^2(J+1)/3J$. They represent the cross-section for WIMP-proton and WIMP-neutron interactions respectively:

$$\sigma_{SD_p} = \frac{24G_F^2\mu_n^2 a_p^2}{\pi} \tag{2.9}$$

and

$$\sigma_{SD_n} = \frac{24G_F^2\mu_p^2 a_p^2}{\pi} \tag{2.10}$$

where μ_p and μ_n are the reduced mass of proton and neutron respectively.

When a search for Weakly Interacting Massive Particle (WIMP) candidate events yields no results [27], we set 90% confidence level (C.L.) limits on the WIMP-nucleon cross-section for a given WIMP mass. If a detector does not measure any events or if

Nucleus	Z	Odd Nuc.	J	$\langle S_p \rangle$	$\langle S_n \rangle$	$4\langle S_p \rangle^2 (J+1)$ $3J$	$4\langle S_n \rangle^2 (J+1)$ $3J$
^{19} F	9	p	1/2	0.477	-0.004	9.1×10^{-1}	6.4×10^{-5}
^{23}Na	11	p	3/2	0.248	0.020	1.3×10^{-1}	8.9×10^{-4}
^{27}Al	13	p	5/2	-0.343	0.030	2.2×10^{-1}	1.7×10^{-3}
^{29}Si	14	n	1/2	-0.002	0.130	1.6×10^{-5}	6.8×10^{-2}
^{35}Cl	17	p	3/2	-0.083	0.004	1.5×10^{-2}	3.6×10^{-5}
^{39} K	19	p	3/2	-0.180	0.050	7.2×10^{-2}	5.6×10^{-3}
^{73}Ge	32	n	9/2	0.030	0.378	1.5×10^{-3}	2.3×10^{-1}
^{93}Nb	41	p	9/2	0.460	0.080	3.4×10^{-1}	1.0×10^{-2}
^{125}Te	52	n	1/2	0.001	0.287	4.0×10^{-6}	3.3×10^{-1}
^{127}I	53	p	5/2	0.309	0.075	1.8×10^{-1}	1.0×10^{-2}
^{129}Xe	54	n	1/2	0.028	0.359	3.1×10^{-3}	5.2×10^{-1}
^{131}Xe	54	n	3/2	-0.009	-0.227	1.8×10^{-4}	1.2×10^{-1}

Table 2.1: The properties of selected odd proton and neutron nuclei, along with their relative sensitivities to spin-dependent interactions. The data displayed in the table includes the atomic number Z, the total nuclear spin J, and the expectation values of proton and neutron spins $\langle S_p \rangle$ and $\langle S_n \rangle$, the value is extracted from [27].

the background can be accurately predicted, the cross-section limit is determined by calculating the Poisson limit at a 90% confidence level. For instance, if no events are detected, the Poisson limit at 90% confidence level is equivalent to 2.3 counts. The method to determine this limit depends on the background of the experiment as well as the characteristics of the detector used. If the experiment has a flat background rate that does not mimic the detector response to dark matter interaction, the background rate can be subtracted to isolate the WIMP signal. In this case, the leftover signal is fitted with a WIMP signal, and the cross-section is extracted. The determination of the limit itself is performed with statistical tools that highly depend on the type of detector and background.

The parameter space for comparing various direct detection experiments for WIMP sensitivity is characterized by the mapping of specific cross-sections (SI or SD) to a range of sensitivities of the experiment to different masses of dark matter particles. Most experiments do not report any conclusive evidence of a WIMP signal. Instead, they define "exclusion" limits which correspond to regions in the parameter space that are statistically excluded based on the assumption that all observed unidentified signals come from WIMPs.

2.3.2 Detection technologies

Most experiments searching for dark matter detect signal of nuclear recoil from rare interactions between weakly interacting massive particles (WIMPs) and target nuclei. This principle is based on detecting energy transfer from WIMPs to our detectors. The energy can be detected as thermal energy via heat and phonons, as well as ionization charge and scintillation light from the nuclear recoil. The diagram in Fig. 2.6 illustrates the technologies used in these experiments. This chapter discusses some of the detection technologies used in direct detection experiments.

Scintillation detectors are based on the detection of scintillation light produced by dark matter particles interacting with target atoms in a detector. These pro-

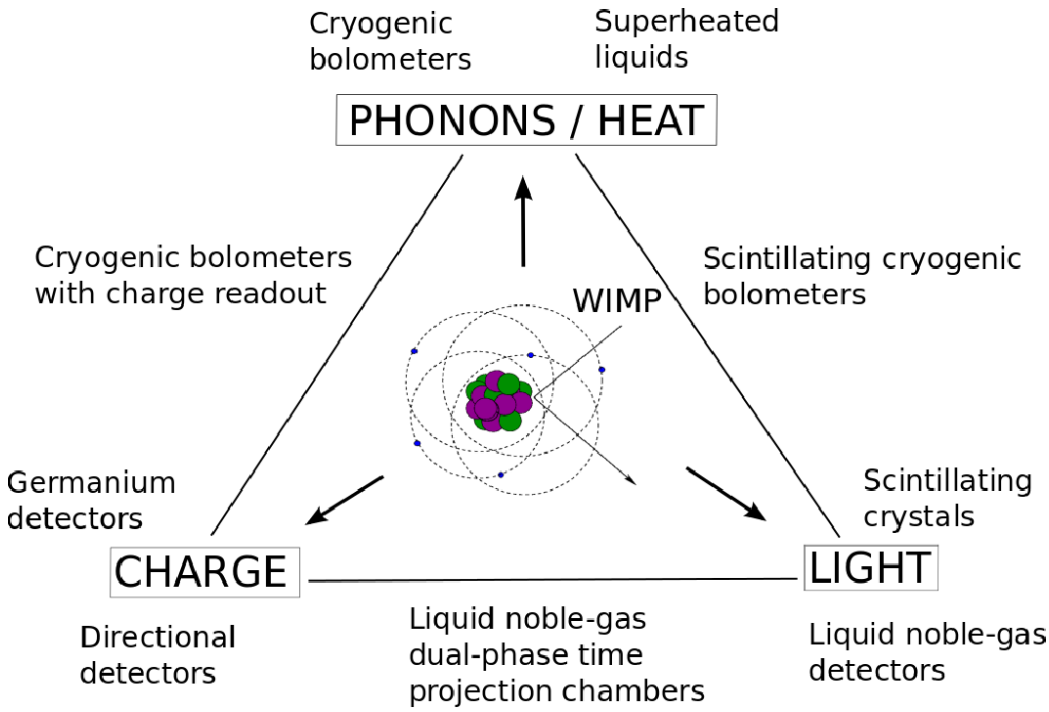

Figure 2.6: This diagram illustrates the possible signals that can be detected in direct detection experiments based on different technologies and detection media used. [28]

duced photons can be detected by sensitive photodetectors such as photomultiplier tubes (PMTs) or silicon photomultipliers (SiPMs). This technology is used in experiments such as the DAMA/LIBRA and DEAP experiments [29][30]. The DEAP is a single-phase argon scintillator detector, located in SNOLAB. It uses pulse-shape discrimination to identify background events [30]. The DAMA/LIBRA experiment, located in the Gran Sasso National Laboratory in Italy, is another direct detection experiment searching for dark matter. It uses a sodium iodide (NaI) scintillator detector to search for the signal of WIMPs. The experiment has reported positive results in the form of an annual modulation signal that could be interpreted as a WIMP signal [23]. However, other experiments have not been able to confirm these results, and the DAMA/LIBRA collaboration's interpretation of the data has been a topic of debate in the community [31].

Ionization detectors are based on the detection of ionization produced by recoil events. This ionization can be detected by semiconductor charge-coupled devices

(CCDs), which operate with high voltage to read out the signal with single-electron sensitivity. DAMIC and SENSEI are experiments using this technology [32][33]. Additionally, the NEWS-G experiment is a gas ionization Spherical Proportional Counter (SPC) that detects ionized electrons drifting through the high electric field inside the detector and can be detected as a current pulse [34]. The number of charges is proportional to the energy of the recoil events.

The heat produced by the WIMPs-nucleus interaction can also be a detection channel. One type of detector that uses heat is the bubble chamber detector, which is the theme of the present work. The details of the principle will be discussed in Chapter 3. The PICO experiment [35] is an example of a bubble chamber detector that uses fluorocarbon to detect WIMPs, particularly spin-independent WIMPs.

Another type of detector is the phonon detector, which senses the collective vibrations of atoms in a crystal lattice generated by dark matter particles as they elastically scatter with atomic nuclei. Phonon detectors convert these vibrations into measurable electrical signals. The Cryogenic Dark Matter Search (CDMS) and SuperCDMS experiments are examples of phonon detectors that use germanium and silicon crystals cooled to extremely low temperatures (millikelvin) to detect phonons generated by dark matter interactions [36]. Additionally, CDMS and SuperCDMS can detect ionization produced by these interactions. This use of multiple detection channels is known as hybrid detection technology.

Hybrid detection allows for greater sensitivity since different channels can probe different regions of parameter space, and it also helps with better background discrimination. Another notable experiment is XENON1T [37], which is a dual-phase liquid xenon experiment. XENON1T uses a hybrid detection technique that combines a time projection chamber (TPC) with a scintillation light detection system.

Last but not least, the scintillating bubble chamber (SBC) is a new experiment that combines the technology of both scintillation and bubble chamber detector [38]. SBC uses liquid argon doped with xenon as a target to operate in the superheated

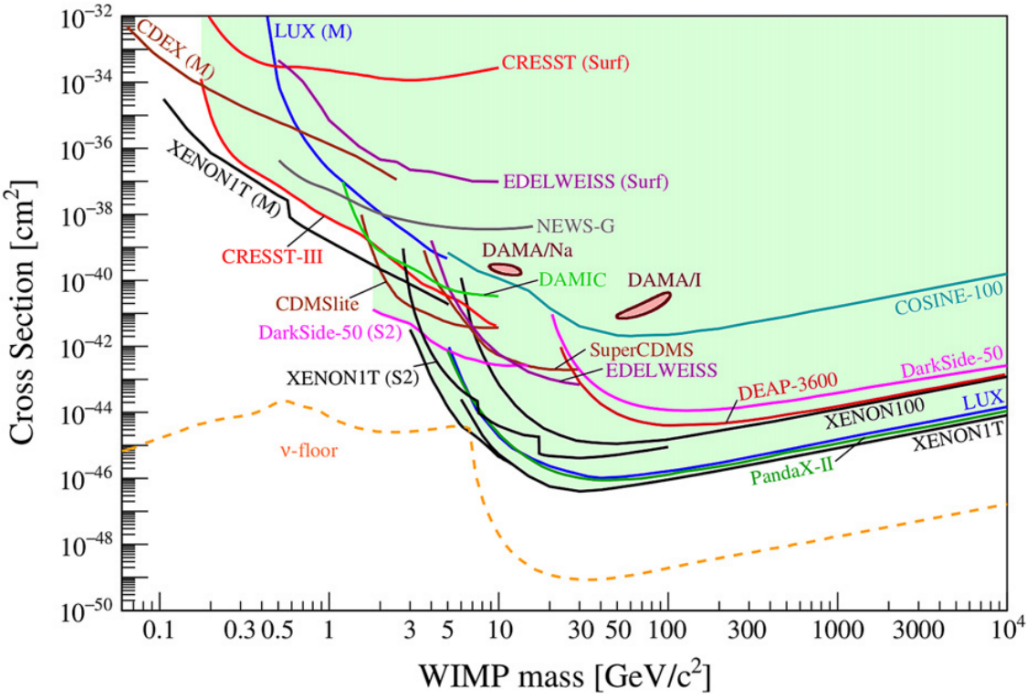

Figure 2.7: Status of direct detection experiment results for spin-independent (SI) WIMP-nucleon scattering cross-section as functions of WIMP mass in 2022 [17], with 90% confidence level. The dashed orange line represents the coherent elastic neutrino-nucleus scattering floors.

state. When the WIMPs cause nuclear recoil, the ionization will create photons, also the energy deposition will cause phase change from liquid to gas to form a bubble. The details will be discussed in the following chapters.

2.3.3 Status of the field

Direct detection experiments in the search for dark matter aim to identify the particle responsible for the majority of matter in the universe. These experiments rely on detecting rare interactions between dark matter particles and ordinary matter. Despite significant progress, the elusive nature of dark matter remains a mystery, with no positive detection to date. Typically, the results and projections of these experiments are presented as exclusion plots, illustrating limits on WIMP cross-sections versus WIMP masses, as discussed in section Fig. 2.3.1. The exclusion limits on both spin-dependent and spin-independent interactions are typically shown separately. Fig. 2.7

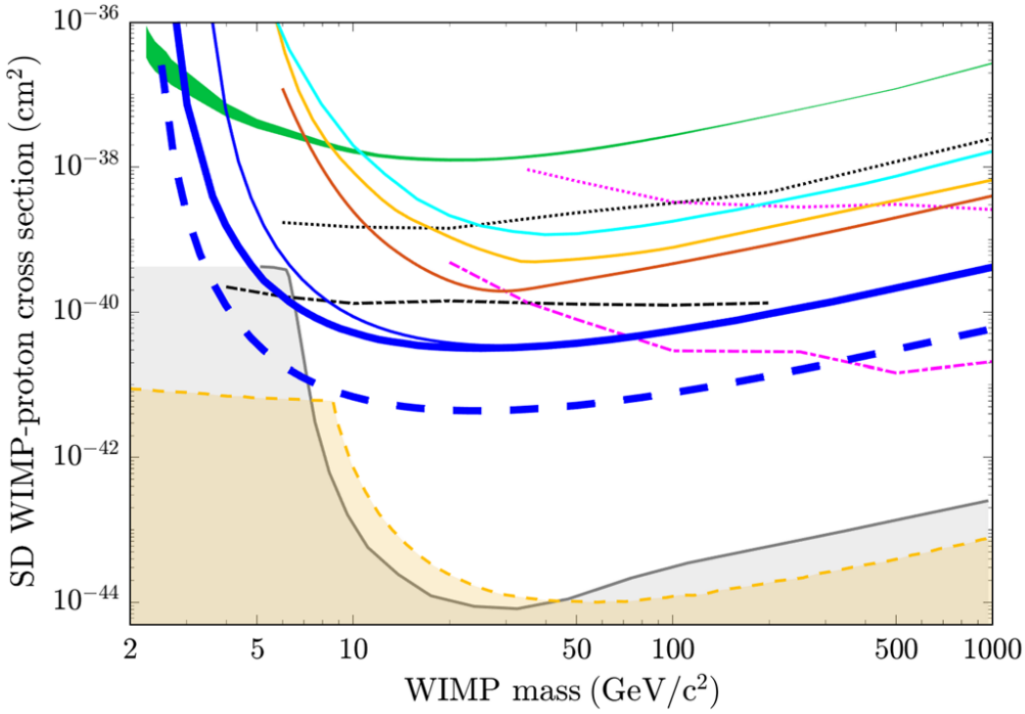

Figure 2.8: The graph shows the projected 90% C.L. spin-dependent WIMP-proton exclusion (dashed blue line) for two expected background events in PICO-40L at a 2.8 keV threshold with 1.64×10^2 kg-days of exposure, as compared against existing limits from several direct detection experiments [39]. The solid blue line corresponds to PICO-60, the orange line corresponds to XENON1T, the yellow line corresponds to LUX[40], the cyan line corresponds to PandaX-II[41], and the green line corresponds to PICASSO[42]. Indirect limits from IceCube (magenta)[43] and SuperK (black)[44] are also shown assuming annihilation to 7 leptons (dotted lines) and b quarks (dashed-dotted lines). The targets of coherent elastic neutrino-nucleus scattering floor are xenon (spin-dependent neutron, gray shaded) and C_3F_8 (no energy resolution, orange shaded).

shows the most recent (2022) results of spin-independent WIMP-nucleon cross-section exclusion limit. And for the spin-dependence WIMP-proton cross-section is shown in Fig. 2.8.

The major challenge in the direct detection of dark matter is the extremely low detection rate of dark matter particles. This makes it difficult to distinguish the signal from the background radiation. To address this, more sensitive detectors with lower background radiation and new detection techniques are required to increase sensitivity to dark matter particles at very low-masses (sub-GeV).

As shown in both exclusion limit plots Fig. 2.7 and Fig. 2.8, another major challenge in these experiments is the presence of a background signal from neutrinos. Neutrinos are produced by natural sources such as the Sun and cosmic-ray interactions in the Earth's atmosphere. They can produce similar energy deposits in the detector by coherent neutrino scattering, which makes it difficult to distinguish their signal from that expected from dark matter particles. This challenge is particularly significant for experiments that use low-mass target materials, as the neutrino background becomes increasingly dominant as the dark matter particle mass decreases. This is known as the "neutrino floor" Fig. 2.7 problem, and it ultimately limits the sensitivity of these experiments to dark matter particles with masses below a certain threshold. One possible way to address this challenge is to use directional channels which can help identify the source of the signal and effectively discriminate against neutrinos originating from known sources [45].

Chapter 3

Bubble chamber detectors

Bubble chamber detectors are one of the most important tools in experimental particle physics for studying the behavior of subatomic particles. It was first developed by Donald Glaser in 1952 [46], for which he was awarded the Nobel Prize in Physics in 1960. The bubble chamber was initially used to study cosmic rays, which are high-energy particles that originate outside of our atmosphere. Over time, it became clear that bubble chamber detectors could also be used to study particles that were produced in accelerators.

The basic principle of operation of a bubble chamber is that a liquid is maintained in a state called a superheated state, which will be introduced in the Section. 3.1. When a charged particle passes through the liquid, it ionizes the molecules along its path, creating a trail of ions. The resulting phase transition in the ionized region causes the liquid to boil along the particle track, forming a trail of bubbles [47]. The bubbles grow in size as they rise to the surface of the liquid, where they can be observed and photographed.

Bubble chamber detectors have led to many discoveries in particle physics, including the Z boson and J/ψ meson. The Gargamelle experiment at CERN used a large liquid hydrogen bubble chamber to study the weak interaction between neutrinos and electrons, confirming the existence of neutral current [48]. Eventually, this led to the discovery of the Z boson in UA1 and UA2 experiments later in 1983 [49]. Another

discovery made by the bubble chamber is the Ω^- particle at Brookhaven National Laboratory in 1964. [50]. The Ω^- particle is composed of 3 strange quarks, and its discovery helped confirm the quark model of Gell-Mann.

This chapter aims to provide an overview of the principle of operation of bubble chamber detectors and their application in dark matter searches. We will discuss the energy threshold, theory of bubble growth, two dark matter direct search experiments using bubble chambers (PICO and SBC), and nucleation efficiency as an important factor in determining the exclusion limit of the dark matter search experiment.

3.1 Principles of operation

The phenomenon of phase change is traditionally studied in classical thermodynamics under quasi-steady-state equilibrium conditions at saturation. However, a phase change occurs under non-equilibrium conditions. Vaporization processes, for instance, require temperatures that exceed the saturation temperature levels, known as superheating temperatures. Similarly, condensation can only occur after at least some vapor has been sub-cooled below the saturation temperature. As a result, saturation curve plots of pure substances exhibit regions where the liquid is superheated or the vapor is subcooled. These states are referred to as metastable [51].

Fig. 3.1 shows the $P - v$ (pressure verse molar volume) Clapeyron diagram for a pure substance, which highlights the regions where metastability occurs. It also contains an isotherm curve that represents different thermodynamic conditions. A state is considered thermodynamically stable when $(\partial P/\partial v)T < 0$, meaning that if the temperature level remains constant, an increase in pressure leads to a decrease in volume, or vice versa. Fig. 3.1 displays stable liquid and stable vapor in sections AB and FG, respectively. The horizontal line BF represents the liquid-vapor equilibrium state, while BC and EF indicate metastable superheated liquid and metastable subcooled vapor, respectively. The region CDE is an unstable region. The metastable regions are located between the saturation curve and the spinodal curve, where phase

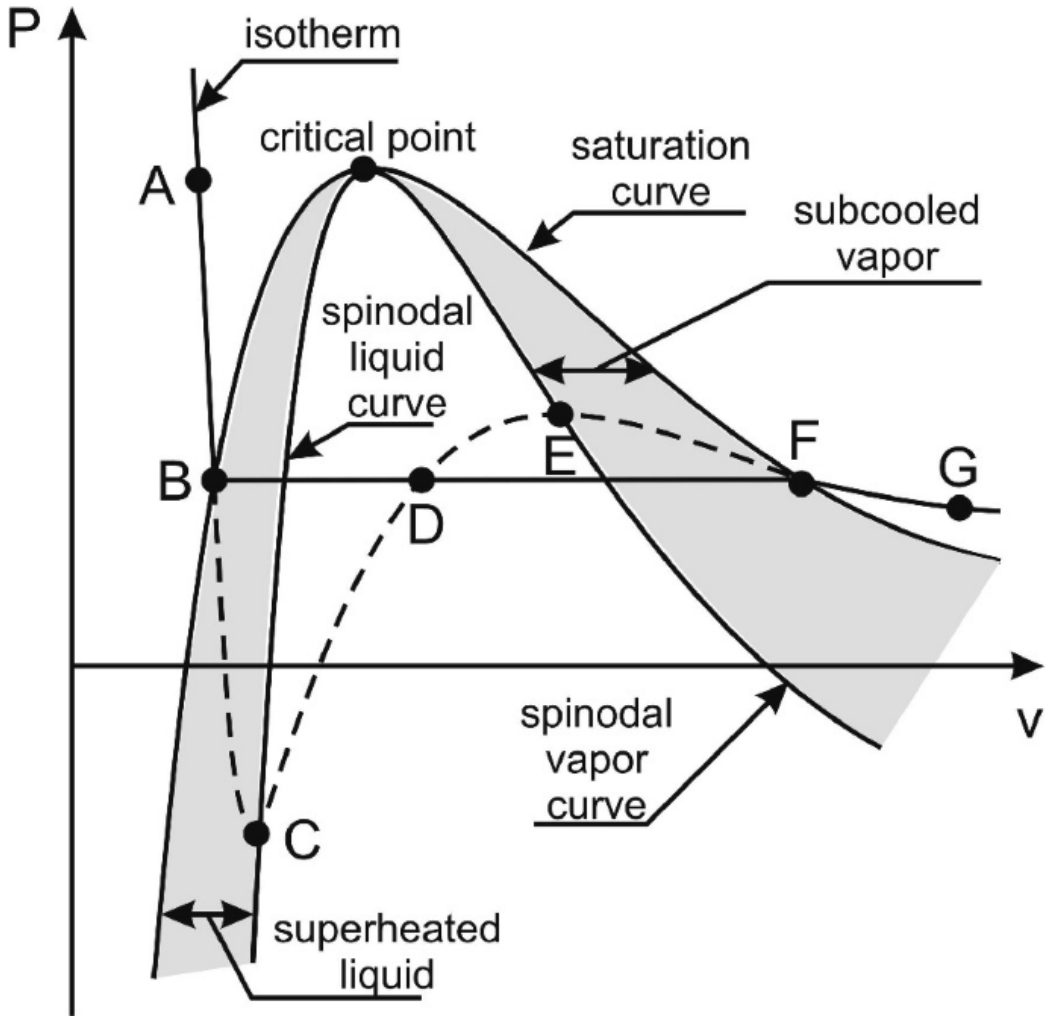

Figure 3.1: Pure substance $P - v$ diagram and Van der Waals curve. [51]

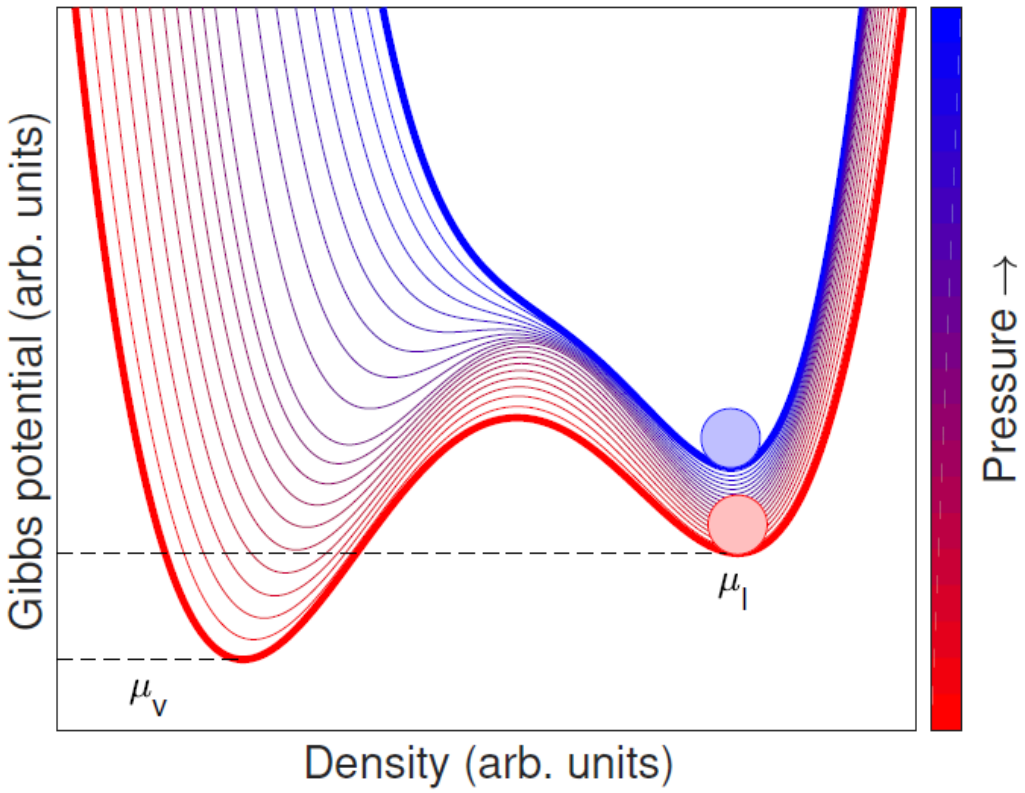

Figure 3.2: The diagram depicts the Gibbs free energy (Gibbs potential) as a function of density and pressure. As the pressure decreases (from blue to red), the Gibbs free energy of both the liquid and vapor phases decreases, but the energy in the lower-density vapor phase decreases at a faster rate than in the liquid phase. Consequently, the gas phase becomes more stable than the liquid phase.[52]

separation occurs for infinitesimal fluctuations in the composition and density of substances.

The Gibbs free energy, also known as the Gibbs potential, is a measure of the maximum amount of non-volume expansion work that can be done by a closed system at constant temperature and pressure. This measure is crucial for determining whether processes like chemical reactions can take place under given pressure and temperature. When a substance is held at constant pressure and temperature, its state is determined by calculating its minimum energy. In the case of a phase transition, energy can be absorbed or released due to a change from one phase to another. At equilibrium, both phases, such as liquid and gaseous phases of water at its boiling

point, coexist because they minimize the Gibbs potential. [52]

When a liquid substance is decreased isothermally and slowly in pressure from point AB to BC in Fig. 3.1, the Gibbs free energy of both the liquid and gaseous phases decreases until they reach equilibrium. If the pressure is further decreased, the Gibbs free energy of the gaseous phase becomes smaller than that of the liquid phase. Curves BC and EF follow the phase stability criteria, but are in a state of non-thermodynamic equilibrium, which means that, for the same pressure, there is another state of lower potential. This is demonstrated by plotting the Gibbs free energy as a function of density for various pressures, as shown in Fig. 3.2. The substance remains in a local minimum, which is a metastable state, in this case, the superheated liquid state. When a particle travels through the liquid, the energy deposit can overcome the potential barrier that causes a phase change resulting in a bubble. The energy is considered to be larger than a minimum threshold, called the Seitz threshold [53], which is discussed in the following sections.

3.1.1 Critical radius

When energy is deposited into a superheated liquid, it can cause a local phase transition resulting in the formation of a spherical cavity filled with vapor, known as a protobubble, which is surrounded by superheated liquid. A heat spike can cause the protobubble to reach a critical radius denoted as r_c, at which point it remains in static equilibrium with the surrounding liquid. If the protobubble's radius is less than r_c, it will collapse on itself. If, on the other hand, the radius exceeds r_c, it will undergo macroscopic expansion. The critical radius can be defined by the equation [47]:

$$r_c = \frac{2\sigma}{P_b - P_l} \tag{3.1}$$

Here, P_b is the vapor pressure inside the bubble, P_l is the liquid pressure, and σ is the surface tension. The pressure of the liquid P_l is a known value that can be controlled experimentally, whereas P_b cannot be directly measured and must be esti-

mated using other measurable quantities. P_b is defined by the equilibrium condition, which can be expressed by the Gibbs potentials for the liquid and vapor phases. At isothermal temperature T, when the pressure reaches the saturation point (points B and F in Fig. 3.1) where the vapor and liquid coexist, the vapor pressure is annotated as P_v (where $P_l < P_v$).

The change in Gibbs free energy when transitioning from P_l to P_v can be equivalent to change from P_b to P_v in the gas phase. The Gibbs free energy in differential form is given by:

$$dG = VdP - SdT + \mu dN \tag{3.2}$$

Here, V is volume, S is entropy, μ is chemical potential, and N is the number of particles. Since the phase change occurs under isothermal conditions and the number of particles does not change, we can simplify the equation to $dG = VdP$. Therefore, we can let the phase change between P_l and P_v be equal to P_b to P_v, and we have:

$$\Delta G = \int_{P_l}^{P_v} V_l dP = \int_{P_v}^{P_b} V_v dP \tag{3.3}$$

We consider the ideal gas law $PV_v = nRT$ and incompressible liquid (V_l does not change with P). After integrating both sides, we get:

$$V_l(P_v - P_l) = nRT \ln\left(\frac{P_v}{P_b}\right) \tag{3.4}$$

Substituting relations from the ideal gas law ($RT = P_v M/\rho_v$ and $V_l = nM/\rho_l$), we obtain:

$$\frac{P_v - P_l}{\rho_l} = \frac{P_v}{\rho_v} \ln\left(\frac{P_v}{P_b}\right) \tag{3.5}$$

Finally, we can express P_b as a known variable and approximate it using the first-order Taylor expansion:

$$P_b = P_v e^{-\frac{\rho_v}{\rho_l}(1-\frac{P_l}{P_v})} \approx P_v - \frac{\rho_v}{\rho_l}(P_l - P_v) \tag{3.6}$$

The critical radius can be expressed in terms of known variables:

$$r_c = \frac{2\sigma}{P_v - P_l}\frac{\rho_l}{\rho_l - \rho_v} \approx \frac{2\sigma}{P_v - P_l} \tag{3.7}$$

The approximation holds since the liquid density is much greater than the vapor density $\rho_l \gg \rho_v$. The critical radius is crucial to calculate the critical energy that must be deposited inside the radius to produce a phase transition in a superheated liquid.

3.1.2 Seitz threshold

The energy of the bubble contains the following major terms, Q_h the change in enthalpy or the latent heat, $Q_s + Q_{ds}$ the surface energy, Q_w the work done against the pressure p_l of the liquid. Therefore Seitz [53], following Pless and Plano's work [54], writes the necessary energy to form the initial bubble.

The energy of the bubble contains three major terms: Q_h, the phase change in enthalpy or the latent heat; Q_s, the surface energy; and Q_w, the work done against the pressure p_l of the liquid. Seitz [53] has written the necessary energy to form the initial bubble, following Pless and Plano's work [54]. The equation takes into account the three major terms and is given by:

$$Q_{\text{Seitz}} = \frac{4\pi}{3} r_c^3 \rho_b \Delta H + 4\pi r_c^2 \left(\sigma - T\frac{d\sigma}{dT}\right) - \frac{4}{3}\pi r_c^3 \left(P_b - P_l\right) + W_{irr} \tag{3.8}$$

where ΔH is the enthalpy of vaporization, σ is the surface tension, T is the temperature, P_b is the vapor pressure inside the bubble, P_l is the liquid pressure, and W_{irr} is the irreversible work term. ρ_b is the density of the vapor which can be calculated as

$$\rho_b \approx \rho_v \frac{P_b}{P_v} \tag{3.9}$$

In addition to the previously described terms, there is also an irreversible work term W_{irr} that accounts for the emission of acoustic waves, effects due to viscosity, energy lost to electronic excitation or ionization due to the recoil ion, and energy lost due to heat diffusion outside of the critical radius.

Traditionally, in nuclear recoil, bubble formation requires that the energy deposition along the track be greater than the critical energy in Eq. 3.8:

$$E_{dep} = \frac{dE_{dep}}{dx} l_c = \frac{dE_{dep}}{dx} b r_c > Q_{\text{Seitz}} \tag{3.10}$$

where l_c represents the track length, also known as the critical length, and b is a factor of critical radius that varies depending on the author [55][56]. In the PICO experiment [57], $b = 2$ is considered for a C_3F_8 target. This work considers track length as a variable that depends on both the primary recoil energy and the probability of interaction with target nuclei. The detail will be discussed in the following chapter.

As the critical radius decreases, the surface tension becomes dependent on the bubble radius due to the effect of intermolecular spacing, also known as the Tolman length [58]. At the protobubble stage, the curvature of the bubble surface is taken into account in the equations as a higher-order correction to both surface tension and radius. Consequently, the measured value of surface tension σ_0 is affected by these corrections, resulting in changes to both the surface tension and radius

$$\sigma/\sigma_0 = 1 + 2\frac{\delta}{r_0} \tag{3.11}$$

and

$$r/r_0 = 1 + 2\frac{\delta}{r_0} \tag{3.12}$$

where the σ_0 and r_0 represent the surface tension and critical radius when $\delta = 0$. We can then expand the Q_{Seitz} into δ/r_0 order, such that [59]:

$$Q = Q_0 + Q_1\frac{\delta}{r_0} + \mathcal{O}\left(\frac{\delta}{r_0}\right)^2 + ... \tag{3.13}$$

Using this definition, Q_0 and Q_1 can be written as:

$$\begin{aligned} Q_0 &= Q_{0,h} + Q_{0,s} + Q_{0,ds} + Q_{0,w} \\ Q_1 &= Q_{1,h} + Q_{1,s} + Q_{1,ds} + Q_{1,w} \end{aligned} \tag{3.14}$$

Each term can be decomposed as below,

$$\begin{aligned} Q_{0,h} &= \frac{4}{3}\pi r_0^3 \rho_b \left(h_b - h_l\right) \\ Q_{0,s} &= 4\pi r_0^2 \sigma_0 \\ Q_{0,ds} &= -\,4\pi r_0^2 t \frac{\partial \sigma}{\partial t}\bigg|\, \Delta p \\ Q_{0,w} &= -\frac{4}{3}\pi r_0^3 \left(P_b - P_l\right) \\ Q_{1,h} &= 8\pi r_0^3 \rho_b \left(h_b - h_l\right) \\ Q_{1,s} &= 24\pi r_0^2 \sigma_0 \\ Q_{1,ds} &= -\,16\pi r_0^2 t \frac{\partial \sigma_0}{\partial t}\bigg|\, \Delta p - \frac{4}{3}\pi r_0^3 \rho_b \left(h_b - h_l\right) \\ Q_{1,w} &= -8\pi r_0^3 \left(P_b - P_l\right) \end{aligned} \tag{3.15}$$

where Q_0 is the same as Q_{Seitz} in Eq. 3.8.

All these thermodynamic parameters of the targets are taken from REFPROP [60] from which the Seitz energy Q_{Seitz} (or the Q with correction) and the critical radius r_c can be calculated.

3.1.3 Bubble growth

If the energy deposition does not reach Seitz threshold energy along the track length, the initial bubble will collapse, otherwise, it will expand when these conditions in Eq. 3.10 are met. The growth of the bubble can be distinguished into two phases, each of which has been described in theoretical studies by Rayleigh [61] and Plesset and Zwick [62]. Both of these stages are based on approximate solutions derived from the Navier-Stokes equation and heat equations.

Once a bubble reaches the critical radius r_c size during the first stage, the energy transfer from the recoiling ion keeps it growing. The force that opposes bubble growth

is the surface tension of the surrounding liquid, which declines as the bubble grows. This process is described mathematically by the Rayleigh-Plesset equation

$$P_b = P_l + \frac{3}{2}\rho_l \dot{r}^2 + \rho_l r \dot{r} \tag{3.16}$$

where P_b is the pressure inside the bubble, P_l is the liquid pressure, ρ_l is the liquid density and r is the radius of the bubble. The equation provides a solution for the rate of bubble growth and is given by:

$$\begin{aligned} r_1(t) &= \phi_1 t, \\ \text{where, } \phi_1 &= \left(\frac{2}{3\rho_l}\left(P_b - P_l\right)\right)^{1/2} \end{aligned} \tag{3.17}$$

where ϕ_1 represents the rate of expansion and the subscript 1 represents the inertial regime. However, this equation can only describe bubble growth in a spherical shape. In reality, the geometry changes due to the linear energy transfer from the initial track to the spherical bubble, which requires an extra spatial degree of freedom. In this work, we study the evolution of bubbles from a cylindrical track using molecular dynamics simulations during the first few nanoseconds. Further details will be discussed in the next chapter.

The second stage is the thermal growth stage. As the initial energy diffuses, it becomes insufficient to support the phase transition. Heat transfer from the region surrounding the bubble is then required to provide the necessary energy. By combining the Rayleigh-Plesset equation [61] for the inertial growth phase and the Plesset-Zwick equation [54] for the thermal growth phase as in [16], we arrive at the bubble growth rate, such as:

$$\frac{\mathrm{d}R}{\mathrm{d}t} = -\left[\frac{A^2\sqrt{t-t_\mathrm{s}}}{B} + \frac{2\nu_l}{R}\right] + \sqrt{A^2 - \frac{2\sigma}{\rho_l R} + \left(\frac{2\nu_l}{R} + \frac{A^2\sqrt{t-t_\mathrm{s}}}{B}\right)^2} \tag{3.18}$$

where A is

$$A = \sqrt{\frac{2}{3}\frac{h\rho_\mathrm{v}\Delta T}{\rho_l T_\mathrm{sat}}} \tag{3.19}$$

where B is

$$B = \sqrt{\frac{12}{\pi a_l}}Ja = \sqrt{\frac{12a_l}{\pi}} \cdot \frac{2\Delta T^2 c_l}{3A^2 T_\mathrm{sat}} \tag{3.20}$$

where t_s is the time bubble become approximately spherical (eccentricity ¡ 0.3), ν_l is the liquid viscosity, σ is the surface tension, ρ_l and ρ_v is the density of the liquid and vapor, h is the latent heat of vaporization, ΔT is the liquid superheat above the saturation temperature, T_{sat} is the saturation temperature, Ja is called the Jacob number with c_l being the liquid heat capacity, a_l is the thermal diffusivity of the liquid. We can solve this differential equation numerically with initial conditions of radius R_s and time t_s when the bubble becomes spherical. We defined the bubble become sphere to be when the eccentricity smaller than 0.4. Bubble growth is particularly useful in the context of dark matter bubble chamber experiments, where the bubble's expansion serves as a source of acoustic emission. This equation will be used to model the acoustic intensity to discriminate α particle background events from nuclear recoil events.

3.1.4 Acoustic Signal

When bubbles grow in a metastable superheated liquid and exceed the critical radius, they undergo macroscopic expansion, emitting an acoustic wave. The power radiated by this wave can be described by the following equation [63]:

$$\mathcal{P} = \frac{\rho_l \ddot{V}^2}{4\pi c} = \frac{\rho_l}{4\pi c}\left(\frac{4\pi \ddot{r}^3}{3}\right)^2 = \frac{4\pi\rho_l}{9c}\left(3r^2\ddot{r} + 6\dot{r}^2 r\right)^4 \tag{3.21}$$

Here, $\ddot{V}$ is the acceleration of the volume expansion, and c is the speed of sound in the liquid phase. We can replace the solved numerical solution $r(t)$ from Eq. 3.18. The intensity (power per unit area) of the pressure acoustic is defined as:

$$I = \frac{\mathcal{P}(t)^2}{\rho_l c} = |\mathcal{A}(f)|^2 \tag{3.22}$$

The acoustic pressure intensity can be converted into a frequency spectrum by performing a discrete Fourier transform and taking the norm of the complex pressure amplitude $\mathcal{A}(f)$. Fig. 3.3 shows the pressure intensity in the frequency domain during the bubble growth in different events. In the PICO experiment, the frequency range

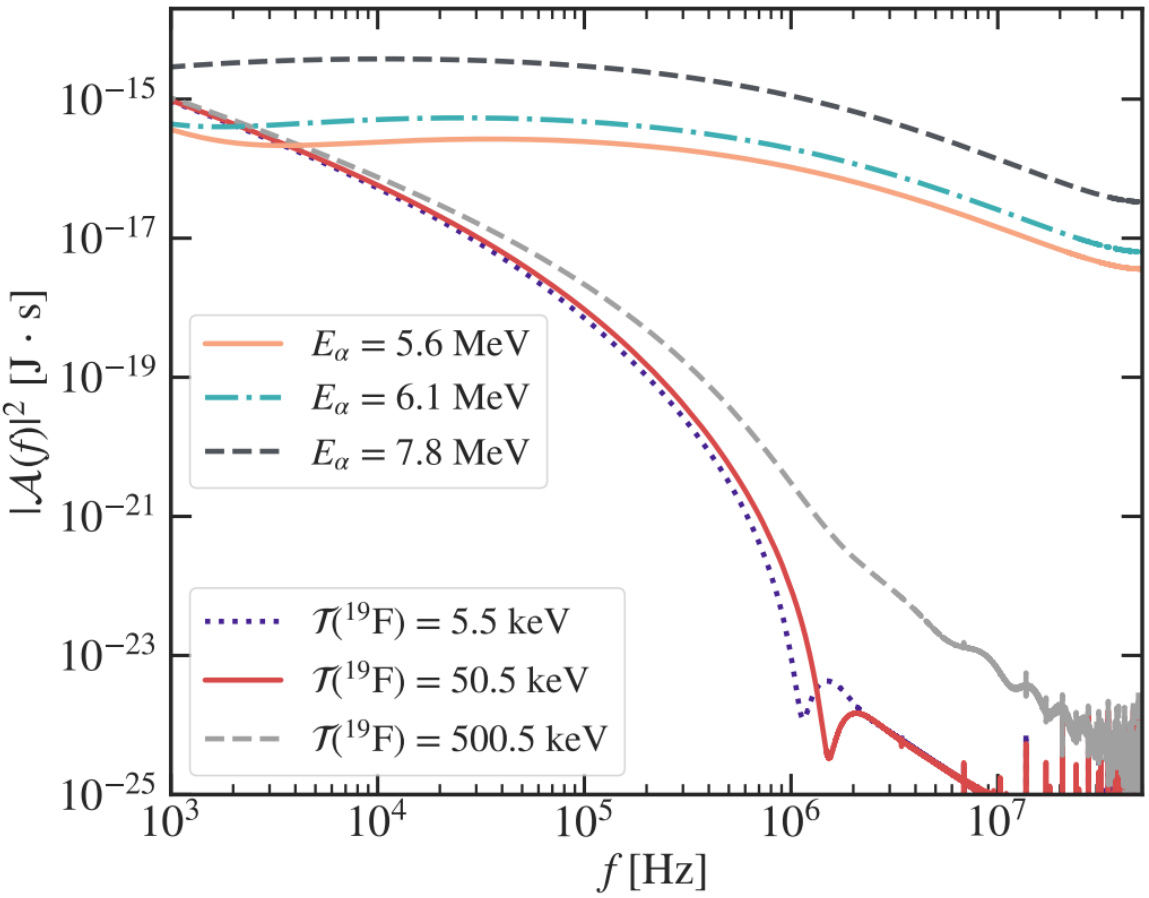

Figure 3.3: Acoustic power frequency spectra during the expansion of nuclear recoil and alpha-induced bubbles events [63]. The E_α curves represent the alpha induce bubble events, and the $\mathcal{T}(^{19}\mathrm{F})$ curves represent the fluorine recoil events.

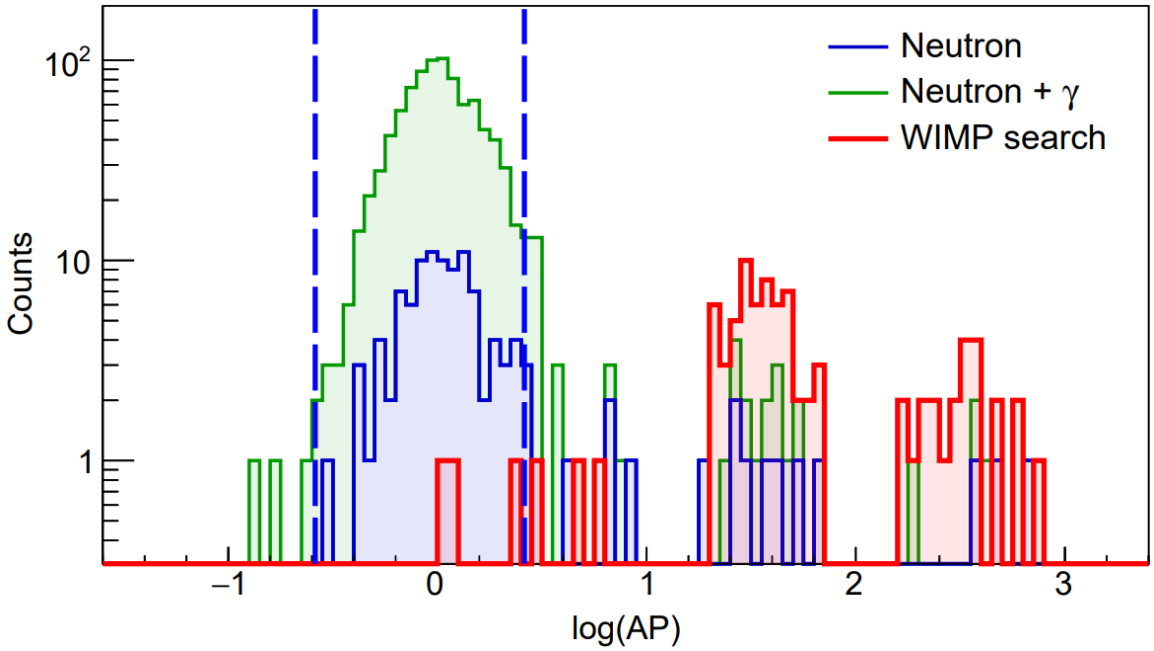

Figure 3.4: The WIMP-search AP data of the PICO-60 experiment at a 2.45 keV threshold (in red), along with the AP distributions for ^{252}Cf (blue) and ^{133}Ba calibration data (combined with ^{252}Cf, green). The acceptance region for nuclear recoil candidates defined through neutron and gamma calibration data.[35]

of interest is from 1 kHz to 300 kHz [63], in order to distinguish different particle events. The acoustic parameter (AP) is calculated by integrating the intensity in the frequency domain, as shown in the following equation:

$$AP = \int_{1kHz}^{300kHz} I(f)df \tag{3.23}$$

where $I(f)$ represents the intensity in the frequency domain. Fig. 3.4 shows the AP distributions in the PICO experiment WIMP-search results, as well as the neutron and gamma calibration data.

3.2 Experiments

In the field of direct search experiments for dark matter, two major experiments use bubble chamber technology: PICO and SBC. This work will focus on analyzing the data and targets of these two detectors. The following subsection introduces these two experiments.

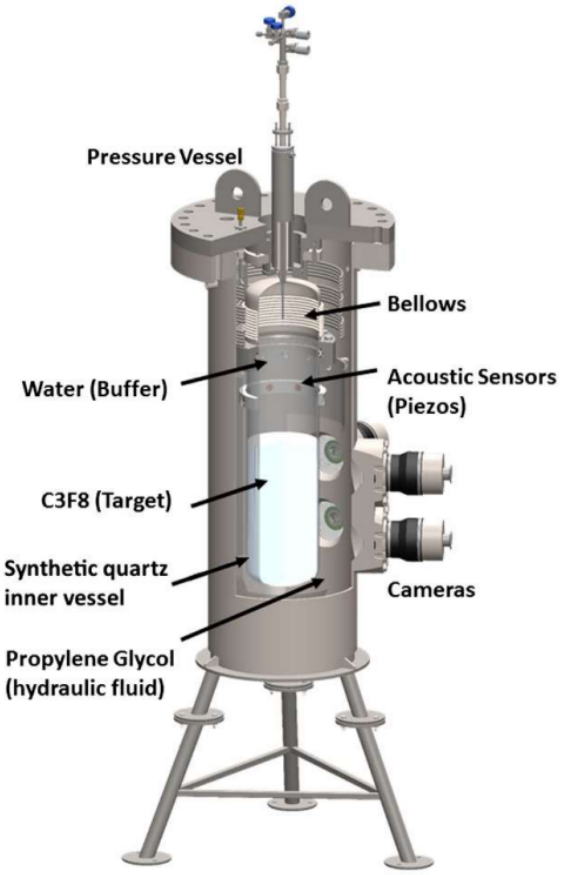

Figure 3.5: The PICO-60 detector model that operated with C_3F_8. [35]

3.2.1 PICO experiment

The PICO experiment is named after two former bubble chamber dark matter experiments, PICASSO (Project In CAnada to Search for Supersymmetric Objects) and COUPP (Chicagoland Observatory for Underground Particle Physics). Fig. 3.5 shows the model of PICO-60 as illustration.

The PICO experiment is a research project that aims to detect dark matter in the form of Weakly Interacting Massive Particles (WIMPs) using bubble chambers. These chambers are designed to operate similarly to historical bubble chambers but with a lower degree of superheat. This lower degree of superheat results in a higher energy threshold of approximately $\mathcal{O}$ (keV) [35], allowing PICO's bubble chambers to remain active for hours, waiting for a dark matter interaction. If the energy deposition

nucleates a bubble, it is recorded by cameras as an event. Additionally, piezoelectric acoustic sensors detect the acoustic power released during bubble formation, while pressure and temperature measurements determine the thermodynamic state of the chamber.

Since its operation, PICO has maintained its position as the world's leading exclusion limit for dark matter spin-dependent (SD) WIMP-proton interaction, and it has continued to enhance this limit. The initial PICO-60 detector used 36.8 kg of CF_3I as the active liquid during its first run[64]. For the subsequent PICO-2L detector, 2.90 kg of C_3F_8 was used. In the second run of PICO-60, the chamber was filled with 52 kg of C_3F_8 [35]. Currently, the PICO collaboration is constructing PICO40L [39], which will contain approximately 40L of active freon. Additionally, they are designing their next detector, PICO500, which will contain approximately 500L of active freon [65].

3.2.2 SBC experiment

The Scintillating Bubble Chamber (SBC) is a liquid-noble bubble chamber that detects low-mass (GeV-scale) dark matter and coherent scattering of low-energy (MeV-scale) neutrinos (CEνNS)[38]. It combines two technologies: the bubble chamber and the noble liquids gas scintillation detector. In the SBC experiment, superheated liquid argon is used as the target. In order to optimize the collection efficiency of scintillation light by silicon photomultipliers (SiPMs), a small concentration of xenon ($\mathcal{O}$(ppm)) is added as a wavelength shifter. This addition xenon facilitates the conversion of ultraviolet scintillation light to blue scintillation light, enabling SiPMs to capture the light higher quantum effectively. The SBC detector is shown in Fig. 3.6.

The liquid-noble bubble chamber technology is highly scalable and offers excellent background discrimination power, making it an attractive option for future dark matter searches. The projected spin-independent sensitivity of the upcoming dark matter search is approximately 10^{-43} cm^2 at 1 GeV/c^2 dark matter particle mass [38]. This technique is also well-suited for studying the solar neutrino floor at 1 GeV/c^2

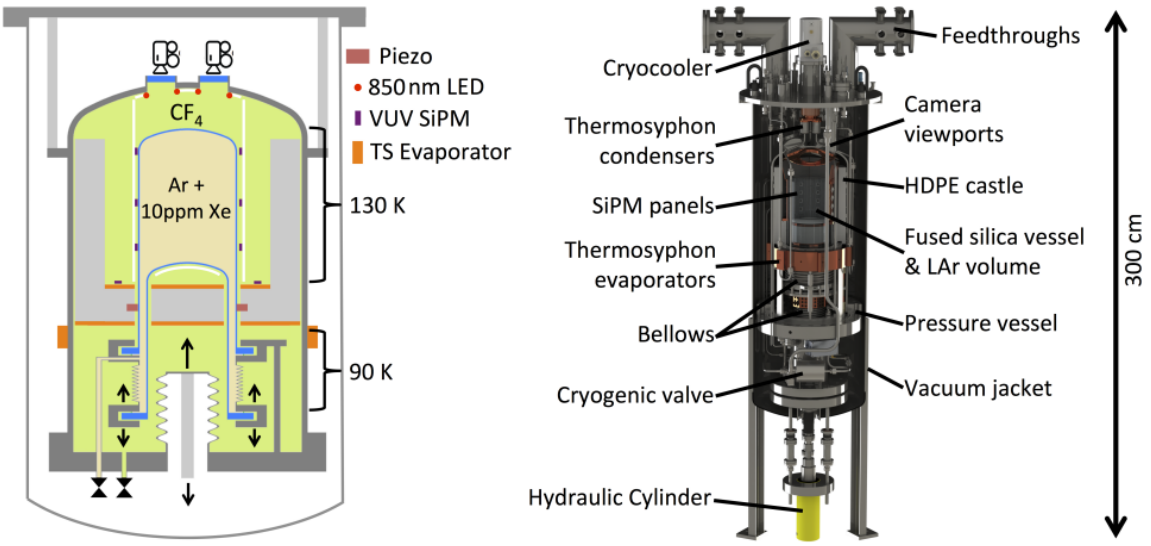

Figure 3.6: Schematic of the SBC (left) and annotated detail model (right) of the SBC-LAr10 detector. [38]

particle mass, which requires a ton-year exposure with non-neutrino backgrounds subdominant to the solar CEνNS signal. Additionally, the scalability and low background noise of the liquid-noble bubble chamber technology can benefit high-statistics CEνNS studies at nuclear reactors.

The SBC-LAr10, a 10-kg liquid argon bubble chamber [38], is the first physics-scale demonstrator of this technique and is currently being commissioned at Fermilab. This detector will calibrate the background discrimination power and sensitivity of superheated argon to nuclear recoils at energies as low as 100 eV. A second detector, identical in function to the SBC-LAr10 but with a focus on radiopure construction, is being built for SBC's first dark matter search at SNOLAB.

3.3 Nucleation efficiency

The Seitz threshold mentioned above does not guarantee bubble nucleation when the nuclear recoil energy exceeds the threshold energy. The model does not take into account energy losses to the electronic stopping, which causes electron excitation and ionization. Furthermore, the energy distribution is affected by the geometry of the

track length, as longer tracks cause heat diffusion outside of the critical radius.

The effects mentioned above can shift the nuclear recoil detection threshold and, in the case of straggling, broaden it. This can lead to detection efficiencies below 100% near the threshold. As Fig. 3.7 shows. The experimental analysis [66] [67] revealed that the bubble nucleation efficiency is a function depending on the recoil energy instead of a step function, as the current theoretical Seitz model indicates.

The goal of this work is to construct a physics model that explains the discrepancy between experimental results and the current theoretical model. In Chapter 4, we will introduce the details of our molecular dynamics simulations, which we conducted to study the first stage of bubble nucleation.

In Chapter 5, we will introduce our Monte Carlo simulations, where we connect the energy required for bubble formation with primary recoil energy loss. The probability of bubble nucleation for each nuclear recoil energy depends on the energy distribution in each event, which determines whether the bubble grows or collapses.

Finally, in Chapter 6, we compare the results of our model with those of recent studies using liquid xenon bubble chambers [66] and PICO C_3F_8 bubble chambers [67].

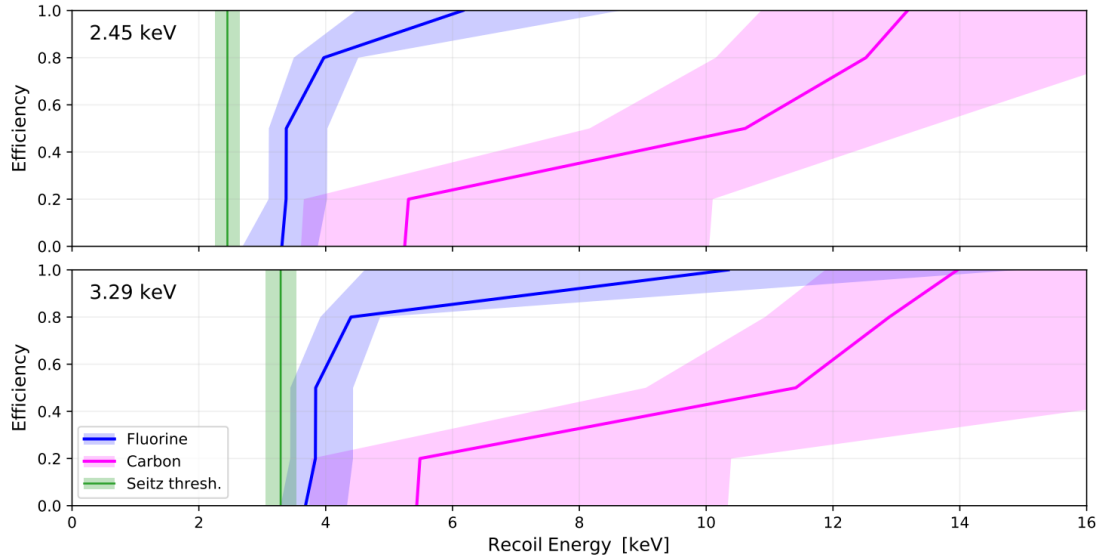

(a) The nucleation efficiency curves obtained from the PICO-60 C_3F_8 data. The best-fit curves and 1 σ error bands for fluorine and carbon are shown in blue and magenta, respectively, while the green bands indicate both thermodynamic Seitz thresholds (2.45 keV above and 3.29 keV below). [66].

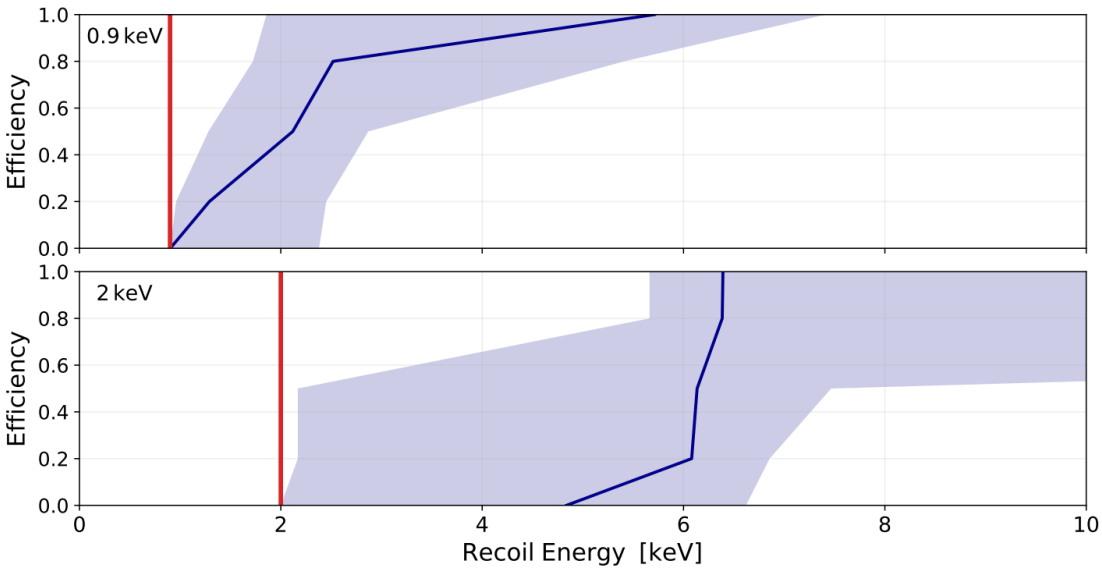

(b) The Preliminary results for nucleation efficiency in SBC LXe prototype [38], with a 1 σ error bands from the best fit (blue). The thermodynamic Seitz thresholds of 0.9 keV and 2 keV are indicated in red. [66]

Figure 3.7: Discrepancy between Seitz threshold and the nucleation efficiency of nuclear recoil.

Chapter 4

Molecular dynamics simulation

The Seitz model describes the minimum energy required to form an initial bubble and the conditions for the bubble to continuously grow. However, the mechanism for forming the initial protobubble remains unclear.

To address this, Molecular Dynamics (MD) simulations were used to study the energy deposition from the nuclear recoil and the initial bubble growth. The MD simulation was performed using the Large-scale Atomic/Molecular Massively Parallel Simulator (LAMMPS) program [68]. In LAMMPS, we use the Lennard-Jones (LJ) potential to describe the interaction between atoms, specifically the attractive and repulsive forces between them:

$$V_{LJ} = 4\epsilon \left[\left(\frac{\sigma}{r} \right)^{12} - \left(\frac{\sigma}{r} \right)^{6} \right] \tag{4.1}$$

Here, r represents the distance between atoms, while σ refers to the distance at which the potential between atoms is zero, sometimes referred to as intermolecular distance. The potential energy has a minimum value of $-\epsilon$, where ϵ is the depth of the potential well. The r^{-6} term representing the dipole-dipole van der Waals attraction and the r^{-12} part is responsible for Pauli repulsion.

In practice, the truncated shifted-force Lennard-Jones (TSF-LJ) potential can accurately describe the superheated system [56] and is given by:

$$V_{\mathrm{TSF}}(r) = \begin{cases} V_{LJ}(r) - V_{LJ}\left(r_{\mathrm{cut}}\right) - \left(r - r_{\mathrm{cut}}\right) V'_{LJ}\left(r_{\mathrm{cut}}\right) & \text{for } r \leq r_{\mathrm{cut}} \\ 0 \quad \text{for } r > r_{\mathrm{cut}} \end{cases} \tag{4.2}$$

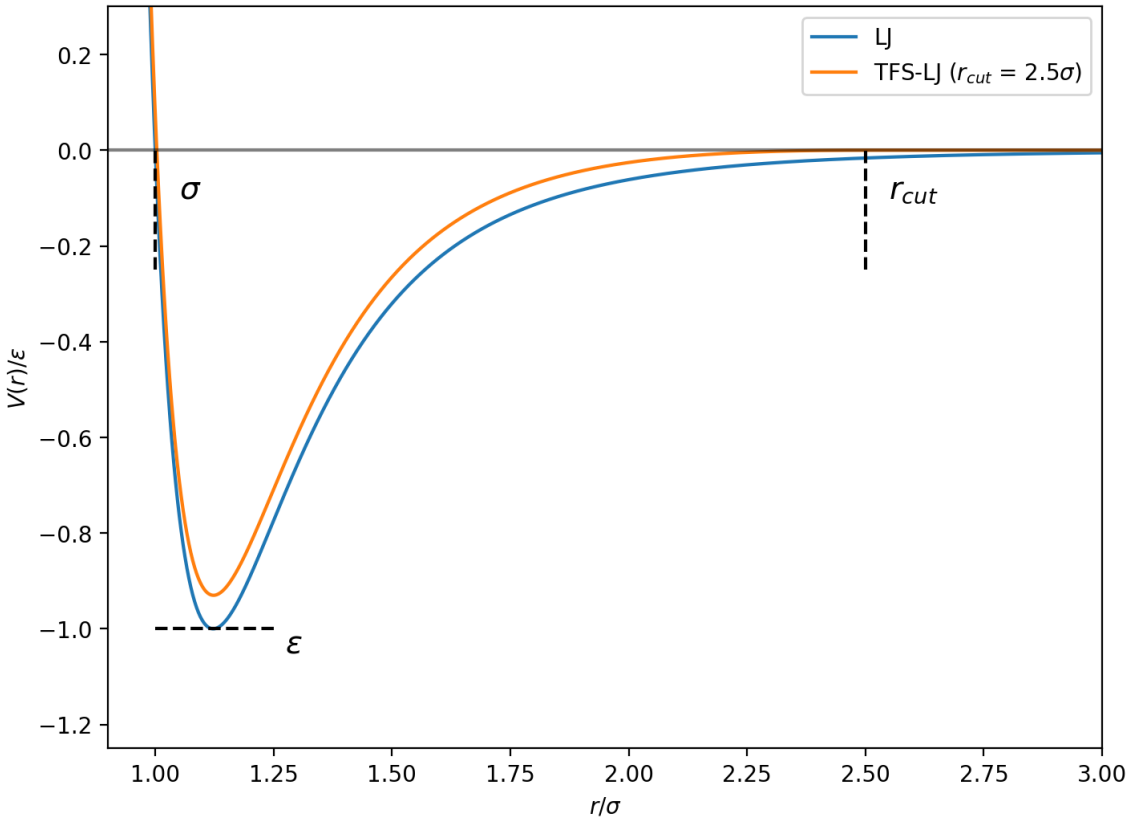

Figure 4.1: Comparison of Lennard-Jones (TSF-LJ) potential and shifted-force Lennard-Jones (TSF-LJ) potential.

where V'_{LJ} is the first derivative with respect to r and r_{cut} is the cutoff distance to maintain the computation efficient. $r_{\text{cut}} = 2.5\sigma$ for this work to ensures the deviation from the full-tail Eq. 4.1 to be smaller than 1.6% [63]. The shape of the potential function in Eq. 4.1 and Eq. 4.2 are shown in Fig. 4.1.

In MD simulations, all quantities are unitless and are referred to as LJ units. Without loss of generality, we assume that the fundamental quantities of mass, σ, ϵ, and the Boltzmann constant k_B are defined to be 1. The masses, distances, and energies specified in the system are multiples of these fundamental values. The transformation between the SI unit and the LJ unit is shown in Table. 4.1

Quantities	SI Unit	LJ Unit
Distance	$x = \sigma$	$x^* = x/\sigma$
Mass	$M = m$	$M^* = M/m$
Time	$\tau = \tau$	$\tau^* = \tau\sqrt{\frac{\epsilon}{m\sigma^2}}$
Energy	$E = \epsilon$	$E^* = E/\epsilon$
Density	$\rho = m/V$	$\rho^* = \rho\frac{\sigma^3}{m}$
Pressure	$P = P$	$P^* = P\frac{\sigma^3}{\epsilon}$

Table 4.1: Physical quantities express in SI and LJ Units

4.1 LAMMPS

LAMMPS simulates the motion and interactions of atoms in a system using the LJ potential under defined periodic conditions. The primary goal is to connect the LJ molecule (atom) to the target molecule (atom) by constraining σ and ϵ to SI unit quantities. The LJ energy unit ϵ can be calculated as $\epsilon = T_c k_B/0.935$, where T_c is the critical temperature. The value of $T_c k_B/\epsilon = 0.935$ is theoretically derived using an ordering map representation [69].

To constrain the intermolecular distance σ, we can simulate the saturation state at the same operational temperature as the detector. The saturation state includes both the liquid and gas phases, so we can use the densities of both phases to calculate σ. The simulation begins by creating a lattice of atoms and running NVE (constant number of particles, volume, and energy) at the detector's operating temperature in the saturated state. This process initializes a stable liquid system.

In NVE simulations, the number of particles (N), volume (V), and total energy (E) of the system are conserved, which is known as the microcanonical ensemble. NVE simulations do not use an external thermostat, and the system's energy is conserved throughout the simulation. This means that any energy exchanges or changes in temperature within the system occur solely due to the internal interactions between particles. NVE simulations are often used to examine energy conservation, study

dynamics without temperature fluctuations, or investigate systems in the absence of thermal baths or external temperature control.

Following the NVE simulation, we conducted an NVT (constant number of particles, volume, and temperature) simulation using the initialized system. This resulted in an isothermal saturation state that exists in both the liquid and gas phases.

In NVT simulations, the number of particles (N), volume (V), and temperature (T) of the system are held constant. A thermostat is used to adjust the velocities of the particles and maintain a desired temperature throughout the simulation. The NVT ensemble is particularly useful for studying systems where temperature is a crucial factor, such as thermal equilibrium or investigating temperature-dependent properties.

Next, we collect the density profile for the liquid and vapor in the simulation box and select the density of the system over the z-axis as ρ_z. We can then use a time-averaged hyperbolic tangent function that depends on z [70]:

$$\rho(z) = \frac{1}{2}\left(\rho_l + \rho_v\right) - \frac{1}{2}\left(\rho_l - \rho_v\right)\tanh\left[\frac{2\left(|z| - z_0\right)}{d}\right] \tag{4.3}$$

where ρ_l is the density of the liquid, ρ_v is the density of the vapor, and $z = z_0$ is the plane of the surface when $\rho(z_0) = \frac{1}{2}\left(\rho_l + \rho_v\right)$, which is the density equal to the average of the liquid and vapor. The measure the interface thickness d is defined as:

$$d = -(\rho_l - \rho_g)\left[\frac{d\rho(z)}{dz}\right]^{-1}_{z=z_0} \tag{4.4}$$

Fig. 4.2 shows an example of density along the central z-axis of CF_3I liquid. Once we have determined the density of the liquid in the saturation state, we make constrain the value of σ for a specific liquid using the LJ unit transform in Table 4.1: $\rho^* = \rho\frac{\sigma^3}{m}$.

Once the energy unit ϵ and spatial unit σ have been established for the LJ system, the next step is to create a superheated state using the NVE mode. For the lattice command, we can use the density of the superheated liquid. However, the density of the liquid in a superheated state is usually lower than the saturation state at

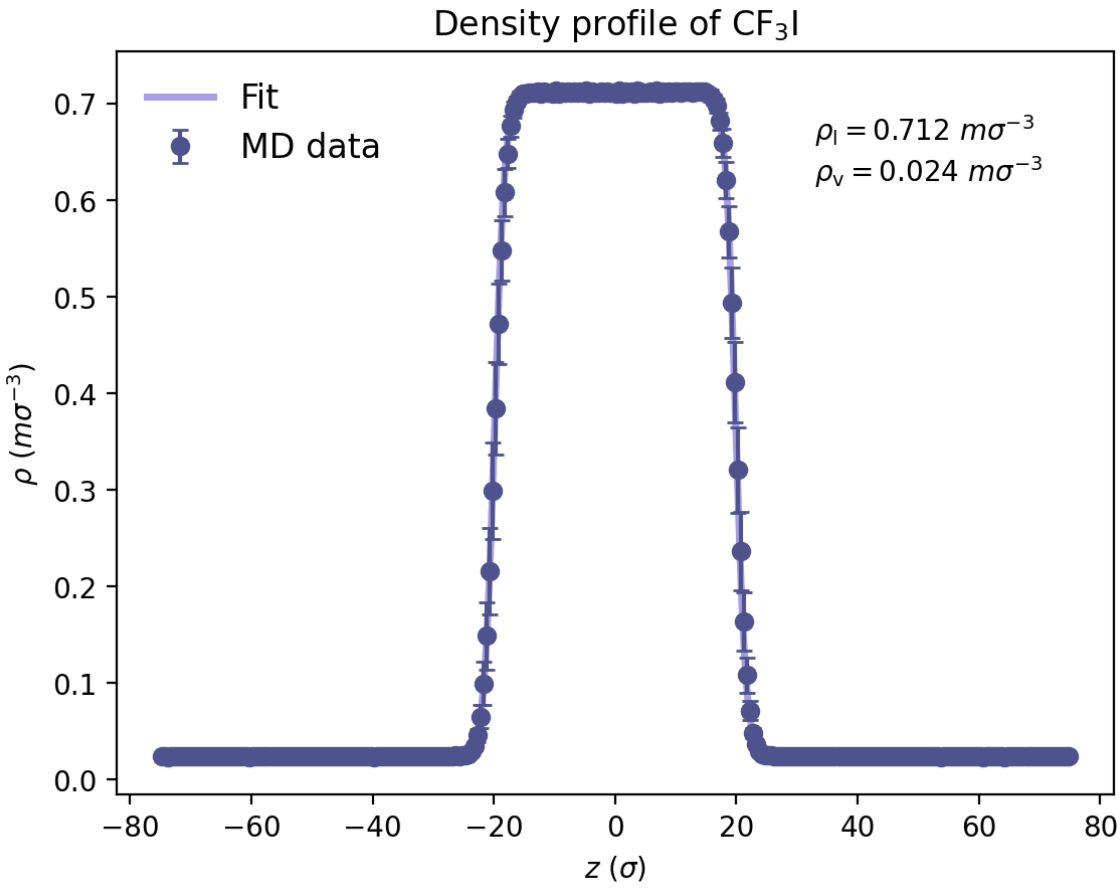

Figure 4.2: Saturation-state density distribution of CF_3I along the central line. Data points obtained from MC simulation, with fitting function defined in Eq. 4.3. Where ρ_l is the density of the liquid, ρ_v density of the vapor.

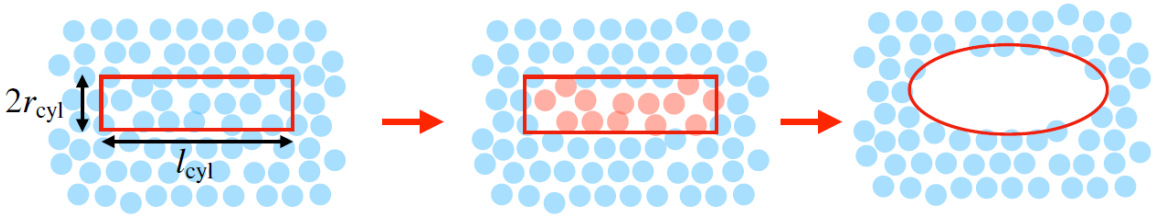

Figure 4.3: Schematic of energy deposition in the MD simulation. We selected a cylinder-shaped region and rescaled the temperature associated with the energy deposition using Eq. 4.6.

the same temperature. To start, we set the initial temperature to be slightly higher than the superheated temperature and then lower the temperature under the NVE ensemble. During the procedure, the system volume and the liquid density were kept constant. Consequently, the resulting density was insufficient for the stable liquid under the given temperature conditions. The density should have been increased proportionally to account for the decrease in temperature and maintain the system in a stable liquid state. As a result, the liquid remained in a superheated state. After creating the superheated system, we proceeded to simulate the energy deposition caused by the track of an ionizing particle from nuclear recoil. To model the track, we defined it as a narrow cylinder with length l_{cyl}, which is shown in the schematic in Fig. 4.3. The volume of the cylinder is given by:

$$V_{cyl} = \pi r_{cyl}^2 l_{cyl} \tag{4.5}$$

According to [63], the cylinder's radius is fixed at $r_{cyl} = 2\sigma$. We also varied r_{cyl} between 2 and 5 σ in the simulation, whereas it did not affect bubble formation. Therefore, we used $r_{cyl} = 2\sigma$ for all other simulations. Since we know the liquid's density ρ^* $[m\sigma^{-3}]$, the number of particles inside the cylinder will be a multiple of the volume with number density. Then, we rescale the temperature of the atom inside the region associated with the energy deposition using the following equation:

$$T_{dep} = \frac{2}{D}\frac{E_{dep}}{Nk_B} + T_0 \tag{4.6}$$

where D represents the degree of freedom of the target molecule or atom, T_0 represents the temperature of the superheated liquid (which is also the temperature of the detector), and N represents the number of atoms or molecules inside the cylindrical region. N can be calculated N with the superheated liquid density $N = \pi r_{cyl}^2 l_{cyl} \rho_l^*$. The degree of freedom of a molecule depends on its structure. Noble elements with monatomic structures, such as argon and xenon, have 3 translational degrees of freedom. In contrast, complex molecules like C_3F_8 and CF_3I have both 3 translational and 3 rotational degrees of freedom.

Since the simulation box is a finite region, we need to avoid the bubble expansion influence on the overall pressure of the system. To solve this, we use NPT ensemble mode to simulate the bubble growth.

The NPT ensemble enables control over the number of particles (N), pressure (P), and temperature (T) of a system. In this ensemble, the system can exchange particles with a reservoir while also exchanging energy and volume with external pressure and temperature baths. This approach is useful for investigating the behavior of liquids under constant pressure conditions. By maintaining a constant temperature and pressure, the NPT ensemble provides a realistic representation of the thermodynamic properties and dynamics of the system to study phase transition phenomena.

4.2 Results

Using MD, we can observe the bubble growth or collapse depending on the track length and energy deposition. Fig. 4.4 shows two events of the bubble nucleation process in molecular dynamic simulation for xenon. The upper graphs show the 2 keV energy deposition and the lower graphs show the 1 keV energy deposition. The sphere surface tracking is done by python `skimage.measure.find_contours` package. The effective radius R_{eff} represents the radius of a sphere that has the same volume as the non-spherical bubble. The red circle represents the bubble that becomes spherical (eccentricity < 0.4) and the red line is the fit obtained by the differential equations

in Eq. 3.18 given in Sec. 3.1.3.

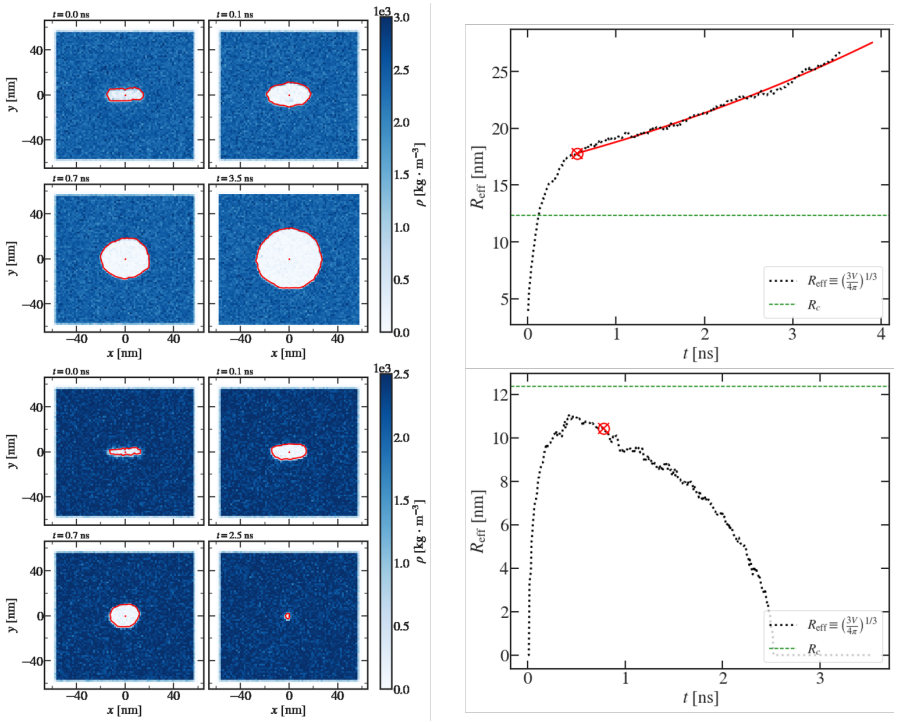

Figure 4.4: MD simulation in liquid xenon for the thermodynamics condition with 0.9 keV Seitz threshold. The upper two graphs show the 2 keV energy deposition and the lower two graphs show the 1 keV energy deposition. The left two graphs show the density of the liquid in the simulation region. The color scale indicates the liquid density in the simulation region. The right two graphs show the effective radius $R_{eff} = \sqrt[3]{3V/4\pi}$ as a function of time, where V is the volume of the bubble. The red circle represents the bubble becoming spherical and the red line represents the fit given by the differential equations in Eq. 3.18. The green dashed line is the critical radius of xenon obtained from Eq. 3.7

In this study, we conducted a MD simulation to investigate the formation and collapse of bubbles based on the variation of two key variables: the energy deposition (E_{dep}) and the cylinder length (l_{cyl}). Our goal was to determine the conditions under which bubbles form or collapse, as illustrated in Fig. 4.4. To analyze the results of bubble nucleation, we categorized them based on the linear energy density (dE/dx) and the cylinder length (l_{cyl}) in the MD simulation.

The function:

$$\langle \frac{dE}{dx} \rangle = \frac{E_{dep}}{l_{cyl}} = \frac{a}{l_{cyl}^2} + \frac{b}{l_{cyl}} + c \tag{4.7}$$

was used to fit the region between bubble formation and collapse. The parameters a, b, and c are the free parameters of the fit, which were determined based on the simulation data. Following this procedure, we have conducted analysis of various gas species used in bubble chamber experiments, enabling us to compare the results with existing data. Further details regarding the analysis of each liquid will be discussed in the subsequent sections, providing a comprehensive understanding of the bubble nucleation.

4.2.1 Liquid Xenon

The SBC experiment has a prototype that uses liquid xenon [71]. Thus, we used MD simulations to study liquid xenon, following the method described in Section 4.1. First, we calculated ϵ by the relation $\epsilon = T_c k_B / 0.935 = 4.278 \times 10^{-21}$ [J] from the critical temperature of xenon $T_c = 289.74K$ [72]. Then, we determined σ by obtaining the liquid density at the saturation state in the MD simulation at a temperature of $T = -42.9$ [°C] (0.743 [ϵ/k_B] in LJ unit), which is $\sigma = 3.97$Å. By calculating ϵ and σ, we could constrain the simulated LJ-liquid to our target liquid.

Seitz threshold	Pressure		Liquid Density	
[keV]	[psia]	$[P\sigma^3/\epsilon]$	[g/cc]	$[\rho\sigma^3/m]$
0.9	25	0.00253	2.4204	0.6951
2.06	76	0.00767	2.4258	0.6959

Table 4.2: Xenon thermodynamics properties in SI units and LJ units. The density is extracted from REFPROP [60], based on the temperature and pressure conditions of superheat. Xenon superheated temperature is fixed in -42.9 [C°] (0.743 [ϵ/k_B] in LJ unit)

To initialize the simulation, we created a superheated state with thermodynamic conditions corresponding to Seitz energy thresholds of 0.9 keV and 2.06 keV, as shown

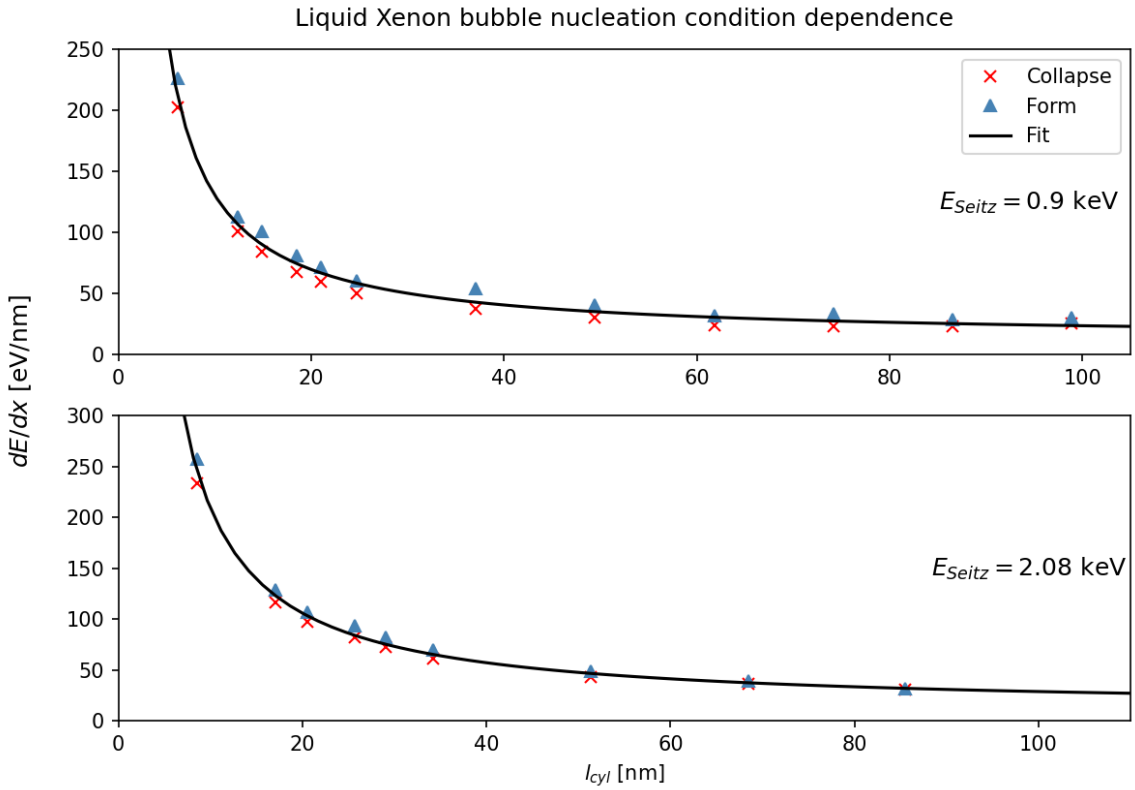

Figure 4.5: The bubble nucleation condition as a function of the linear energy density and the track length. The graphs show the xenon in the 0.9 keV and 2.06 keV Seitz threshold respectively. Red crosses indicate events where bubbles collapse, while blue triangles indicate events where bubbles form. The fitting curve is fitted by Eq. 4.7 with the average dE/dx between the form and collapse.

in Table. 4.2. The parameters used in the MD simulation in both LJ and SI units are presented there. We then varied the energy deposition E_{dep} and cylinder length l_{cyl} and summarized the results by fitting them with the function in Eq. 4.7.

Fig. 4.5 illustrates the dependence of bubble nucleation on the linear energy density dE/dx and cylinder length l_{cyl} in molecular dynamic simulations. Red crosses indicate events where bubbles collapse, while blue triangles indicate events where bubbles form. The regions between bubble formation and collapsing (i.e., the average energy density between them) are fitted with the function given in Eq. 4.7. Conversely, the lower bound is fit with the largest simulated energy density resulting in bubble collapse (red crosses). Similarly, the upper bound is fit with the lowest energy density resulting

in bubble formation (blue triangles). The fitting parameter is shown in Table. 4.3.

Seitz threshold	a [eV·nm]	b [eV]	c [eV/nm]
0.9 keV	705.86	1109.1	12.542
0.9 keV lower bound	1188.4	995.18	10.581
0.9 keV upper bound	1087.6	1116.3	17.417
2.06 keV	1503.4	1835.2	10.371
2.06 keV lower bound	1388.4	1755.1	9.6365
2.06 keV upper bound	721.58	2031.3	9.4678

Table 4.3: The xenon bubble nucleation fitting parameters obtained from Eq. 4.7 used for Fig. 4.5 shown. The lower bound is fit with the largest simulated energy density resulting in bubble collapse (red crosses) and the upper bound is fit with the lowest energy density resulting in bubble formation (blue triangles).

4.2.2 Octafluoropropane (C_3F_8)

The MD simulation of C_3F_8 was conducted following a similar procedure as employed for liquid xenon. However, C_3F_8 is a multi-atom compound, leading to a non-isotropic intermolecular potential. Considering the computational expense associated with accounting for all internal chemical bonds within the molecule, a degree of simplification was necessary for the simulation. This simplification was achieved through a method known as coarse-graining (CG), which treats the molecule as a single particle while disregarding internal interactions, including chemical bonds. CG models are MD models specifically designed to investigate the behavior of complex molecules. They enable a reduction in system complexity by focusing on relevant physical quantities while still capturing the fundamental physics at play. Notably, the CG method has been successfully applied to study the behavior of C_2ClF_5 in the context of the SIMPLE experiment [56].

To determine the interaction energy parameter ϵ, we used the relation $\epsilon = T_c k_B/0.935 = 5.095 \times 10^{-21}$ J, where T_c represents the critical temperature of C_3F_8, found to be

345.1 K in REFPROP [60]. Subsequently, to obtain the liquid density, we created a saturation state in the MD simulation at temperatures of $T = 14$ [°C] (0.778 $[\epsilon/k_B]$ in LJ unit) and $T = 16$ [°C] (0.783 $[\epsilon/k_B]$ in LJ unit), which corresponded to the experimental conditions at Seitz thresholds of 3.29 keV and 2.45 keV, respectively. From the saturated density, we determined σ to be approximately 5.38 Å. This value was then used to constrain the LJ-liquid simulation to accurately represent the target liquid. The specific values employed in the simulation are shown in Table 4.4.

Seitz threshold	Temperature		Pressure		Density	
[keV]	$[°C]$	$[\epsilon/k_B]$	[psia]	$[P\sigma^3/\epsilon]$	[g/cc]	$[\rho\sigma^3/m]$
3.29	14	0.778	106	0.0224	1.3676	0.688
2.45	16	0.7834	71	0.0146	1.3791	0.672

Table 4.4: Thermodynamic properties of C_3F_8 in both SI and LJ (Lennard-Jones) units used in MD simulation. The density values are extracted from REFPROP [60], utilizing the temperature and pressure conditions corresponding to the experimental superheated state. The listed pressure values represent the outputs obtained from the MD simulation.

The use of a coarse-graining model, such as C_3F_8, involves approximating a compound molecule with a single isotropic particle, which can result in certain deviations from the properties of the actual material. In the PICO-60 experiment [35], we controlled the temperature and pressure to achieve a superheated state. However, in the MD simulations, we regulated the temperature and density to attain the same state. When generating the superheated state in MD, the pressure becomes a dependent variable determined by temperature and density. In the case of the xenon MD simulation, the isotropic nature of the atom allows for agreement between the MD-derived pressure and the experimental pressure provided in Table 4.4. However, for C_3F_8, as shown in Table 4.4, the coarse-graining model leads to a discrepancy in the pressure estimation. Despite this discrepancy, it is important to note that the coarse-graining model remains valid and has been employed successfully in past studies [56, 63]. Con-

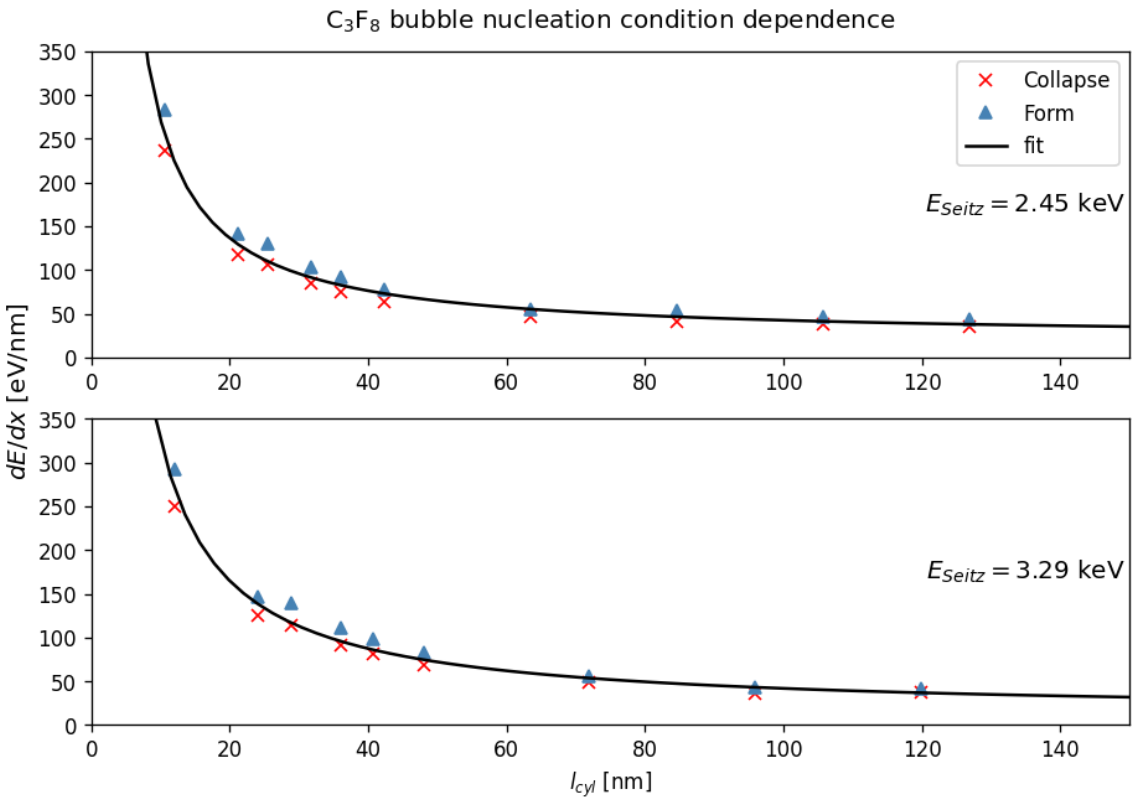

Figure 4.6: The bubble nucleation condition dependence on the linear energy density and the track length. The graphs shows the C_3F_8 in the 3.29 keV and 2.45 keV Seitz threshold. Red crosses indicate events where bubbles collapse, while blue triangles indicate events where bubbles form. The fitting curve is fitted by Eq. 4.7 with the average dE/dx between the form and collapse.

sequently, we constrained the model using real experimental temperature and density values to conduct subsequent simulations for both C_3F_8 and CF_3I.

We conduct the simulation using the experimental superheated state with Seitz thresholds of 3.29 keV and 2.45 keV. To understand the bubble nucleation threshold, we systematically vary the energy deposition E_{dep} and cylinder length l_{cyl}. The obtained results are summarized by fitting them with the function described by Eq.4.7. The dependence of bubble nucleation on these thresholds is revealed in Fig. 4.6.

Fig. 4.6 shows the relationship between bubble nucleation, linear energy density (dE/dx), and cylinder length (l_{cyl}) in our MD simulations for C_3F_8. The red crosses indicate bubble collapse events, while the blue triangles represent bubble formation

events similar to xenon results. The fitting parameter is shown in Table. 4.5.

Seitz threshold	a [eV·nm]	b [eV]	c [eV/nm]
2.45 keV	1543	2975.6	12.054
2.45 keV lower bound	112.48	2866.1	10.137
2.45 keV upper bound	32.204	3333	13.003
3.29 keV	3850.8	2111.9	21.169
3.29 keV lower bound	3131	2022.8	17.278
3.29 keV upper bound	3532.1	2433.8	22.084

Table 4.5: The C_3F_8 bubble nucleation fitting parameters obtained from Eq. 4.7 used for Fig. 4.6. The lower bound is fit with the largest simulated energy density resulting in bubble collapse (red crosses) and the upper bound is fit with the lowest energy density resulting in bubble formation (blue triangles).

4.2.3 Trifluoroiodomethane (CF_3I)

In 2015, the PICO-60 used CF_3I as a target in the search for WIMPs [64]. Thus, a MD simulation of CF_3I was conducted to verified the present model. The simulation produced $\epsilon = 5.85 \times 10^{-21}$ J and $\sigma = 6.43$Å with a critical temperature of 396.495 K and a saturation temperature of 34.5 °C.

During the experiment, the detector operated in a superheated state with a 13.6 keV Seitz threshold. To replicate this threshold condition, we used the thermodynamic parameters listed in Table 4.6.

Seitz threshold	Temperature		Pressure		Liquid Density	
[keV]	$[°C]$	$[\epsilon/k_B]$	[psia]	$[P\sigma^3/\epsilon]$	[g/cc]	$[\rho\sigma^3/m]$
13.6	34.5	0.725	23	0.0075	1.97967	0.70954

Table 4.6: CF_3I thermodynamics properties in common units and LJ units. The density is extracted from REFPROP [60], based on the temperature and pressure conditions of superheat. The listed pressure values represent the outputs obtained from the MD simulation.

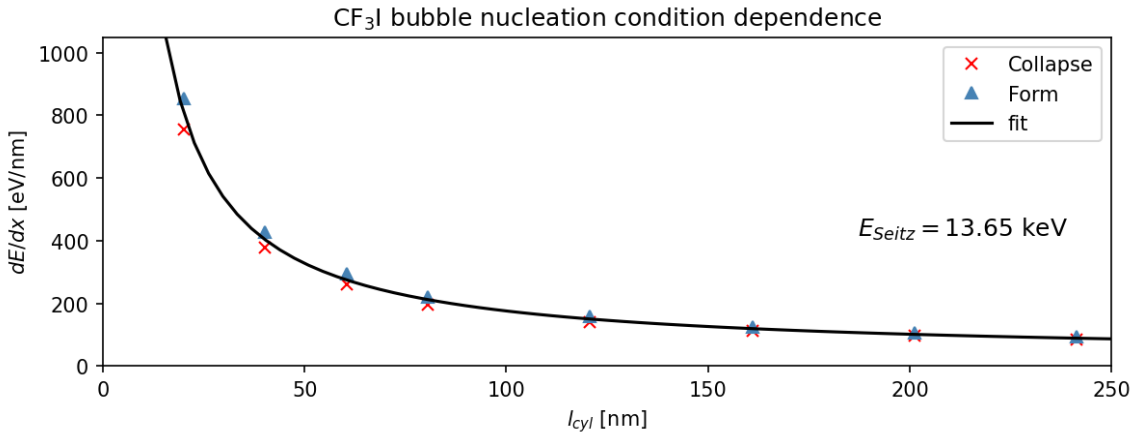

Figure 4.7: The bubble nucleation condition dependence on the linear energy density and the track length. The graphs show the C_3F_8 in the 3.29 keV and 2.45 keV Seitz threshold respectively. Red crosses indicate events where bubbles collapse, while blue triangles indicate events where bubbles form. The fitting curve is fitted by Eq. 4.7 with the average dE/dx between the form and collapse.

After creating the superheated state, we simulate various values of energy deposition (E_{dep}) and cylinder length (l_{cyl}). We obtain results and summarize them by fitting them with the function Eq. 4.7. The dependence of bubble nucleation on these thresholds is shown in Fig. 4.7, along with the fitting parameters Table. 4.7.

Seitz threshold	a [eV·nm]	b [eV]	c [eV/nm]
13.6 keV	22114	14537	28.066
13.6 keV lower bound	22114	13537	28.066
13.6 keV upper bound	22114	15537	28.066

Table 4.7: The CF_3I bubble nucleation fitting parameters obtained from Eq. 4.7used in Fig. 4.7. The lower bound is fit with the largest simulated energy density resulting in bubble collapse (red crosses) and the upper bound is fit with the lowest energy density resulting in bubble formation (blue triangles).

4.2.4 Liquid Argon

In the upcoming SBC experiment, the detector will use liquid argon to operate at a very low threshold to search for low-mass WIMPs. Following the same procedure as with liquid xenon simulation, we obtained $\epsilon = 2.227 \times 10^{-21}$ J and $\sigma = 3.4$Å. In this

work, we perform simulations at two threshold conditions, 44.5 eV and 97.3 eV, with the aim of achieving the desired experimental targets for these thresholds.

Seitz threshold	Pressure		Liquid Density	
[keV]	[psia]	$[P\sigma^3/\epsilon]$	[g/cc]	$[\rho\sigma^3/m]$
44.5	20	0.002466	1.035	0.639
97.3	100	0.1233	1.046	0.646

Table 4.8: Liquid argon thermodynamics properties in SI units and LJ units. The density is extracted from REFPROP [60], based on the temperature and pressure conditions of superheat. Argon superheated temperature are fixed in -143.15 [C°] (0.806 $[\epsilon/k_B]$ in LJ unit)

Once the superheated state was created, we conducted simulations with various values of energy deposition (E_{dep}) and cylinder length (l_{cyl}). We then summarized the results by fitting them to the function given in Eq. 4.7. The relationship between bubble nucleation and these thresholds is shown in Fig. 4.8, and the fitting parameters are provided in Table. 4.9.

Seitz threshold	a [eV·nm]	b [eV]	c [eV/nm]
44.5 eV	15.834	31.109	2.7416
44.5 eV lower bound	14.617	26.638	2.7928
44.5 eV upper bound	14.770	36.878	2.6474
97.3 eV	0.62748	122.00	2.8496
97.3 eV lower bound	1.1863	111.63	2.9051
97.3 keV upper bound	1.6679	131.52	2.8864

Table 4.9: The liquid argon bubble nucleation fitting parameters obtained from Eq. 4.7used in Fig. 4.8. The lower bound is fit with the largest simulated energy density resulting in bubble collapse (red crosses) and the upper bound is fit with the lowest energy density resulting in bubble formation (blue triangles).

Moving on to the next chapter, we will discuss the travel of the recoiling nucleus in the target material after the nuclear recoil. A fraction of the incident ion's energy is

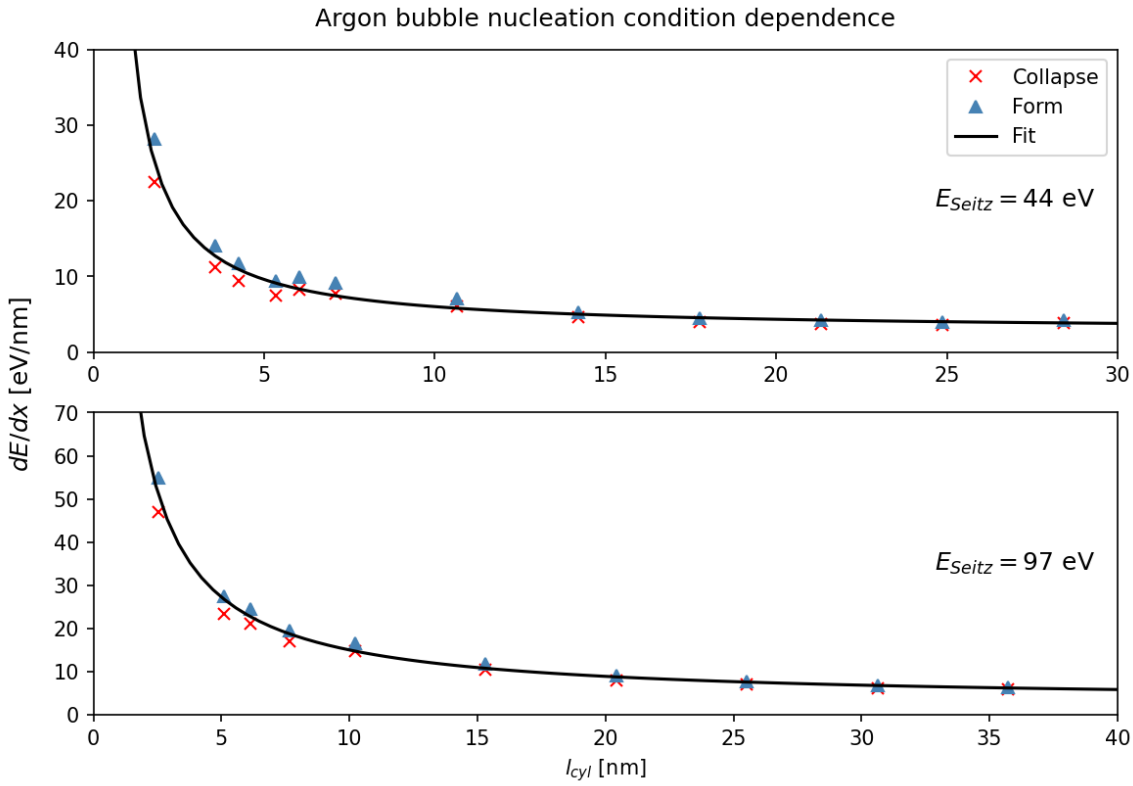

Figure 4.8: The bubble nucleation condition dependence on the linear energy density and the track length. The graphs show the argon in the 44.5 eV and 97.3 eV Seitz threshold respectively. Red crosses indicate events where bubbles collapse, while blue triangles indicate events where bubbles form. The fitting curve is fitted by Eq. 4.7 with the average dE/dx between the form and collapse.

transferred into the target material, which can contribute to the formation of bubbles as we discussed in this chapter. We will introduce the Monte Carlo simulation and the theoretical models that describe the interaction and the energy transfer.

Chapter 5

Recoil ion in matter simulation

MD can provide the insights into the mechanism of bubble nucleation. The initial trigger for nucleation is the deposition of energy, typically in the form of heat, known as the heat spike. This surge in temperature is a result of momentum transfer from the initial ion, which is ionized due to nuclear recoil. Hence, comprehending the efficiency of bubble nucleation requires a profound understanding of how energy is transferred from the incident ion to the target medium. This chapter provides an introduction and discussion of Monte Carlo (MC) simulation tools used to study and analyze energy transfer in different target materials. By employing MC simulations, we can reproduce and explain the shape of the efficiency curve.

5.1 SRIM

Stopping and Range of Ions in Matter (SRIM) and its Monte Carlo subprogram, Transport of Ions in Matter (TRIM), are simulation tools used to model interactions between ions and their target material [73]. These simulations are used to study the behavior of ions when they collide with solid or liquid targets.

In SRIM/TRIM simulations, the incident ion is assigned a specific energy and direction, and the simulation calculates the ion's trajectory as it traverses the target material. Throughout its journey, the ion undergoes collisions with atoms in the target, resulting in a cascade of recoiling atoms. The SRIM/TRIM simulation uses

universal nuclear-scattering cross-sections, as provided by Ziegler [73], which quantitatively measure the probability of a collision leading to a recoil event.

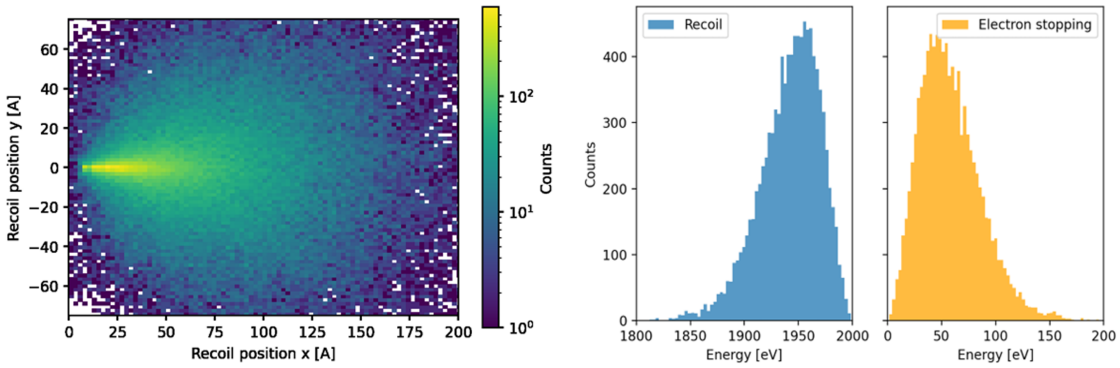

Figure 5.1: Example of 2 keV xenon ions in the xenon target simulated in SRIM. The graph on the left shows the distribution of the position of recoiling ions. The histogram on the right shows the energy loss of the ion in the atomic motion through recoiling or electron stopping.

Fig. 5.1 shows an example of the energy deposition of 2 keV xenon ions in a xenon target. The SRIM/TRIM simulation output includes the energy and position of the recoiling atoms, which can be used to calculate the heat generated by the ion's interactions with the target atoms. This heat can contribute to the formation of bubbles in the target material. The remaining energy of the incident ion is either lost through electronic excitation or ionization, which can contribute to the scintillation.

5.2 RustBCA

RustBCA is a newly developed package for simulating ion-material interactions using the binary collision approximation (BCA) [74]. Similar to the SRIM/TRIM software, Fig. 5.2 shows an example of the energy deposition of 2 keV xenon ions in a xenon target. However, RustBCA's source code is built using Rust, a modern programming language that overcomes common challenges associated with conventional scientific computing languages. This enhances RustBCA's overall functionality and reliability. Moreover, the code is open source and can be used for more flexible purposes.

BCA codes are typically valid within a range of incident ion energies spanning from

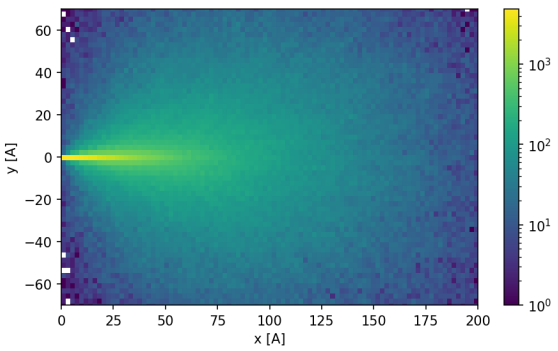

(a) The distribution of the position of recoiling ions.

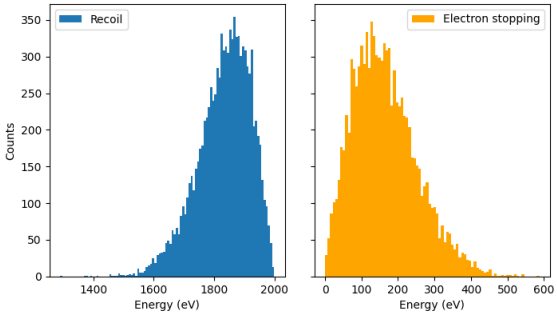

(b) The histogram shows the energy loss of the ion in the atomic motion through recoiling or electron stopping.

Figure 5.2: Example of 2 keV xenon ions in the xenon target simulated in RustBCA

around 10 eV to several GeV. However, RustBCA yields satisfactory outcomes even at substantially lower energy levels, as validated by conducted tests. By representing the collision cascade as a series of binary collisions, BCA codes can effectively simulate reflection, implantation, sputtering, transmission, and displacement damage accurately and efficiently.

Using the RustBCA codebase, we can perform similar calculations to those done in SRIM/TRIM to simulate ion interaction in the target and extract the energy that contributes to heat to study bubble nucleation. However, the major disadvantage of RustBCA is that it doesn't return information about which atom the initial ion scattered with if the target consists of more than one element. Nevertheless, we can still uses it to compare with SRIM to avoid bias from the simulation code.

5.3 Lindhard Model

To understand the underlying mechanism of energy transfer, we need to understand the theoretical model. When a neutron or WIMP undergoes elastic scattering with a target nucleus, the resulting recoiling nucleus traverses the target material. The energy loss per unit length of the nucleus is called the stopping power, which consists of two mechanisms. On one hand, energy dissipation can occur via electronic excita-

tion or further ionization caused by interactions with the electron cloud surrounding the target atoms, and we usually call it the electronic stopping power. Ultimately, this energy deposition contributes to scintillation or fluorescence. On the other hand, another portion of the energy is dissipated through momentum transfer via elastic collisions with other nuclei in the material, and we usually call it the nuclear-stopping power. These collisions prompt additional ionization, and the resulting primary ions create cascades of successive interactions. This momentum transfer from recoiling contributes to the generation of a localized heat spike.

The energy loss is commonly described by Lindhard's model [75]. Lindhard derived an integro-differential equation that describes the total electronic energy loss in a nuclear recoil cascade, in terms of the differential elastic nuclear-scattering cross-section and the electronic stopping power for recoiling nuclei. This equation provides a means for calculating the energy lost to electronic excitation during a nuclear recoil event [76]. The electronic stopping power for low-velocity ions is given by Lindhard's equation:

$$\begin{aligned} S_{\mathrm{e}} =& \xi_{\mathrm{e}} \times 8\pi N e^2 a_0 \frac{Z_1 Z_2}{\left(Z_1^{2/3} + Z_2^{2/3}\right)^{3/2}} \frac{v}{v_0} \\ &= \xi_{\mathrm{e}} \times 8\sqrt{2}\pi N \hbar c a_0 \frac{Z_1 Z_2}{\left(Z_1^{2/3} + Z_2^{2/3}\right)^{3/2}} \sqrt{\frac{E}{mc^2}} \\ &\text{with} \quad \xi_{\mathrm{e}} \approx Z_1^{1/6}, \end{aligned} \tag{5.1}$$

where Z is the atomic number, subscript 1 represents the incoming ion and subscript 2 represents the target medium atoms, a_0 is the Bohr radius, N is the number density of atoms in the target medium, E is the kinetic energy of the ion, m is the mass of the ion, e is the electron charge, $\hbar$ is the reduced plank constant, v is the velocity of the projectile ion and $v_0 = c/137$ where c is the speed of light and $1/137$ is associated with the fine structure constant. If the target and projectile are the same elements $Z_1 = Z_2 = Z$:

$$S_e = 4\pi N\hbar c a_0 Z^{7/6}\sqrt{\frac{E}{mc^2}}. \tag{5.2}$$

Lindhard [77] solved the problem with the dimensionless reduced linear energy transform:

$$(\frac{\epsilon}{\rho})_{el} = k\epsilon^{1/2} \tag{5.3}$$

where ϵ and ρ are the dimensionless reduced energy and range respectively, and k is a parameter associated with the electronic stopping power. Hitachi expressed that for most cases [78], $k = 0.1 \sim 0.2$. He calculated $k_{\mathrm{C}} = 0.127$ for carbon and $k_{\mathrm{F}} = 0.132$ for fluorine in CF_4 by using:

$$k = 0.133Z^{2/3}A^{-1/2} \tag{5.4}$$

where A is the atomic number. We are using the same k values for C_3F_8 in our model since it is made of the same atoms and we vary the uncertainty between 0.1 and 0.2.

The reduced energy can be expressed as:

$$\varepsilon = \frac{a_{\mathrm{s}}A_2}{Z_1Z_2e^2\left(A_1 + A_2\right)}E \tag{5.5}$$

where a_s is the screening radius proposed by Lindhard [77]:

$$a_{\mathrm{s}} = 0.8853a_0/\left(Z_1^{2/3} + Z_2^{2/3}\right)^{1/2} \tag{5.6}$$

For monotonic atoms $Z_1 = Z_2 = Z$, we have $\epsilon = 11.5\left(E_{nr}/keV\right)Z^{(-7/3)}$.

The friction of nuclear recoil energy contributing to the electronic excitation is called the Lindhard factor or quenching factor. The numerical solution of the Lindhard factor is approximated by:

$$\mathcal{L} = \frac{E_e}{E_n + E_e} \approx \frac{kg(\epsilon)}{1 + kg(\epsilon)} \tag{5.7}$$

where

$$g(\epsilon) = 3\epsilon^{0.15} + 0.7\epsilon^{0.6} + \epsilon$$

E_n is the energy loss in nuclear stopping, E_e is the energy loss in electronic stopping. Hitachi [79] approximated the Lindhard factor of a compound with the ratio of $\mathcal{L}$ for each element, such as for C_3F_8, $\mathcal{L}(C_3F_8) = (3\mathcal{L}(C) + 8\mathcal{L}(F))/11$. For the case of liquid xenon, we use NEST (Noble Element Simulation Technique) [80] package to calculate the Lindhard factor. NEST fits the empirical functions from various experimental data.

Due to quantum fluctuations, the energy transferred to the nucleus or electrons will have a probability distribution with a straggling. The relative straggling (variance) of energy that goes to the electronic stopping sector, with low energy approximation, is given by [77]:

$$\Omega_E^2/E_{nr}^2 = \frac{1}{14}\gamma\left\{\left(\frac{\gamma^{1/2}}{C_A E_c^{1/2}} - \frac{7}{4}\right)^2 + \frac{7}{16}\right\} \tag{5.8}$$

therefore the straggling of the Lindhard factor can be determined as:

$$\Omega_L^2 = \frac{\mathcal{L}}{14}\gamma\left\{\left(\frac{\gamma^{1/2}}{C_A E_c^{1/2}} - \frac{7}{4}\right)^2 + \frac{7}{16}\right\} \tag{5.9}$$

where

$$C_A = 2/3\left\{{E_{1c}}^{-1/2} + \frac{1}{2}\gamma^{1/2}{E_c}^{-1/2}\right\}$$

$$E_{1c} \cong {A_1}^3\left(A_1 + A_2\right)^{-2} Z^{4/3}{Z_1}^{-1/3} \cdot 500\text{eV}$$

and

$$E_{2c} \cong \left(A_1 + A_2\right)^2 A_1^{-1} Z_2 \cdot 125\text{eV}$$

where $Z^{2/3} = Z_1^{2/3} + Z_2^{2/3}$, $E_c = \gamma E_{2c}$ and $\gamma = 4A_1A_2/\left(A_1 + A_2\right)^2$. The Lindhard factor of C_3F_8 and Xe as a function of energy with straggling (Ω_L) is shown in Fig. 5.3.

5.4 Analysis and correction

By using both SRIM and RustBCA software, we are able to conduct Monte Carlo (MC) simulations to analyze the extent to which energy contributes to bubble nucleation. The inherent quantum fluctuations in the system introduce randomization in energy transfer and ion track length, thereby affecting the nucleation efficiency. To

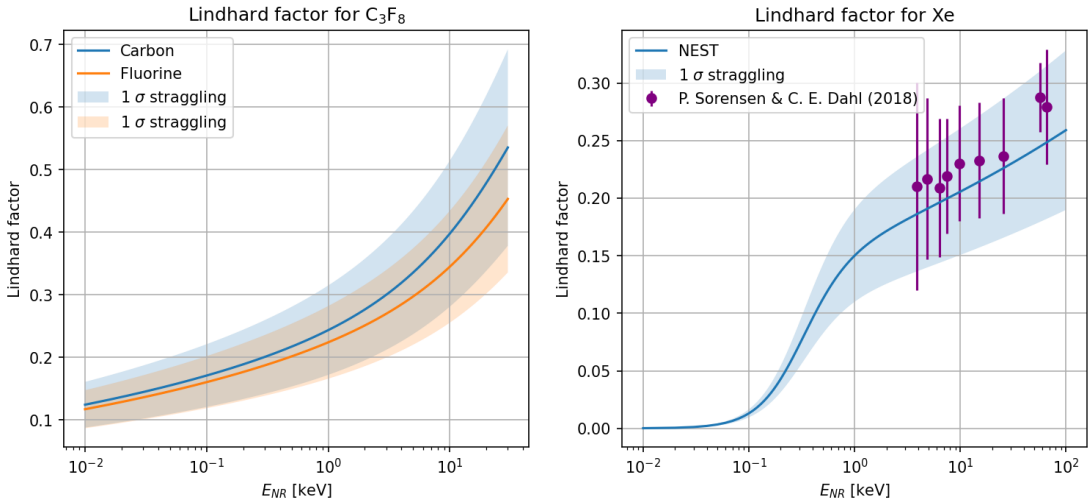

Figure 5.3: C_3F_8 and Xe Lindhard factor as a function of nuclear recoil energy. C_3F_8 is calculated by Eq. 5.7 ($k_C = 0.127, k_F = 0.132$), and Xe is calculated by NEST [80]. The Xe data is also compared with experimental data from Sorensen and Dahl [81]. The error band is 1σ straggling of the Lindhard factor calculated by Eq. 5.9.

validate our simulation tool and the way we interpret the simulation data, it is crucial to incorporate Lindhard's theory as a benchmark in our analysis. This will allow us to determine if the simulation results align with the expected outcomes predicted by the theoretical model.

In the MC simulation, in both SRIM and RustBCA, numbers of ions with assigned energy were sent into the target, as illustrated in Fig. 5.4. Each incoming ion undergoes multiple elastic scattering events with the target nuclei (depicted as blue circles), which in turn leads to the creation of secondary recoiling ion (depicted as pink circles). Between each recoiling event, the initial ion gradually loses energy as it interacts with the electron cloud surrounding the target atoms, e.g. electronic stopping (indicated by the dashed line). The secondary ions, generated by the incident nucleus, also experience energy loss along their trajectories following the same principle. The red dashed line represents their energy loss due to electronic excitation, while the pink circle represents a recoiling event. Eventually, one ion leads to a cascade of interaction.

According to the Lindhard model, nuclear recoil energy can be deposited either

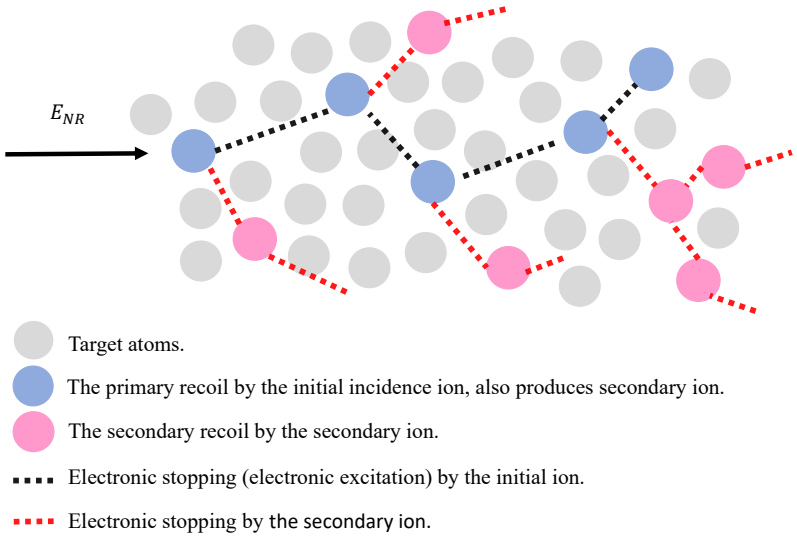

Figure 5.4: Diagram showing the cascade created by the incident nucleus. The grey circles represent the target atoms, while the blue circle indicates the recoiling of the target nucleus due to the incident nucleus. The pink circles represent the secondary recoil scatter by the secondary ions. The black dashed line represents the energy loss due to electronic stopping by the incident nucleus, while the red dashed line is the electronic loss of the secondary ion.

through nuclear stopping or electronic stopping. Only the portion of energy attributed to nuclear stopping is responsible for generating the heat spike required for bubble formation. However, when comparing the energy distribution allocated to the electronic stopping, we observe inconsistencies with the predictions of the Lindhard theory.

As we can see from Fig. 5.5, the Lindhard factor calculated by both simulation tools is significantly smaller than the theoretical value. The discrepancy arises because the simulation tools only track the energy loss of the primary ion (e.g. incidence ion). We consider all of its nuclear energy loss as the contributor to the heat spike, as indicated by the blue circle in Fig. 5.4. However, this portion of the energy is subsequently carried by the secondary ions, which can also dissipate energy through electronic stopping as they travel, illustrated by the red dashed line in Fig. 5.4.

To overcome this issue, we need to implement corrections that account for the energy losses incurred during the process of electronic stopping. Consequently, when considering the energy of the secondary ion with index i in a nuclear recoil event, we can describe it as follows:

$$E_{i,n} = E_i(1 - \mathcal{L}(E_i)) \tag{5.10}$$

where $E_{i,n}$ represents the nuclear stopping energy loss experienced by the secondary ion with index i, E_i the initial energy of the secondary ion and $\mathcal{L}$ is the theoretical Lindhard factor. The Lindhard factor is a function that encapsulates the dependency of energy loss on nuclear recoil energy. Since the Lindhard factor $\mathcal{L}$ represents the fraction of energy loss due to electronic stopping, the remaining contributes to nuclear stopping.

By implementing this correction, we can establish a benchmark for our simulations using the theoretical Lindhard model. Through the summation of the energy of all recoiling secondary ions, we can determine the amount of energy that contributes to both nuclear stopping and the resulting heat spike. The Lindhard factor, derived

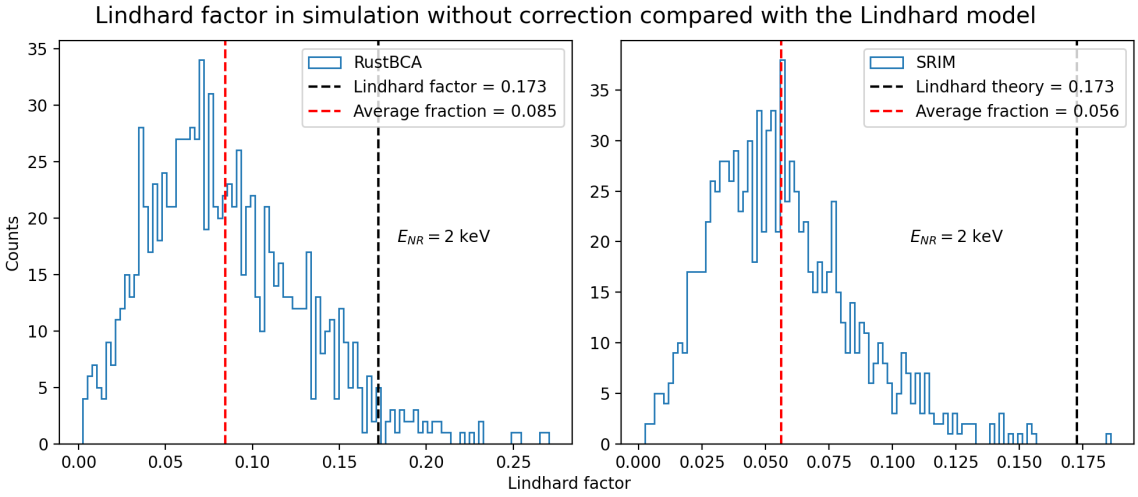

(a) Distribution of energy loss fractions dissipated to electronic stopping (e.g., Lindhard factor) in 2 keV nuclear recoil events in liquid xenon (LXe), simulated using RustBCA (left) and SRIM (right). The black dashed line represents the theoretical Lindhard factor at 2 keV nuclear recoil energy, and the red dash line is the mean of the distribution.

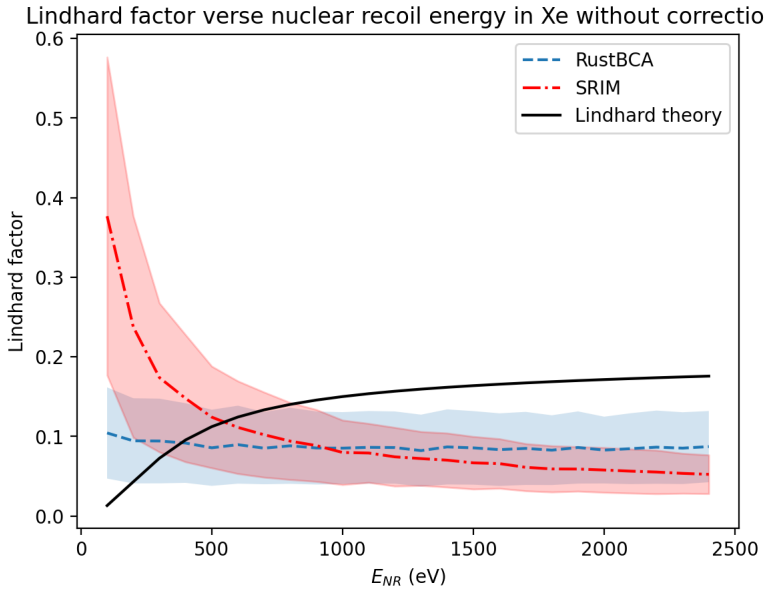

(b) Lindhard factor versus nuclear recoil energy without correction. The red dashed line corresponds to the simulation generated by SRIM, while the blue dashed line represents the simulation produced by RustBCA. The theoretical value is obtained from NEST. The shaded error band represents the 1-σ from the distribution from histogram (a).

Figure 5.5: Simulation results without considering for the energy lost from the secondary ions.

from the simulation, can be expressed as:

$$L = 1 - \frac{\sum_i E_{i,n}}{E_{nr}} \tag{5.11}$$

As depicted in Fig. 5.6, the simulation results are compared to the theoretical Lindhard factor. It is observed that the simulations generally align with the theoretical values, except for energies smaller than 500 eV. The discrepancy may occur due to the insufficient energy of the primary ion to create numbers of secondary ions, so the faction of energy contributing to the electronic stopping is over estimated. However, this lower energy range only has small impact on the simulated data in higher energy region. The Lindhard factor in the lower energy range remains an active subject of research due to some inconsistencies between experimental observations and theoretical predictions [37].

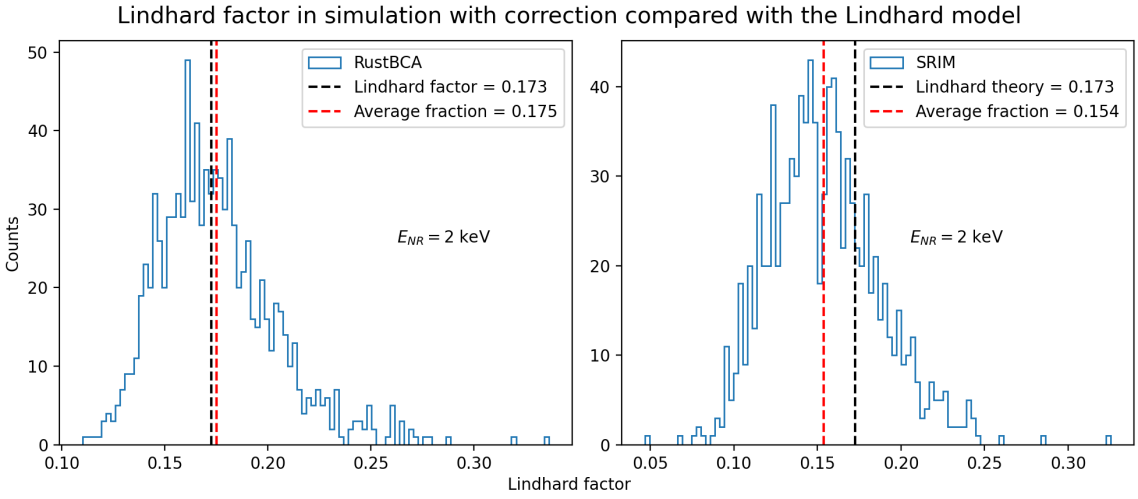

(a) Distribution of energy loss fractions dissipated to electronic stopping (e.g., Lindhard factor) in 2 keV nuclear recoil events in liquid xenon (LXe) with correction, simulated using RustBCA (left) and SRIM (right). The black dashed line represents the theoretical Lindhard factor at 2 keV nuclear recoil energy, and the red dashed line is the mean of the distribution.

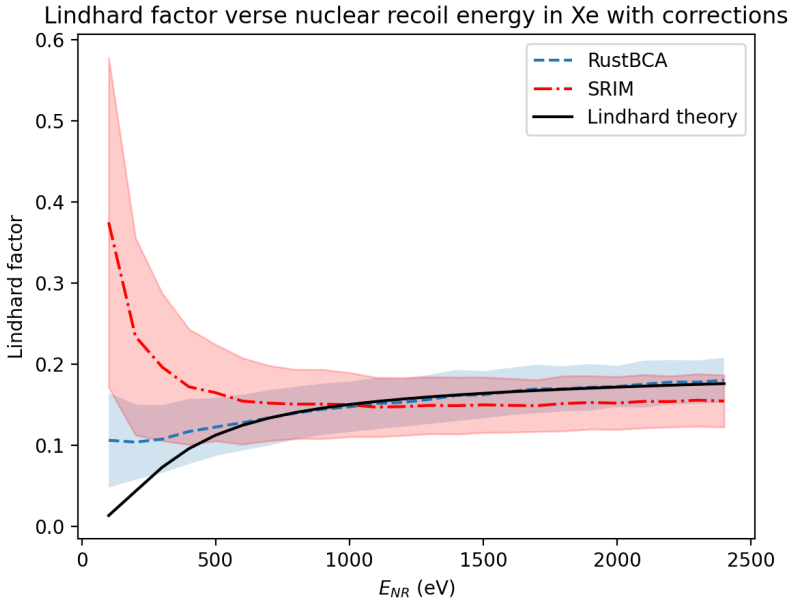

(b) Lindhard factor versus nuclear recoil energy with correction. The red dashed line corresponds to the simulation generated by SRIM, while the blue dashed line represents the simulation produced by RustBCA. The theoretical value is obtained from NEST. The shaded error band represents the 1-σ from the distribution from the histogram (a).

Figure 5.6: Simulation results using consideration for the energy lost from the secondary ions.

Chapter 6

New model of bubble nucleation efficiency

In Chapter. 4, we explore the use of MD to determine the specific conditions that dictate the growth or collapse of a bubble. These conditions depend on both track length and energy deposition.

To concisely represent the bubble nucleation condition, we use a fitting function defined by Eq. 4.7. This fitting function enables us to describe that if the linear energy density dE/dx of a nuclear recoil event is above the threshold given by Eq. 4.7, the bubble will form. Conversely, if the linear energy density is below this threshold, the bubble will collapse.

Following the Chapter. 5, we will discuss the use of MC simulations to study how energy is deposited into the target, along with the correction for secondary ionization using the Lindhard model. Recall the energy for each secondary ions the Eq. 5.10, if we sum up all of the secondary ion that lost energy through nuclear stopping, we get the amount of energy that would contribute to the heat spike:

$$Q = \sum_i \left(1 - \mathcal{L}(E_i)\right) E_i \tag{6.1}$$

where E_i represents the energy of the secondary ion or the recoil energy caused by the incident ion, which is the calculation output in SRIM and RustBCA simulation. The Lindhard factor $\mathcal{L}(E_i)$ is a function of energy that depends on the recoil energy.

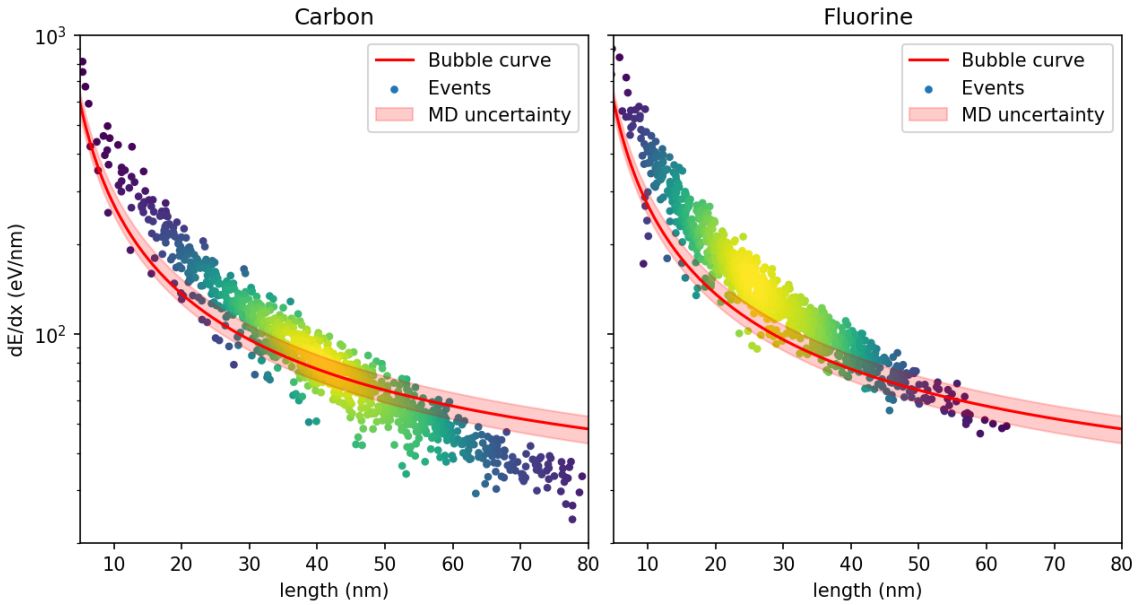

Figure 6.1: Example of 6 keV nuclear recoil events compared with the linear energy density fitting curve for C_3F_8 at a 3.29 keV thermodynamic threshold. The y-axis represents the linear energy density and the x-axis represents the track length. The red curve represents the fitting linear energy density fit using Eq. 4.7, which governs the bubble formation for C_3F_8. The scatter points are the simulated events produced in SRIM. The left graph represents the carbon recoiling events, and the right plot shows the fluorine recoiling events.

On the other hand, we have the trajectory of the incident nucleus, so the average linear energy transform is given by:

$$\left(\frac{dE_{dep}}{dx}\right)_{avg} = \frac{Q}{l_c} \tag{6.2}$$

where Q is the energy loss in heat in Eq. 6.1 and l_c is the track length varying for different events. Therefore, we can determine if a given event from the MC simulation satisfies the conditions necessary for bubble formation. In other words, if the energy density in an event exceeds the curve shown in Fig. 6.1, the formation of a bubble is considered to occur. Conversely, if the energy density falls below the curve depicted in Fig. 6.1, the bubble is considered to collapse.

Furthermore, the example presented in Fig. 6.1 reveals the energy density dE_{dep}/dx and the track length of 6 keV carbon and fluorine ions in C_3F_8. Although both carbon

and fluorine ions possess the same initial energy, fluorine ions have a higher stopping power, enabling them to be stopped within a shorter distance. Thus, fluorine ions display a higher energy deposition density compared to carbon ions. Moreover, it is observed that fluorine ions generate a greater number of events above the bubble formation curve obtained with Eq. 4.7, indicating that bubble formation is more readily achieved with fluorine recoil. The nucleation efficiency can be calculated from the MC by:

$$\varepsilon = \frac{\#\text{ of events above the curve}}{\#\text{ of total events}} \tag{6.3}$$

where ε is the efficiency for a given nuclear recoil energy. It is determined by the number of events above the fitting function divided by the total number of events. For 6 keV carbon and fluorine recoiling ions in C_3F_8, 47% of carbon recoil events and 94% of fluorine recoil events exceed the expected curve. Therefore, the bubble nucleation efficiency for carbon and fluorine recoil is 47% and 94%, respectively. Using this principle, we can model the nucleation efficiency as a function of nuclear recoil energy and compare this model with experimental results.

6.1 Experimental comparison

This presents the comparison between our new model with experimental results from SBC liquid xenon's prototype chamber that used liquid xenon [71], as well as the PICO experiments that used C_3F_8 [64] and CF3I [35].

6.1.1 Liquid Xenon

We performed MD simulations to obtain the energy density function described by Eq. 6.2 with parameter in Table. 4.3, which governs bubble formation at thermodynamic thresholds of 0.9 keV and 2.06 keV. The corresponding thermodynamic conditions and liquid properties used in the MD simulation are shown in Chapter 4 Section 4.2.1, specifically in Table 4.2.

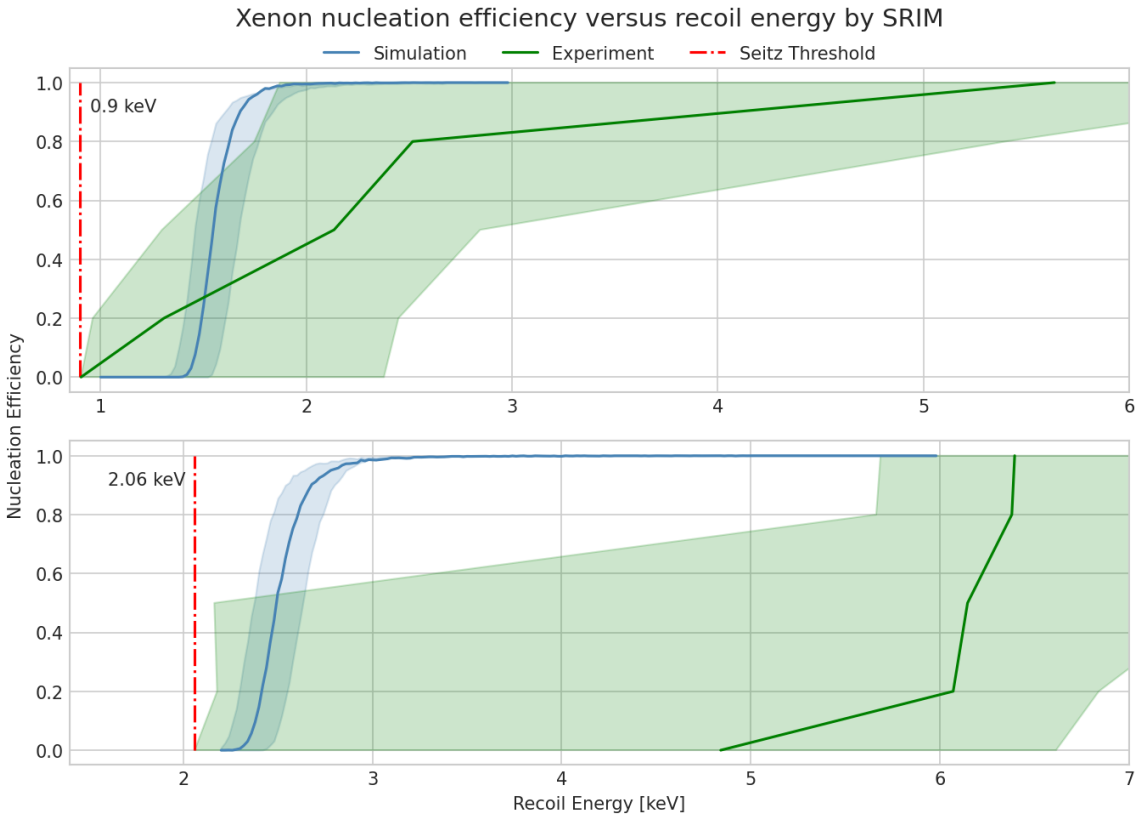

Figure 6.2: Xenon bubble nucleation efficiency as a function of energy by using SRIM. Three graphs show the bubble nucleation efficiency with a Seitz threshold (red dash lines) of 0.9 keV, and 2.06 keV respectively. The blue curve is the calculation done in the present work with MD, SRIM and the Lindhard correction. The green curve represents the experimental result obtained by MCMC calculation. Their associated errors are described in the text.

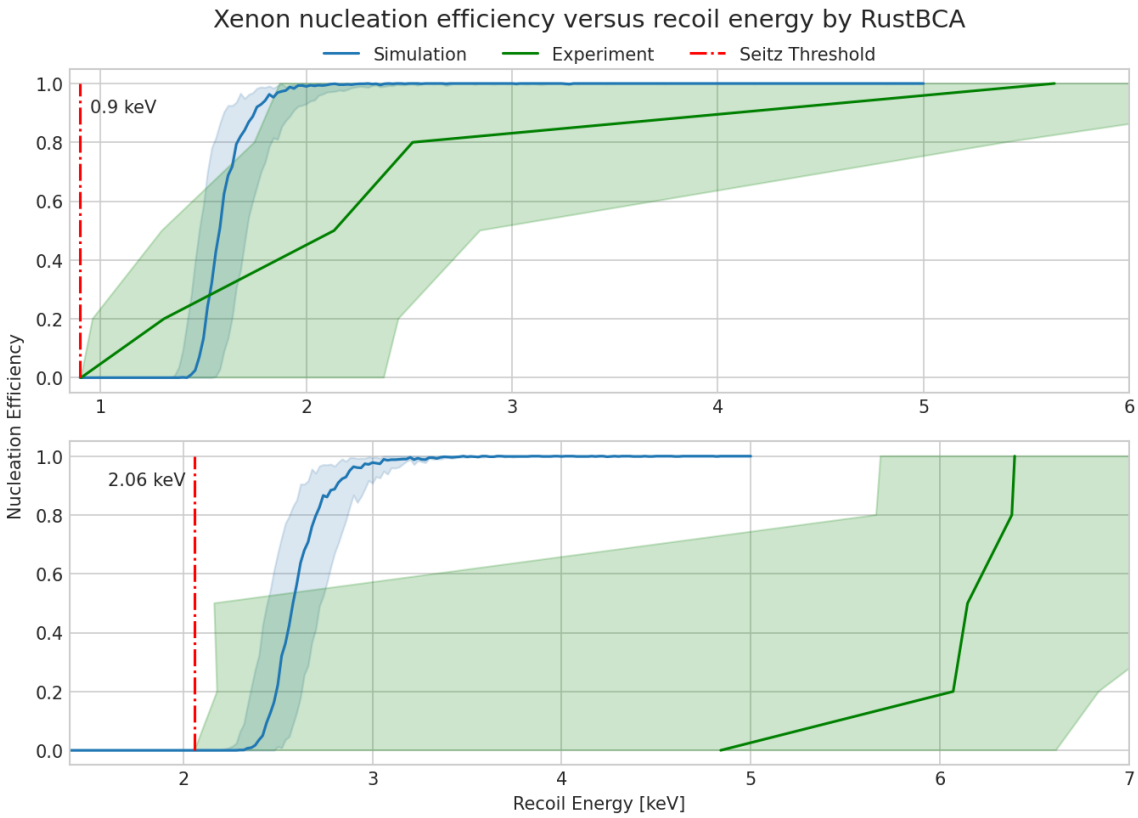

Figure 6.3: Xenon bubble nucleation efficiency as a function of energy by using RustBCA. Three graphs show the bubble nucleation efficiency with a Seitz threshold (red dash lines) of 0.9 keV and 2.06 keV respectively. The blue curve is the calculation done in the present work with MD, RustBCA with the Lindhard correction. The green curve represents the experimental result obtained by MCMC calculation. Their associated errors are described in the text.

The first results show the liquid xenon nucleation efficiency under different threshold conditions. Fig. 6.2 gives the nucleation efficiency with a Seitz threshold of 0.9 keV and 2.06 keV respectively. The simulated results represented by the blue curve in Fig. 6.2 are the calculation procedures obtained in the previous section, including MD in LAMMPS, MC simulation in SRIM, and the secondary recoiling correction by the Lindhard factor. The experimental best fit is analyzed by Markov Chain Monte Carlo (MCMC) approached by Durnford and Piro [66]. The experiment is based on SBC collaboration's LXe prototype chamber [71].

Moreover, we also performed the MC simulation using RustBCA to cross-check

if there is any bias from the simulation tools. Fig. 6.3 represents the nucleation efficiency using MD simulation in LAMMPS and MC simulation in RustBCA. The results are mostly consistent between the two MC simulations.

The error estimation in our new calculation incorporates both the upper and lower limits of the function defined by Eq. 4.7, which governs the formation of bubbles. The upper limit is determined by fitting the function to the MD simulated data that represents the minimum energy density required for bubble formation. Conversely, the lower limit is obtained by fitting the function to the MD simulated data that represents the maximum energy density that leads to bubble collapse. Additionally, there is a component of statistical error resulting from the inherent randomness of the Monte Carlo simulations. To quantify this statistical uncertainty, we employed the Bootstrap method. However, it is important to note that the magnitude of this statistical uncertainty is comparatively small when compared to the error arising from the upper and lower limits.

The obtained results align well with the initial rising trend observed in the experimental efficiency curve. For the 0.9 keV threshold condition, the curve calculated using our model mostly agrees with the experimental result within the 1σ error band. However, it should be noted that for the 2.06 keV threshold condition, the uncertainty of the results in this study appears to be underestimated, particularly in the high-efficiency regions. Nonetheless, within the 1σ error band, the experimental curve and the simulation show good agreement for efficiencies below 50%. Above this threshold, the experimental analysis reveals a sharp increase in the energy required to nucleate the bubble, exceeding 10 keV. These observations indicate the need for further investigation to gain a deeper understanding of the underlying physics governing these phenomena.

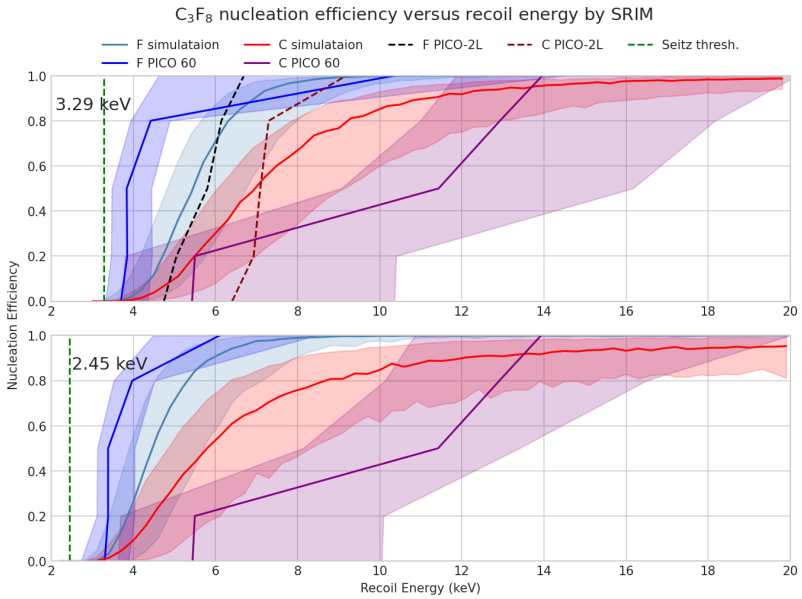

(a) The nucleation efficiency of C_3F_8 obtained with MD, SRIM and Lindhard correction. The two dashed curves are the analysis results from PICO-2L [64].

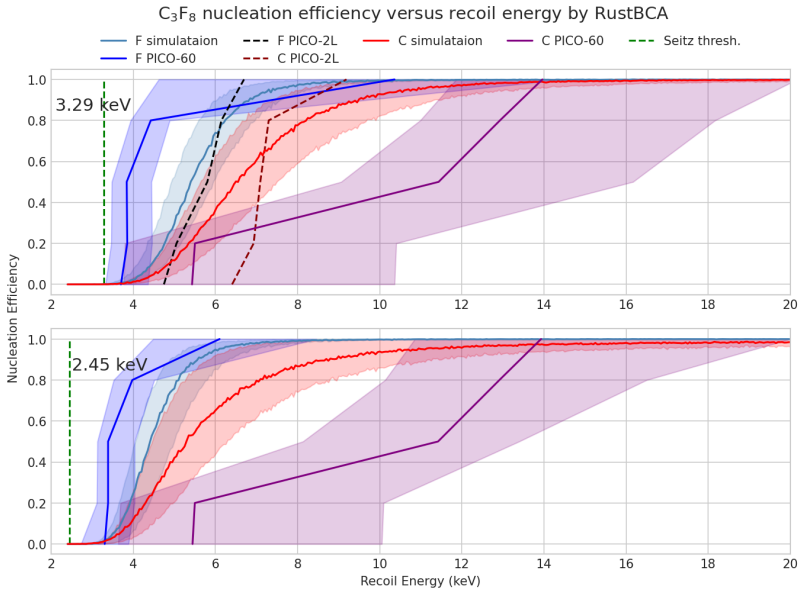

(b) The nucleation efficiency of C_3F_8 obtained with MD, RustBCA and Lindhard correction.

Figure 6.4: Two subplots in each graph show nucleation efficiency with a Seitz threshold of 3.29 keV and 2.45 keV (green vertical line) respectively. The blue curve shows the nucleation efficiency of fluorine nuclei, while the red curve shows the one for carbon, both obtained with the calculation in this work. The deep blue and purple curves are the experimental results for fluorine and carbon recoil, respectively, obtained by MCMC analysis [66].

6.1.2 Octafluoropropane (C_3F_8)

We conducted MD simulations of C_3F_8 using the same methodology as described in the previous chapter and a prior study [63]. The parameters employed in the LAMMPS simulations are presented in Table 4.4. To simulate nuclear recoil, carbon and fluorine ions were simulated with SRIM and RustBCA. The formation of bubbles was determined by comparing the energy density versus the track length of events with the curve defined by Eq.4.7. The resulting C_3F_8 nucleation efficiency curves using SRIM and RustBCA are depicted in Fig. 6.4a and Fig. 6.4b respectively. These simulation results are compared to the best-fit experimental data obtained via MCMC analysis of the PICO-60 [67] . The error bands were calculated using the same method as described in the previous section for liquid xenon.

In the SRIM results presented in Fig. 6.4a for a threshold of 3.29 keV, the fluorine recoil simulation aligns well with the experimental analysis within the low and high-efficiency regions, falling within a 1σ error band. However, it is observed to be approximately 1.5σ higher than the experimental analysis near 60% efficiency. For the 2.45 keV threshold, the fluorine ion efficiency curves obtained from both the experiment and our simulations reveal good agreement within a 1σ error band. Regarding the carbon simulation, it matches the experimental analysis in both low and high-efficiency regions. However, there is a deviation between 30% and 90% efficiency, with energy approximately 1 to 2σ lower than the experimental value.

Comparing the results obtained using RustBCA in Fig. 6.4b, it should be noted that RustBCA does not provide information on which nucleus the ion scatters with. Consequently, the discrepancy between carbon and fluorine is smaller compared to the results obtained using SRIM. The simulation curve for fluorine recoil demonstrates good agreement with the experimental curve within a 1σ range for both the 2.45 keV threshold conditions. However, the RustBCA simulation results for carbon do not align as well as those from SRIM, and further investigation is needed.

6.1.3 Trifluoroiodomethane (CF_3I)

By performing the same procedure, we also obtain the nucleation efficiency for CF3I. The resulting nucleation efficiency curves for CF3I, obtained from SRIM and RustBCA simulations, are depicted in Fig. 6.5a and Fig. 6.5b respectively. These simulation results are then compared to experimental data obtained through the neutron calibration result from the COUPP [82] and PICO-60 experiment [64]. Error bands were computed using the same methodology as xenon and C_3F_8.

Analyzing the SRIM results presented in Fig. 6.5a, we observe that the iodine recoil simulations exhibit a close alignment with the experimental results obtained from both the PICO-60 experiment (gray curve) and the COUPP iodine efficiency data (brown data points) within a 1σ confidence interval for efficiencies exceeding 60%. However, below 60% efficiency, there is a notable discrepancy between the iodine simulation results and the experimental data. Regarding the fluorine recoil, the experimental results demonstrate agreement with the simulation when the efficiency is below 50%. However, as the energy increases, the efficiency of the simulation begins to plateau, deviating from the experimental trend. The case of carbon recoil show a slower increase in efficiency compared to the experimental result, indicating a disagreement between the two.

The analysis of the simulation results using RustBCA reveals similar findings, which effectively eliminates potential bias arising from the simulation tools. While the analysis of the simulation results using RustBCA demonstrates a consistent agreement with SRIM, it is important to acknowledge the areas where discrepancies between the simulation and experimental data persist. These inconsistencies highlight the need for further investigation to better understand the underlying causes and mechanisms governing the observed differences.

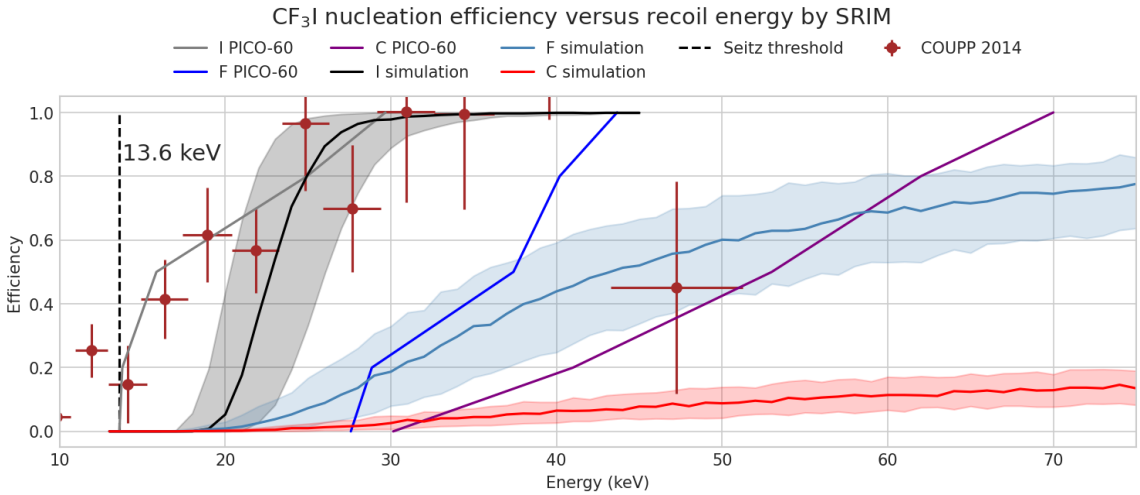

(a) Nucleation efficiency of CF_3I obtained through MD simulations, SRIM simulations, and Lindhard correction.

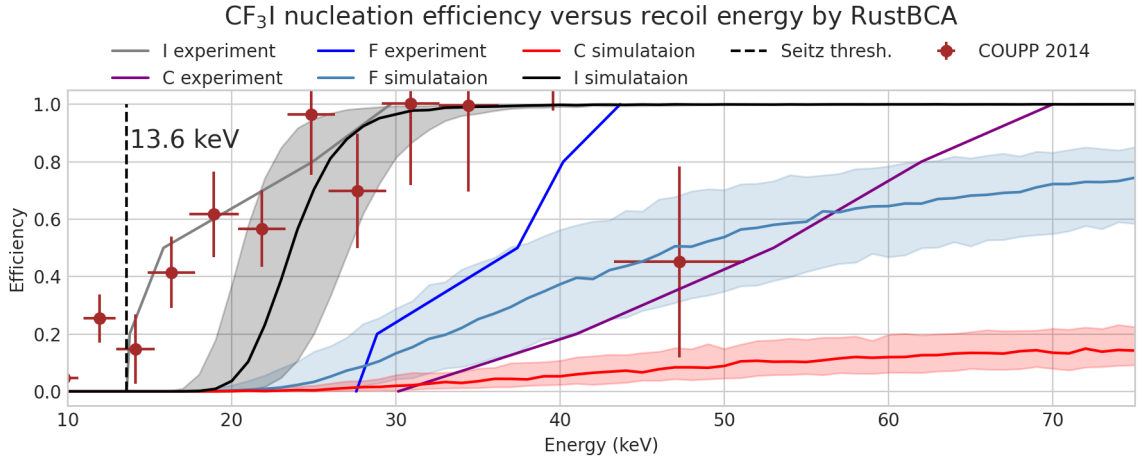

(b) Nucleation efficiency of CF_3I obtained through MD simulations, RustBCA simulations, and Lindhard correction.

Figure 6.5: The subplots in each graph illustrate the nucleation efficiency with a Seitz threshold of 13.6 keV indicated by the black vertical dashed line. The black solid curve represents the nucleation efficiency of iodine, the blue curve represents the nucleation efficiency of fluorine nuclei, and the red curve represents the nucleation efficiency of carbon, all obtained through calculations in this study. The gray, deep blue and purple curves represent the experimental results for iodide, fluorine, and carbon recoil, respectively, obtained through MCMC analysis. Additionally, the brown data point corresponds to the iodine nucleation efficiency as a function of iodine-equivalent recoil energy from the COUPP experiment [13].

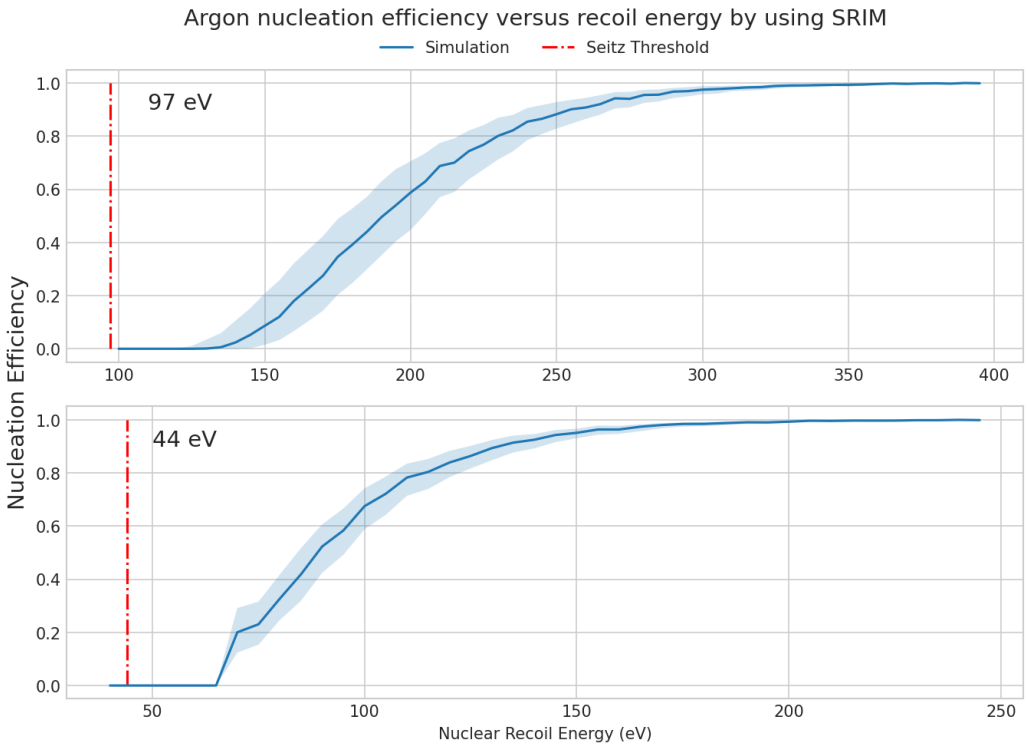

Figure 6.6: Predicted nucleation efficiency of liquid argon for the future SBC experiment, derived from MD simulations, SRIM simulations, and Lindhard correction.

6.1.4 Liquid Argon

In the upcoming SBC experiment [38], the plan is to utilize superheated liquid argon as the target. To prepare for this future operation, we conducted MD and MC simulations. These simulations aimed to predict the efficiency curve for the forthcoming experiment and understand our detector threshold. Additionally, we followed the same procedure to determine the nucleation efficiency for liquid argon at an energy threshold of 97 eV and 44 eV, as shown in Fig. 6.6. The corresponding thermodynamic parameters and properties for these threshold conditions are outlined in Table. 4.8.

SBC using liquid argon aim to operate at a low threshold to detect low-mass WIMPs and coherent neutrino scattering. Thus, the experiment sets the threshold in the range of tens to hundreds of eV. Fig. 6.6 illustrates the nucleation efficiency curve for different threshold conditions. For a threshold of 97 eV, the nucleation efficiency curve exhibits an increase after surpassing the Seitz threshold at approximately 130

$n_0 \setminus b$	0.0	0.5	1.0	1.5	2.0
0	0.00, 2.44	0.00, 1.94	0.00, 1.61	0.00, 1.33	0.00, 1.26
1	0.11, 4.36	0.00, 3.86	0.00, 3.36	0.00, 2.91	0.00, 2.53
2	0.53, 5.91	0.03, 5.41	0.00, 4.91	0.00, 4.41	0.00, 3.91
3	1.10, 7.42	0.60, 6.92	0.10, 6.42	0.00, 5.92	0.00, 5.42

Table 6.1: According to the Table.IV in Feldman and Cousins [83]. 90% C.L intervals for the Poisson signal μ, for total events observed n_0 for known mean background b. The number on the left is the lower limit, the right is the upper limit.

eV, reaching 100% efficiency slightly beyond 300 eV. On the other hand, the efficiency curve for the 44 eV threshold condition shows a rise starting at around 70 eV, with 100% efficiency achieved at 200 eV.

In the following stage, we eagerly anticipate conducting a thorough comparison of our current results with the forthcoming data, focusing particularly on the prototype chamber developed at the University of Alberta.

6.2 Effect on exclusion limit

The nucleation efficiency plays a crucial role in determining the exclusion limit of the bubble chamber, making it a significant factor to consider. Understanding the underlying principles that govern nucleation efficiency can provide valuable insights for planning future experiment operations. Recall Eq. 2.5 in Sect. 2.3.1

$$R_{obs} = \int_{E_{\min}}^{E_{\max}} \varepsilon\left(E_{nr}, m_{\chi}\right) \frac{dR}{dE_{nr}} dE_{nr} \tag{6.4}$$

where R_{obs} is the observed event rate, ε is the detector efficiency, E_{min} and E_{max} are the lower and upper energy limits of the region of interest. Therefore, we can determine expect events rate of the WIMPs for a given mass (m_{χ}). Most of the cases, when no WIMPs candidate events are found, 90% C.L. (confidence level) limits of the cross-section can be determined and the results above the limit will be excluded.

According to Feldman and Cousins [83], 90% confidence level (C.L.) intervals for

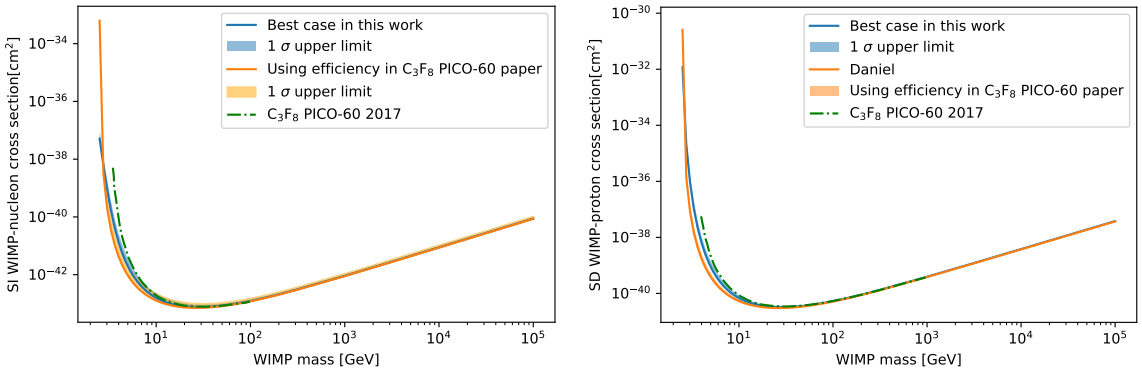

(a) SI WIMP-nucleus cross-section. (b) SD WIMP-proton cross-section.

Figure 6.7: The 90% C.L. limit on the cross-section in C_3F_8 PICO-60 2017 blind analysis. The blue line is calculated with the MD and MC generated efficiency, while the orange curve is derived from the MCMC efficiency function published PICO data [66]. The shaded region represents the 1-sigma efficiency upper limit area propagate to the cross-section. The green dashed line is the published cross-section in PICO-60 paper [84].

Poisson signal are presented in Table 6.1. If we have an experiment that detected 2 events with 1 expect background, 4.91 events and above can be excluded with 90% confidence. Therefore, we can use this principle to determine the exclusion limit σ_{lim} with a given mass m_χ.

$$\sigma_{\text{lim}}(m_\chi) = n_{\text{lim}} \frac{\sigma(m_\chi)}{R_{obs}(m_\chi) \cdot T_{\text{exposure}}} \tag{6.5}$$

where R_{obs} is the expected observed rate of the WIMPs for a given mass m_χ, and T_{exposure} is the exposure with the dimension of time multiplied by mass. n_{lim} is the 90% upper limit event in Table. 6.1 depending on the experimental event counts and prior expected background counts.

Fig. 6.7 and Fig. 6.8 present the exclusion limits for the PICO-60 C_3F_8 bubble chamber obtained using different approaches. The dashed lines are extracted directly from PICO-60 C_3F_8 blind analysis in 2017 [84] and the complete exposure in 2019 [35] as a benchmark. The event rate in the blue line is obtained with the MD and MC generated efficiency and integrated with the differential rate in Eq. 6.4. The uncertainty of the event rates is calculated by propagating the efficiency uncertainty.

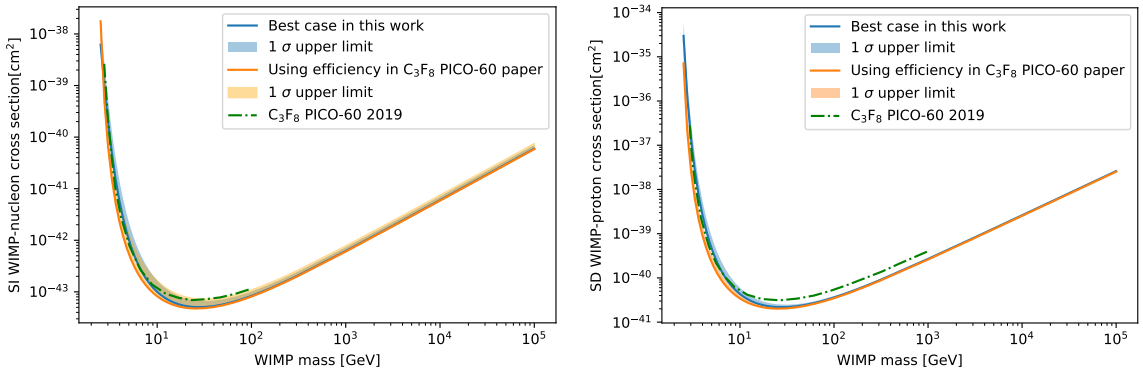

(a) SI WIMP-nucleus cross-section.

(b) SD WIMP-proton cross-section.

Figure 6.8: The 90% C.L. limit on the cross-section in C_3F_8 PICO-60 2019 complete exposure. The blue curve is calculated with the MD and MC generated efficiency, while the orange curve is derived from the MCMC efficiency function published PICO data [66]. The shaded region represents the 1-sigma efficiency upper limit area propagate to the cross-section. The green dashed line is the published cross-section in PICO-60 paper [35].

The lines with label "best case" represents the result obtained using the best-fit efficiency function, while the lines labeled "1-sigma upper limit" shows the 1-sigma uncertainty of the efficiency propagated to the cross-section limit. The cross-section and differential rate dR/dE_{nr} function are extracted from the `dmdd` package [85]. We use the standard WIMPs halo parameters [86], which are the same as those in the PICO-60 publications. The parameters are: Local dark matter density $\rho_D = 0.3$ GeV/c^{-2}cm^{-3}, galactic escape velocity $v_{esc} = 544$ km/s, velocity of the earth with respect to the halo $v_{Earth} = 232$ km/s, and characteristic WIMP velocity with respect to the halo $v_0 = 220$ km/s. In the PICO-60 in 2017 blind exposure [84], the detector was operated with a 3.3 keV Seitz threshold in the first run, with 0.25 prior expected background, there were no recorded single bubble events during the 1167 kg-day first run exposure. As a result, the 90% upper limit was calculated to be 2.44 events. In the PICO-60 in 2019 complete exposure [35], the detector's Seitz threshold was set to 2.4 keV in second run. During the 1404 kg-day exposure second run period, 3 single bubble events have been observed with an expected 1 background event. Consequently, the 90% upper limit was estimated to be 6.42 events. The complete

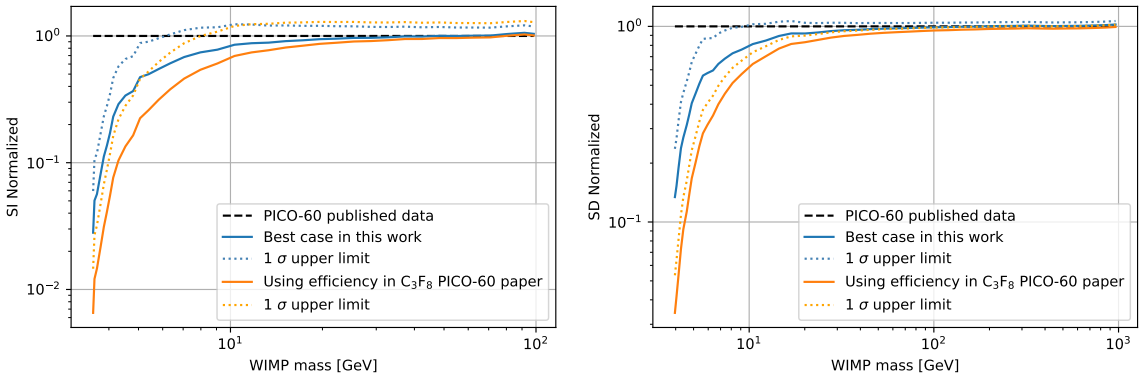

(a) SI WIMP-nucleus cross-section normalized with respect to PICO-60 published results.

(b) SD WIMP-proton cross-section normalized with respect to PICO-60 published results.

Figure 6.9: Reproduced exclusion limit normalized with respect to the PICO-60 C_3F_8 2017 blind analysis publication [84]. The blue line is calculated with the MD and MC generated efficiency, and the orange line is calculated with the efficiency in PICO MCMC analysis [66]. The dotted lines represents the conservative 1-sigma upper limit considering the uncertainty from each efficiency curve.

exposure final result includes both the first and second runs. They are combined via:

$$\frac{1}{\sigma_{tot}^{\text{lim}}} = \sum_i \frac{1}{\sigma_i^{\text{lim}}} \tag{6.6}$$

where σ_{tot} is the total excluded cross-section limit and i represents each run. The same applies to the combined cross-section limit for different elements in the target [86].

When comparing results, it is important to note that the 2017 blind analysis results represent a conservative limit. They use an efficiency function that is rescaled upwards to account for the 2% difference in thermodynamic threshold. In the complete exposure in 2019, it shows the best fit exclusion limit. The estimated exclusion limit curves in our study are found to be consistent with the results obtained from the PICO-60 profile likelihood analysis. These curves, represented by the blue and orange lines, primarily differ in their utilization of different efficiency functions. Specifically, the blue curve employs the best fit efficiency derived from our work, as shown in Fig.6.4a, while the orange curve adopts the efficiency obtained through MCMC analysis, as depicted in Fig.6.4a for PICO-60. Despite these distinctions, the exclusion limit curves

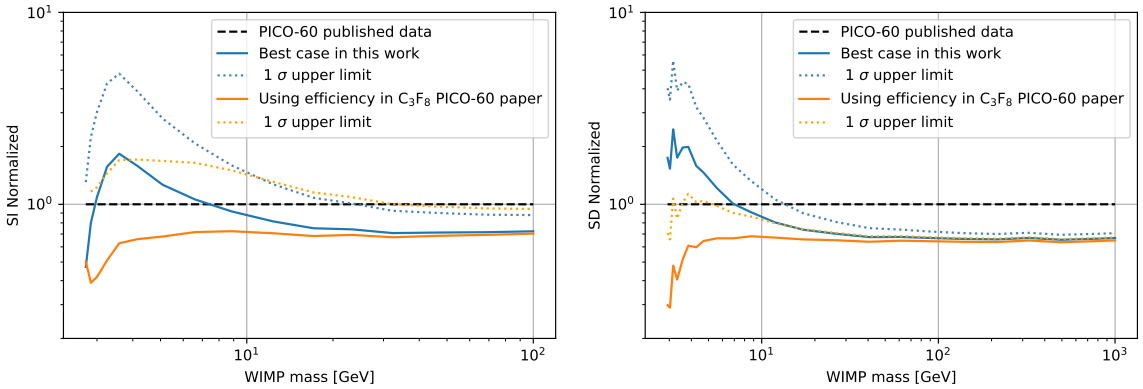

(a) SI WIMP-nucleus cross-section normalized with respect to PICO-60 published results.

(b) SD WIMP-proton cross-section normalized with respect to PICO-60 published results.

Figure 6.10: Reproduced exclusion limit normalized with respect to the PICO-60 C_3F_8 2019 complete exposure publication [35]. The blue curve is calculated with the MD and MC generated efficiency, and the orange curve is calculated with the efficiency in PICO MCMC analysis. The dotted curves represents the conservative 1-sigma upper limit considering the uncertainty from each efficiency curve.

generally align with each other. Fig. 6.9 and Fig. 6.10 show that two reproduced curves are normalized with respect to the PICO published results. Both blind analysis result and the complete exposure result show that the reproduced curves and the PICO published results are within the same order of magnitude. In the high WIMP mass range, the exclusion limit curves are mostly aligned. This is because a higher WIMP mass corresponds to a higher recoil energy, and the nucleation efficiency is always one for high energy. However, discrepancies begin to emerge around the curves' minima and in the lower mass range, primarily due to the variation in efficiency. In the 2017 blind analysis, the maximum difference is approximately between 1 and 2 order of magnitude lower than the published findings in low mass range. Conversely, in the full exposure analysis, the maximum difference can range from within an order of magnitude with respect to the published results. These difference between each limit we obtained from the efficiency and the PICO publish results are primarily attributable to numerical errors arising from the use of different analysis methods. Fluctuation within an order of magnitude is common to all rare-event search experi-

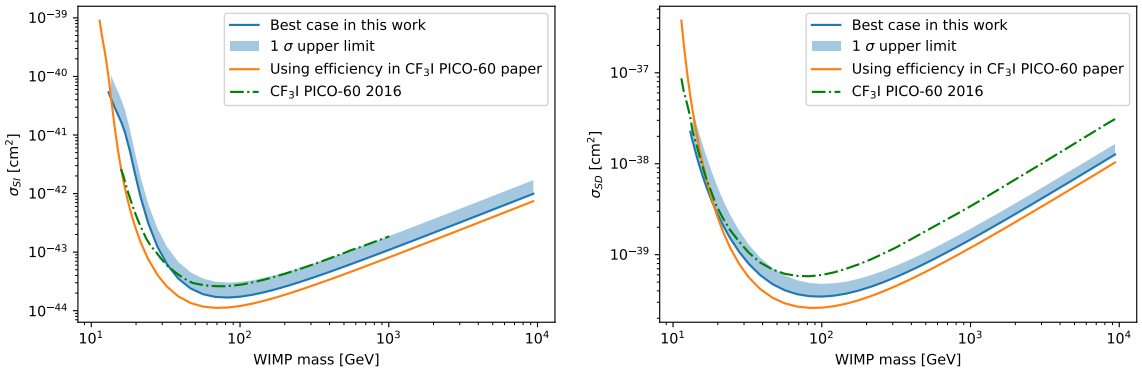

(a) SI WIMP-nucleus cross-section.

(b) SD WIMP-proton cross-section.

Figure 6.11: The 90% C.L. limit on the cross-section in CF_3I bubble chamber. The blue curve is calculated with the MD and MC generated efficiency, the orange curve is calculated with CF_3I PICO-60 published efficiency function [64]. The shaded region represents the 1-sigma efficiency upper limit propagate to the cross-section. The green dashed line is the cross-section limit reported in the PICO publication [64].

ments [37]. To understand the impact of efficiency, we need to compare the difference between reproduced results where the only variable is the efficiency function. These differences in efficiency functions mainly affect the exclusion curves in the low mass range. The discrepancy between using different efficiency function is within an order of magnitude. In the context of SI analysis, the observed small discrepancy can be attributed to the fact that both the simulated carbon and fluorine efficiencies lie between the efficiencies obtained from the MCMC analysis. This intermediate positioning mitigate some of the discrepancies between the two. On the other hand, in the SD analysis, where only the fluorine nucleus contributes to the SD mitigate cross-section, the exclusion limit produced by the simulated efficiency appears to be more conservative. This is due to the simulated efficiency being slightly lower than the efficiency derived from the MCMC analysis.

For CF_3I, the cross-section exclusion limit curves estimated in our study are consistent with the results obtained from the PICO-60 analysis [64]. Note that the published results shown are conservative, as the 1-sigma upper limit of the efficiency function was used to obtain the result. Fig. 6.11 shows the 90% confidence level upper limit

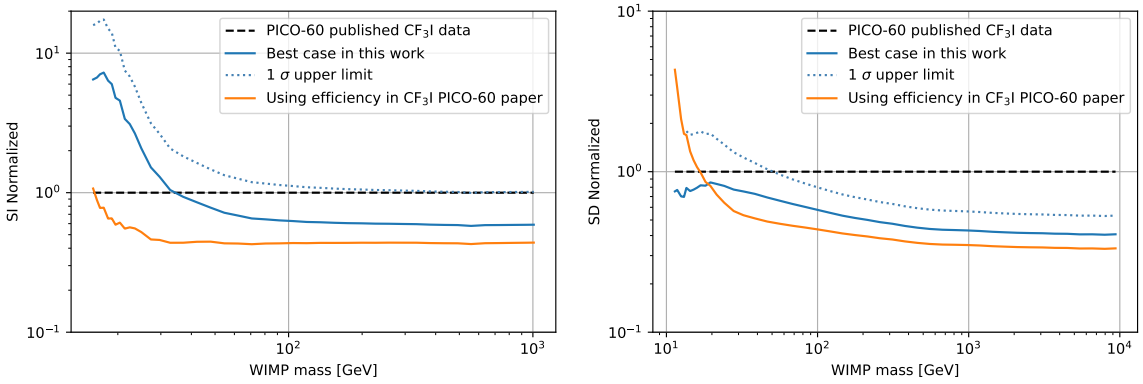

(a) SI WIMP-nucleus cross-section normalized with respect to PICO-60 published CF_3I results.

(b) SD WIMP-proton cross-section normalized with respect to PICO-60 published CF_3I results.

Figure 6.12: Comparison of exclusion limits normalized to PICO-60 CF_3I Data. The blue curve is calculated with the MD and MC generated efficiency, while the orange curve is derived from the efficiency function published PICO data[64]. Dotted curve indicates the conservative 1-sigma upper limits, accounting for uncertainties in the efficiency curve.

cross-section exclusion. It is also normalized with respect to the PICO-60 published data, as shown in Fig. 6.12a. The "best case" represents the result obtained using the best-fit efficiency function, while the "1-sigma upper limit" shows the 1-sigma uncertainty of the efficiency propagated to the cross-section limit. The results for two recalculated exclusion limit are consistence within an order of magnitude. In the SI cross-section shown in Fig. 6.11a and Fig. 6.12a, there is a relatively high discrepancy between the results in this work and in PICO-60 for the low WIMP mass range. This is mainly due to the carbon nucleation efficiency, which contributes mostly to the low mass range and is lower in the simulated results compared to the experimental results. The impact of carbon makes the difference up to 6 times higher the published results in SI cross-section. On the other hand, for the SD cross-section in Fig. 6.11b and Fig. 6.12b, the results are mostly consistent with the experimental results within the same order of magnitude, due to only fluorine and iodine contributing to the SD cross-section. One thing to note is that the uncertainty in efficiency, as produced in this work (blue curve), has been taken into account and shown as shaded area when

calculating the exclusion limit. As the efficiency from the PICO-60 CF_3I publication is not provided, the reproduced result (orange curve) does not include the uncertainty.

Using our new model with MD and MC simulations shows promise in assessing bubble nucleation efficiency and estimating cross-section limits with an accuracy within the same order of magnitude. This could potentially obviate the need for experimental calibration. This methodological approach provides valuable insights into understanding the intrinsic constraints of detectors. It also advances our understanding of their operational limitations and assists with experimental operation planning.

6.3 Discussion

In Section 5.3, we present the Lindhard model as a means to describe the fraction of energy loss in electronic stopping that contributes to ionization and excitation. In our study, we employ the Lindhard model to estimate the energy loss of secondary ions generated by the initial recoiling ion. In this section, we will thoroughly discuss and compare the results obtained with and without the incorporation of this correction.

Fig. 6.13 presents the nucleation efficiency of xenon. The blue and green curves correspond to the same data shown in Fig. 6.2. The purple dotted curve represents the results without the Lindhard factor correction. The observed outcome is aligned with expectations, as the Lindhard factor correction for secondary ions leads to an additional energy loss in electronic stopping, resulting in a greater contribution to the heat spike and hence better efficiency. However, even with the correction, there are still deviations from the experimental results. Several hypotheses merit exploration. Firstly, noble liquid gases exhibit scintillation properties due to the ionization and excitation processes involved. These processes entail the intricate formation of dimers [87]. One of the phenomena entails the excitation of noble liquid atoms through electron collisions, resulting in the formation of highly stable diatomic molecules in an excited state known as excimers. The excimers will produce photons during the de-excitation. The process can be shown as:

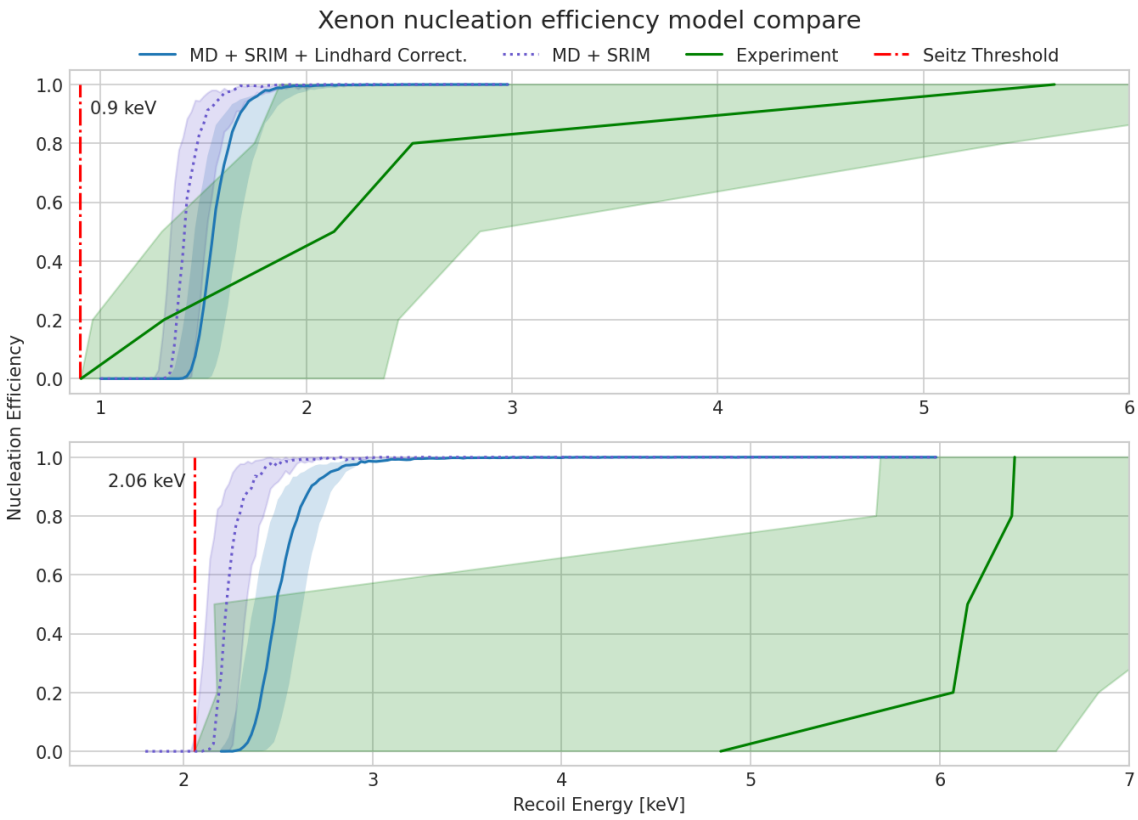

Figure 6.13: Lindhard model correction impact on the nucleation efficiency for xenon.

$$
\begin{aligned}
&e^- + R \rightarrow R^* + e^- && \text{impact excitation} \\
&R^* + R \rightarrow R_2^{*,v} && \text{excimer formation} \\
&R_2^{*,v} + R \rightarrow R_2^* + R && \text{relaxation} \\
&R_2^* \rightarrow R + R + h\nu && \text{VUV emission}
\end{aligned}
$$

where, R = Ar or Xe and the superscript v is used to distinguish excited states with vibrational excitation within the molecule bond.

On the other hands, for the case of ionization, the ions and free electrons would recombine and form excimers. De-excited of the excimers will produce photons. The process can be shown as:

$$
\begin{aligned}
&e^- + R \rightarrow R^+ + 2e^- && \text{ionization} \\
&R^+ + R + R \rightarrow R_2^+ + R && \\
&e^- + R_2^+ \rightarrow R^{**} + R && \text{recombination} \\
&R^{**} + R \rightarrow R^* + R + \text{ heat} && \\
&R^* + R + R \rightarrow R_2^* + R + \text{ heat} && \\
&R_2^* \rightarrow R + R + h\nu && \text{VUV emission}
\end{aligned}
$$

The recombination occurs mostly with molecular ions formed shortly (∼ps) after ionization. However, both ionization and excitation processes involve two different kinds of excimers, called singlet and triplet state. The de-excitation time for a triplet state is longer than that of the singlet state due to the forbidden direct transition from the triplet state to the ground state. The lifetime for the triplet state in LXe is approximately $\sim 27 - 34$ ns, while the singlet state has a lifetime of 2.2 ns [87]. In the aforementioned process, we observed that it involved an inelastic collision that would result in a loss of kinetic energy from the $R^* + R \rightarrow R_2^{*,v}$ excimer formation. In the process after the ionization, heat is generated after recombination as well. The hypothesis is that some of the heat release will be delayed due to the long lifetime of the triplet state. The time scale of bubble formation is in the order of ∼ns, and the bubble may collapse within ∼3 ns as we can see from the MD simulation Fig. 4.4.

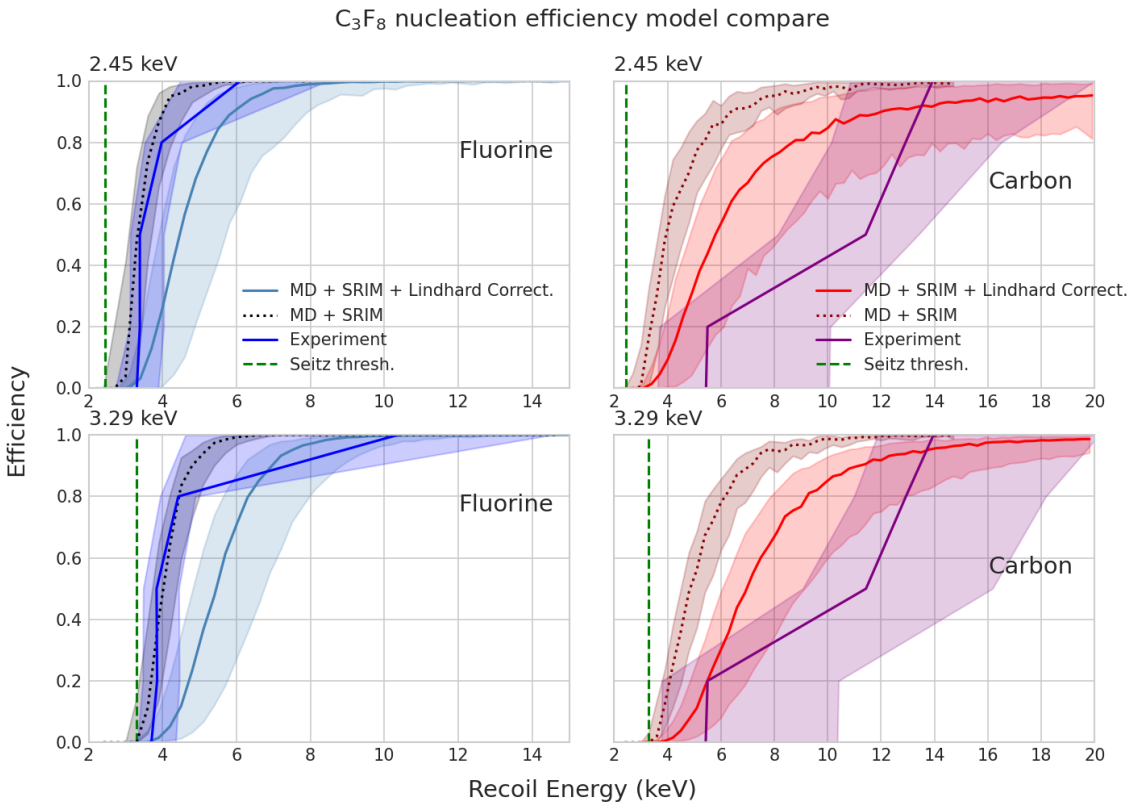

Figure 6.14: Lindhard model correction impact on the nucleation efficiency for C_3F_8.

Estimating the amount of delayed heat release is a challenge, and it could be the next step of this project.

Moving on to the results for C_3F_8, as depicted in Fig. 6.14, we observe that the nucleation efficiency without employing the Lindhard correction is represented by the dotted curve. Notably, the fluorine efficiency without the correction falls within the 1-sigma error band of the experimental data, indicating a strong agreement. In contrast, the efficiency for carbon with the Lindhard correction aligns more closely with the experimental analysis. There are two primary factors to consider. Firstly, the Lindhard model demonstrates better performance with noble liquid, benefiting from the numerous experimental data available. However, for C_3F_8, the Lindhard factor is solely calculated based on theoretical grounds, lacking experimental verification. Secondly, the MD simulation employs a simplified coarse-graining (CG) model, treating C_3F_8 as a sphere, while the MC simulation does not account for molecular structure.

Assuming the validity of the Lindhard correction, the discrepancy may stem from the influence of the molecule's structure. Similar considerations apply to CF_3I, as shown in Fig. 6.15, where the complexity of the molecule and the uncertainty associated with the Lindhard correction introduce further challenges. The endeavor to construct a full molecular simulation incorporating chemical bonds has been contemplated. However, it is important to note that a fully detailed molecular simulation without CG is computationally demanding and would not yield results within a reasonable time frame. Overall, the efficiency results for the primary targets, fluorine in C_3F_8 and iodine in CF_3I, are reasonably accurate even without incorporating experimental data. The impact of this discrepancy is minimal since carbon in C_3F_8 does not couple with the spin-dependent WIMP. Furthermore, in terms of the spin-independent cross-section, carbon's contribution is almost negligible compared to fluorine and iodine in both targets.

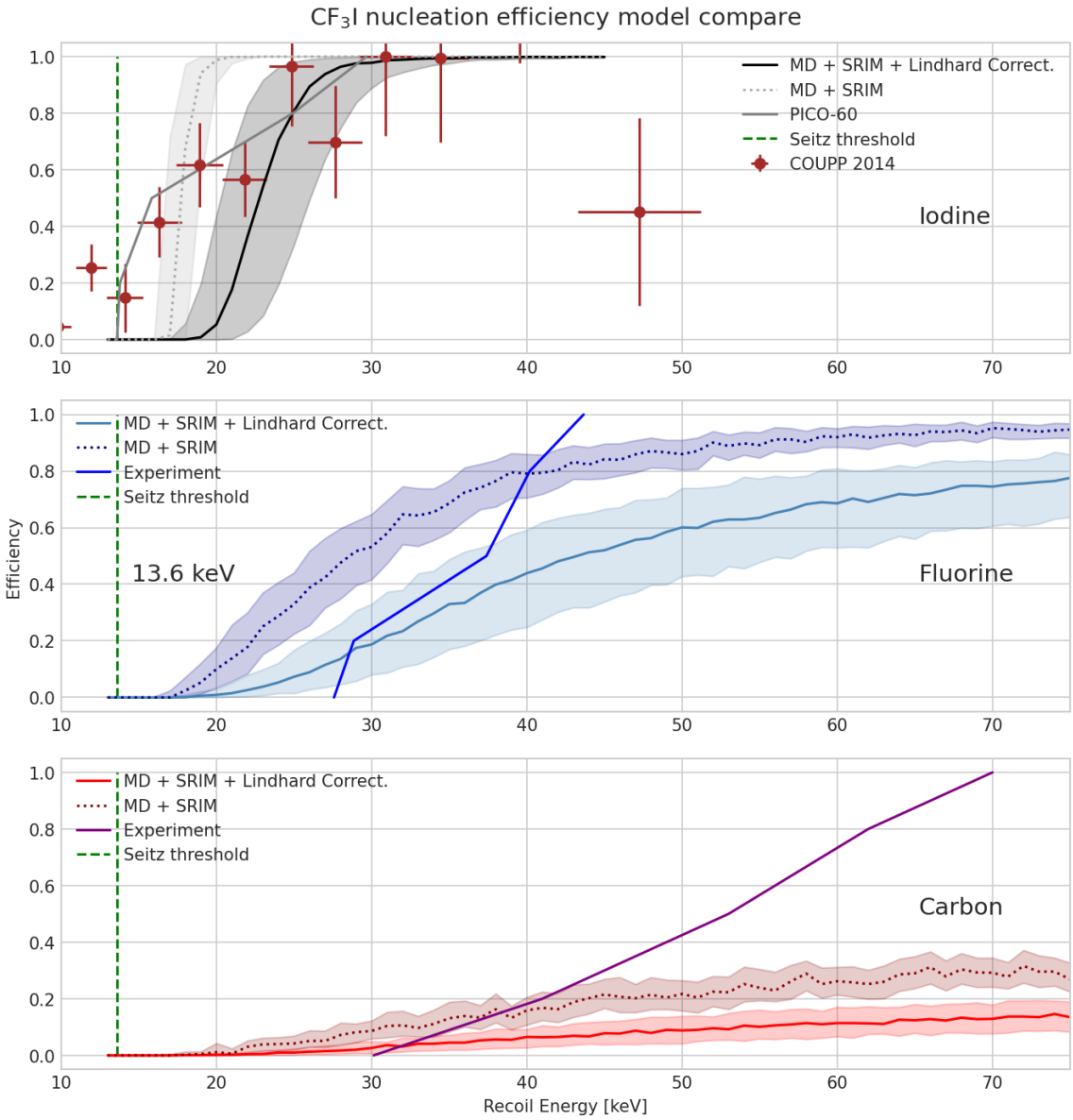

Figure 6.15: Lindhard model correction impact on the nucleation efficiency for CF_3I.

Chapter 7

Summary and the Future Work

Despite the absence of definitive evidence of dark matter through ongoing experiments, the present moment holds great promise for direct dark matter detection. This optimism stems from the fact that the initial tonne-scale experiments are currently gathering data, with several others progressing toward the construction or planning stages. These upcoming detectors possess the capability poised to breach the neutrino floor [38], a significant milestone in the field. The thesis work provides insights into the bubble nucleation efficiency for bubble chamber dark matter detectors. Such insights have the potential to assist in detector design and planning future operations.

This thesis work begins by exploring the operational principle of bubble chambers, which are operated with a metastable state known as a superheated state. In these detectors, when the WIMP or neutron interacts with the target nucleus, the recoiling nucleus traverses through the target medium, resulting in energy deposition as a local heat spike. Such a heat spike triggers the superheated liquid to have a local phase change, resulting in a bubble. The energy deposition is described by the Seitz model, which depends on the pressure and temperature of the superheated liquid. Although the Seitz model, has conventionally been considered as the threshold for bubble chamber detection, experimental results have indicated that the efficiency of bubble nucleation is influenced by the energy of the nuclear recoil. Consequently, this

thesis focuses on studying the factors that impact bubble formation to gain a deeper understanding of the phenomenon.

The study begins by using molecular dynamics simulations to investigate the formation of bubbles at the microscopic scale. The simulations involve depositing energy in a cylinder to simulate the track length. Depending on the energy and length of the cylinder, the bubbles will either grow or collapse. An empirical function (linear energy density as a function of cylinder length) is used to fit the events between bubble formation and collapse. The resulting empirical function is used as an acceptance or rejection criterion to determine the bubble nucleation efficiency in the Monte Carlo simulation.

In addition, Monte Carlo simulations are employed to investigate the transfer of energy from recoiling nuclei to the target material. The energy loss during this process can be divided into nuclear stopping and electronic stopping. However, only the energy attributed to nuclear stopping contributes to the heat necessary for bubble formation. The Lindhard model, a theoretical model, is used to describe the energy transfer and approximate the energy loss of secondary ions. Additionally, the Lindhard model is used as a benchmark to validate the results obtained from the Monte Carlo simulations.

By combining molecular dynamics and Monte Carlo simulations, it is possible to determine the efficiency of bubble nucleation. The criterion for successful bubble formation is satisfied when the linear energy density exceeds the threshold defined by the empirical function. Conversely, if the condition is not met, the bubble will collapse. Simulations conducted across various nuclear recoil energies can determine the relationship between bubble nucleation efficiency and nuclear recoil. The results obtained show promising agreement with experimental data.

Combining MD and MC simulations can generate efficiency, which allows us to replicate the cross-section exclusion limit. The results enable comparisons with experimental observations, facilitating a comprehensive assessment of how the simulated

outcomes impact the exclusion limit. This methodology not only offers insights for the planning of future experimental procedures but also has the potential to obviate the requirement for experimental calibration.

Moving forward, several aspects need to be explored to continue this project. The Lindhard factor calculation is still active in the sub-keV range. This factor can also be computed from the nucleation efficiency obtained experimentally. One area of focus is delving deeper into the energy transfer mechanisms, including the energy associated with dimmer formation in noble liquids. Another aspect is developing theoretical models that describe the formation of bubbles based on energy and track length. Furthermore, an intriguing development in the project is the ongoing construction of a prototype scintillation bubble chamber in the Piro Lab at the University of Alberta. This presents an exciting opportunity to compare and validate the existing models with experimental observations, further enhancing our understanding of bubble formation, and potentially adding the directional channel into the bubble chamber.

Bibliography

[1] F. Zwicky, "On the masses of nebulae and of clusters of nebulae," *The Astrophysical Journal*, vol. 86, p. 217, 1937. DOI: 10.1086/143864.

[2] G. Bertone, D. Hooper, and J. Silk, "Particle dark matter: Evidence, candidates and constraints," *Physics Reports*, vol. 405, no. 5-6, pp. 279–390, Jan. 2005. DOI: 10.1016/j.physrep.2004.08.031.

[3] M. Schumann, "Direct detection of WIMP dark matter: Concepts and status," *Journal of Physics G: Nuclear and Particle Physics*, vol. 46, no. 10, p. 103 003, Aug. 2019. DOI: 10.1088/1361-6471/ab2ea5.

[4] K. G. Begeman, A. H. Broeils, and R. H. Sanders, "Extended rotation curves of spiral galaxies: Dark haloes and modified dynamics," *Monthly Notices of the Royal Astronomical Society*, vol. 249, no. 3, pp. 523–537, 1991. DOI: 10.1093/mnras/249.3.523.

[5] K. Freese, *Dark matter in galaxies and clusters*, 2017.

[6] J. Kormendy and K. C. Freeman, "Scaling Laws for Dark Matter Halos in Late-Type and Dwarf Spheroidal Galaxies," in *Dark Matter in Galaxies*, S. Ryder, D. Pisano, M. Walker, and K. Freeman, Eds., vol. 220, Jul. 2004, p. 377. DOI: 10.48550/arXiv.astro-ph/0407321. arXiv: astro-ph/0407321 [astro-ph].

[7] J. A. Tyson, F. Valdes, and R. A. Wenk, "Detection of Systematic Gravitational Lens Galaxy Image Alignments: Mapping Dark Matter in Galaxy Clusters," *apjl*, vol. 349, p. L1, Jan. 1990. DOI: 10.1086/185636.

[8] D. Clowe *et al.*, "A Direct Empirical Proof of the Existence of Dark Matter," *apjl*, vol. 648, no. 2, pp. L109–L113, Sep. 2006. DOI: 10.1086/508162. arXiv: astro-ph/0608407 [astro-ph].

[9] H. Hoekstra, M. Bartelmann, H. Dahle, H. Israel, M. Limousin, and M. Meneghetti, "Masses of galaxy clusters from gravitational lensing," *Space Science Reviews*, vol. 177, no. 1-4, pp. 75–118, Apr. 2013. DOI: 10.1007/s11214-013-9978-5.

[10] R. Garner, *Nasa's webb delivers deepest infrared image of universe yet*, Jul. 2022. [Online]. Available: https://www.nasa.gov/image-feature/goddard/2022/nasa-s-webb-delivers-deepest-infrared-image-of-universe-yet.

[11] M. D. Schneider, Ó. Holm, and L. Knox, "INTELLIGENT DESIGN: ON THE EMULATION OF COSMOLOGICAL SIMULATIONS," *The Astrophysical Journal*, vol. 728, no. 2, p. 137, Jan. 2011. DOI: 10.1088/0004-637x/728/2/137.

[12] A. B. Newman, T. Treu, R. S. Ellis, and D. J. Sand, "The Density Profiles of Massive, Relaxed Galaxy Clusters. II. Separating Luminous and Dark Matter in Cluster Cores," *apj*, vol. 765, no. 1, 25, p. 25, Mar. 2013. DOI: 10.1088/0004-637X/765/1/25. arXiv: 1209.1392 [astro-ph.CO].

[13] C. L. Bennett *et al.*, "Nine-year Wilkinson Microwave Anisotropy Probe (WMAP) Observations: Final Maps and Results," *apjs*, vol. 208, no. 2, 20, p. 20, Oct. 2013. DOI: 10.1088/0067-0049/208/2/20. arXiv: 1212.5225 [astro-ph.CO].

[14] Planck Collaboration *et al.*, "Planck 2018 results. VI. Cosmological parameters," *app*, vol. 641, A6, A6, Sep. 2020. DOI: 10.1051/0004-6361/201833910. arXiv: 1807.06209 [astro-ph.CO].

[15] K. Garrett and G. Duda, "Dark matter: A primer," *Advances in Astronomy*, vol. 2011, pp. 1–22, 2011. DOI: 10.1155/2011/968283.

[16] N. Jarosik *et al.*, "Seven-year wilkinson microwave anisotropy probe (wmap) observations: Sky maps, systematic errors, and basic results," *The Astrophysical Journal Supplement Series*, vol. 192, no. 2, p. 14, Jan. 2011. DOI: 10.1088/0067-0049/192/2/14.

[17] J. Billard *et al.*, "Direct detection of dark matter—APPEC committee report," *Reports on Progress in Physics*, vol. 85, no. 5, p. 056 201, Apr. 2022. DOI: 10.1088/1361-6633/ac5754.

[18] R. D. Peccei and H. R. Quinn, "CP conservation in the presence of pseudoparticles," *prl*, vol. 38, no. 25, pp. 1440–1443, Jun. 1977. DOI: 10.1103/PhysRevLett.38.1440.

[19] D. J. E. Marsh, "Axion cosmology," *physrep*, vol. 643, pp. 1–79, Jul. 2016. DOI: 10.1016/j.physrep.2016.06.005. arXiv: 1510.07633 [astro-ph.CO].

[20] I. G. Irastorza and J. Redondo, "New experimental approaches in the search for axion-like particles," *Progress in Particle and Nuclear Physics*, vol. 102, pp. 89–159, Sep. 2018. DOI: 10.1016/j.ppnp.2018.05.003.

[21] M. W. Goodman and E. Witten, "Detectability of certain dark-matter candidates," *Phys. Rev. D*, vol. 31, pp. 3059–3063, 12 Jun. 1985. DOI: 10.1103/PhysRevD.31.3059.

[22] G. Jungman, M. Kamionkowski, and K. Griest, "Supersymmetric dark matter," *Physics Reports*, vol. 267, no. 5-6, pp. 195–373, 1996. DOI: 10.1016/0370-1573(95)00058-5.

[23] G. Bertone, D. Hooper, and J. Silk, "Particle dark matter: Evidence, candidates and constraints," *Physics Reports*, vol. 405, no. 5-6, pp. 279–390, 2005. DOI: 10.1016/j.physrep.2004.08.031.

[24] X. Bi, *Detection of dark matter particles and progress**, Aug. 2018.

[25] G. Aad *et al.*, "Search for dark matter in events with missing transverse momentum and a higgs boson decaying to two photons in pp collisions at $\sqrt{s} = 8$ TeV with the atlas detector," *Phys. Rev. Lett.*, vol. 115, p. 131 801, 13 Sep. 2015. DOI: 10.1103/PhysRevLett.115.131801.

[26] M. Aaboud *et al.*, "Search for an invisibly decaying higgs boson or dark matter candidates produced in association with a z boson in pp collisions at $\sqrt{s} = 13$ tev with the ATLAS detector," *Physics Letters B*, vol. 776, pp. 318–337, Jan. 2018. DOI: 10.1016/j.physletb.2017.11.049.

[27] R. W. Schnee, "Introduction to dark matter experiments," in *Theoretical Advanced Study Institute in Elementary Particle Physics: Physics of the Large and the Small*, 2011, pp. 775–829. DOI: 10.1142/9789814327183_0014. arXiv: 1101.5205 [astro-ph.CO].

[28] T. M. Undagoitia and L. Rauch, "Dark matter direct-detection experiments," *Journal of Physics G: Nuclear and Particle Physics*, vol. 43, no. 1, p. 013 001, Dec. 2015. DOI: 10.1088/0954-3899/43/1/013001.

[29] R. Bernabei *et al.*, "First results from DAMA/LIBRA and the combined results with DAMA/NaI," *Eur. Phys. J. C*, vol. 56, pp. 333–355, 2008. DOI: 10.1140/epjc/s10052-008-0662-y. arXiv: 0804.2741 [astro-ph].

[30] M. Kuź niak, "Status of the DEAP-3600 experiment," *Journal of Physics: Conference Series*, vol. 2156, no. 1, p. 012 070, Dec. 2021. DOI: 10.1088/1742-6596/2156/1/012070.

[31] Y. Ko *et al.*, "Comparison between DAMA/LIBRA and COSINE-100 in the light of quenching factors," *Journal of Cosmology and Astroparticle Physics*, vol. 2019, no. 11, pp. 008–008, Nov. 2019. DOI: 10.1088/1475-7516/2019/11/008.

[32] I. Arnquist *et al.*, *The damic-m experiment: Status and first results*, 2022. arXiv: 2210.12070 [hep-ex].

[33] L. Barak *et al.*, "SENSEI: Direct-detection results on sub-GeV dark matter from a new skipper CCD," *Physical Review Letters*, vol. 125, no. 17, Oct. 2020. DOI: 10.1103/physrevlett.125.171802.

[34] L. Balogh *et al.*, "The NEWS-g detector at SNOLAB," *Journal of Instrumentation*, vol. 18, no. 02, T02005, Feb. 2023. DOI: 10.1088/1748-0221/18/02/t02005.

[35] C. Amole *et al.*, "Dark matter search results from the complete exposure of the PICO-60 c_3f_8 bubble chamber," *Physical Review D*, vol. 100, no. 2, Jul. 2019. DOI: 10.1103/physrevd.100.022001.

[36] O. Kamaev, *Results from the cryogenic dark matter search experiment*, 2009. arXiv: 0910.3005 [hep-ex].

[37] E. Aprile *et al.*, "The XENON1T Dark Matter Experiment," *Eur. Phys. J. C*, vol. 77, no. 12, p. 881, 2017. DOI: 10.1140/epjc/s10052-017-5326-3. arXiv: 1708.07051 [astro-ph.IM].

[38] E. Alfonso-Pita *et al.*, "Snowmass 2021 Scintillating Bubble Chambers: Liquid-noble Bubble Chambers for Dark Matter and CEνNS Detection," in *Snowmass 2021*, Jul. 2022. arXiv: 2207.12400 [physics.ins-det].

[39] C. B. Krauss and for the PICO Collaboration, "Pico-60 results and pico-40l status," *Journal of Physics: Conference Series*, vol. 1468, no. 1, p. 012 043, Feb. 2020. DOI: 10.1088/1742-6596/1468/1/012043.

[40] D. Akerib *et al.*, "The LUX-ZEPLIN (LZ) experiment," *Nuclear Instruments and Methods in Physics Research Section A: Accelerators, Spectrometers, Detectors and Associated Equipment*, vol. 953, p. 163 047, Feb. 2020. DOI: 10.1016/j.nima.2019.163047.

[41] Q. Wang *et al.*, "Results of dark matter search using the full PandaX-II exposure," *Chinese Physics C*, vol. 44, no. 12, p. 125 001, Dec. 2020. DOI: 10.1088/1674-1137/abb658.

[42] E. Behnke *et al.*, "Final results of the PICASSO dark matter search experiment," *Astroparticle Physics*, vol. 90, pp. 85–92, Apr. 2017. DOI: 10.1016/j.astropartphys.2017.02.005.

[43] M. G. Aartsen *et al.*, "Search for annihilating dark matter in the sun with 3 years of IceCube data," *The European Physical Journal C*, vol. 77, no. 3, Mar. 2017. DOI: 10.1140/epjc/s10052-017-4689-9.

[44] K. Choi *et al.*, "Search for neutrinos from annihilation of captured low-mass dark matter particles in the sun by super-kamiokande," *Phys. Rev. Lett.*, vol. 114, p. 141 301, 14 Apr. 2015. DOI: 10.1103/PhysRevLett.114.141301.

[45] C. A. J. O'Hare, "New definition of the neutrino floor for direct dark matter searches," *Physical Review Letters*, vol. 127, no. 25, Dec. 2021. DOI: 10.1103/physrevlett.127.251802.

[46] D. A. Glaser, "Some effects of ionizing radiation on the formation of bubbles in liquids," *Phys. Rev.*, vol. 87, pp. 665–665, 4 Aug. 1952. DOI: 10.1103/PhysRev.87.665.

[47] R. P. Shutt and D. Keefe, "Bubble and Spark Chambers: Principles and Uses, Vol. 1 and 2," *Physics Today*, vol. 22, no. 4, pp. 95–97, Apr. 1969, ISSN: 0031-9228. DOI: 10.1063/1.3035548.

[48] F. Hasert *et al.*, "Observation of neutrino-like interactions without muon or electron in the gargamelle neutrino experiment," *Physics Letters B*, vol. 46, no. 1, pp. 138–140, 1973. DOI: 10.1016/0370-2693(73)90499-1.

[49] G. Arnison *et al.*, "Experimental observation of isolated large transverse energy electrons with associated missing energy at," *Physics Letters B*, vol. 122, no. 1, pp. 103–116, 1983. DOI: 10.1016/0370-2693(83)91177-2.

[50] W. B. Fowler and N. P. Samios, "The omega-minus experiment," *Scientific American*, vol. 211, no. 4, pp. 36–45, 1964, ISSN: 00368733, 19467087. (visited on 06/11/2023).

[51] M. B. H. Mantelli, "Physical principles," in *Thermosyphons and Heat Pipes: Theory and Applications*. Cham: Springer International Publishing, 2021, pp. 9–46, ISBN: 978-3-030-62773-7. DOI: 10.1007/978-3-030-62773-7_2.

[52] A. Plante, "Searching for dark matter with superheated liquid detectors," Ph.D. dissertation.

[53] F. Seitz, "On the theory of the bubble chamber," *Physics of Fluids*, vol. 1, no. 1, p. 2, 1958. DOI: 10.1063/1.1724333.

[54] I. A. Pless and R. J. Plano, "Negative pressure isopentane bubble chamber," *Review of Scientific Instruments*, vol. 27, no. 11, pp. 935–937, 1956. DOI: 10.1063/1.1715416.

[55] M. J. Harper, "Calculation of recoil ion effective track lengths in neutron-radiation-induced nucleation," *Nuclear Science and Engineering*, vol. 114, no. 2, pp. 118–123, 1993. DOI: 10.13182/NSE93-A24023. eprint: https://doi.org/10.13182/NSE93-A24023.

[56] P. Denzel, J. Diemand, and R. Angélil, "Molecular dynamics simulations of bubble nucleation in dark matter detectors," *Physical Review E*, vol. 93, no. 1, 2016. DOI: 10.1103/physreve.93.013301.

[57] T. Frederic and V. Zacek, "Direct detection of dark matter with the pico experiment and the pico-0.1 calibration chamber," Ph.D. dissertation.

[58] Y.-Q. Xue, X.-C. Yang, Z.-X. Cui, and W.-P. Lai, "The effect of microdroplet size on the surface tension and tolman length," *The Journal of Physical Chemistry B*, vol. 115, no. 1, pp. 109–112, 2011, PMID: 21155577. DOI: 10.1021/jp1084313. eprint: https://doi.org/10.1021/jp1084313.

[59] C. Amole *et al.*, "Data-driven modeling of electron recoil nucleation in PICO c_3f_8 bubble chambers," *Physical Review D*, vol. 100, no. 8, Oct. 2019. DOI: 10.1103/physrevd.100.082006.

[60] E. W. Lemmon, I. H. Bell, M. L. Huber, and M. O. McLinden, *NIST Standard Reference Database 23: Reference Fluid Thermodynamic and Transport Properties-REFPROP, Version 10.0, National Institute of Standards and Technology*, 2018. DOI: https://doi.org/10.18434/T4/1502528.

[61] L. Rayleigh, "On the pressure developed in a liquid during the collapse of a spherical cavity," *The London, Edinburgh, and Dublin Philosophical Magazine and Journal of Science*, vol. 34, no. 200, pp. 94–98, 1917. DOI: 10.1080/14786440808635681.

[62] M. S. Plesset and S. A. Zwick, "The growth of vapor bubbles in superheated liquids," *Journal of Applied Physics*, vol. 25, no. 4, pp. 493–500, 1954. DOI: 10.1063/1.1721668.

[63] T. Kozynets, S. Fallows, and C. B. Krauss, "Modeling emission of acoustic energy during bubble expansion in pico bubble chambers," *Physical Review D*, vol. 100, no. 5, 2019. DOI: 10.1103/physrevd.100.052001.

[64] C. Amole *et al.*, "Dark matter search results from the PICO-60 cf_3i bubble chamber," *Physical Review D*, vol. 93, no. 5, Mar. 2016. DOI: 10.1103/physrevd.93.052014.

[65] G. Giroux, "Search for dark matter with the pico-500 experiment," *Journal of Physics: Conference Series*, vol. 2156, no. 1, p. 012 068, Dec. 2021. DOI: 10.1088/1742-6596/2156/1/012068.

[66] D. Durnford and M.-C. Piro, "Nucleation efficiency of nuclear recoils in bubble chambers," *Journal of Instrumentation*, vol. 17, no. 01, 2022. DOI: 10.1088/1748-0221/17/01/c01030.

[67] B. Ali *et al.*, "Determining the bubble nucleation efficiency of low-energy nuclear recoils in superheated c_3f_8 dark matter detectors," *Physical Review D*, vol. 106, no. 12, 2022. DOI: 10.1103/physrevd.106.122003.

[68] S. Plimpton, A. Kohlmeyer, A. Thompson, S. Moore, and R. Berger, *Lammps stable release 29 september 2021*, Sep. 2021.

[69] J. R. Errington, P. G. Debenedetti, and S. Torquato, "Quantification of order in the lennard-jones system," *The Journal of Chemical Physics*, vol. 118, no. 5, pp. 2256–2263, 2003. DOI: 10.1063/1.1532344.

[70] G. A. Chapela, G. Saville, S. M. Thompson, and J. S. Rowlinson, "Computer simulation of a gas–liquid surface. part 1," *J. Chem. Soc., Faraday Trans. 2*, vol. 73, no. 7, pp. 1133–1144, 1977. DOI: 10.1039/f29777301133.

[71] D. Baxter *et al.*, "First demonstration of a scintillating xenon bubble chamber for detecting dark matter and coherent elastic neutrino-nucleus scattering," *Phys. Rev. Lett.*, vol. 118, p. 231 301, 23 Jun. 2017. DOI: 10.1103/PhysRevLett.118.231301.

[72] F. Theeuwes and R. J. Bearman, "The p, v, t behavior of dense fluids v. the vapor pressure and saturated liquid density of xenon," *The Journal of Chemical Thermodynamics*, vol. 2, no. 4, pp. 507–512, 1970. DOI: 10.1016/0021-9614(70)90100-x.

[73] J. F. Ziegler, M. Ziegler, and J. Biersack, "Srim – the stopping and range of ions in matter (2010)," *Nuclear Instruments and Methods in Physics Research Section B: Beam Interactions with Materials and Atoms*, vol. 268, no. 11-12, pp. 1818–1823, 2010. DOI: 10.1016/j.nimb.2010.02.091.

[74] J. T. Drobny and D. Curreli, "Rustbca: A high-performance binary-collision-approximation code for ion-material interactions," *Journal of Open Source Software*, vol. 6, no. 64, p. 3298, 2021. DOI: 10.21105/joss.03298.

[75] J. Lindhard and M. Scharff, "Energy dissipation by ions in the kev region," *Physical Review*, vol. 124, no. 1, pp. 128–130, 1961. DOI: 10.1103/physrev.124.128.

[76] C. E. Dahl, "The physics of background discrimination in liquid xenon, and first results from Xenon10 in the hunt for WIMP dark matter," Ph.D. dissertation, Princeton U., 2009.

[77] J. Lindhard, V. Nielsen, M. Scharff, and P. V. Thomsen, "Integral equations governing radiation effects. (notes on atomic collisions, iii)," *Kgl. Danske Videnskab., Selskab. Mat. Fys. Medd.*, Jan. 1963.

[78] A. Hitachi, A. Mozumder, and K. D. Nakamura, "Energy deposition on nuclear emulsion by slow recoil ions for directional dark matter searches," *Physical Review D*, vol. 105, no. 6, 2022. DOI: 10.1103/physrevd.105.063014.

[79] A. Hitachi, "Bragg-like curve for dark matter searches: Binary gases," *Radiation Physics and Chemistry*, vol. 77, no. 10-12, pp. 1311–1317, 2008. DOI: 10.1016/j.radphyschem.2008.05.044.

[80] M. Szydagis *et al.*, *Noble element simulation technique v2.0*, version v2.0.0, Jul. 2018. DOI: 10.5281/zenodo.1314669.

[81] P. Sorensen and C. E. Dahl, "Nuclear recoil energy scale in liquid xenon with application to the direct detection of dark matter," *Physical Review D*, vol. 83, no. 6, Mar. 2011. DOI: 10.1103/physrevd.83.063501.

[82] E. Behnke *et al.*, "Direct Measurement of the Bubble Nucleation Energy Threshold in a CF_3I Bubble Chamber," *Phys. Rev. D*, vol. 88, p. 021 101, 2013. DOI: 10.1103/PhysRevD.88.021101. arXiv: 1304.6001 [physics.ins-det].

[83] G. J. Feldman and R. D. Cousins, "Unified approach to the classical statistical analysis of small signals," *Physical Review D*, vol. 57, no. 7, pp. 3873–3889, Apr. 1998. DOI: 10.1103/physrevd.57.3873.

[84] C. Amole *et al.*, "Dark Matter Search Results from the PICO-60 C_3F_8 Bubble Chamber," *Phys. Rev. Lett.*, vol. 118, no. 25, p. 251 301, 2017. DOI: 10.1103/PhysRevLett.118.251301. arXiv: 1702.07666 [astro-ph.CO].

[85] V. Gluscevic, M. I. Gresham, S. D. McDermott, A. H. Peter, and K. M. Zurek, "Identifying the theory of dark matter with direct detection," *Journal of Cosmology and Astroparticle Physics*, vol. 2015, no. 12, pp. 057–057, Dec. 2015. DOI: 10.1088/1475-7516/2015/12/057.

[86] J. D. Lewin and P. F. Smith, "Review of mathematics, numerical factors, and corrections for dark matter experiments based on elastic nuclear recoil," *Astropart. Phys.*, vol. 6, pp. 87–112, 1996. DOI: 10.1016/S0927-6505(96)00047-3.

[87] V. Chepel and H. Araú jo, "Liquid noble gas detectors for low energy particle physics," *Journal of Instrumentation*, vol. 8, no. 04, R04001–R04001, Apr. 2013. DOI: 10.1088/1748-0221/8/04/r04001.

[88] T. Frédéric, "Direct detection of dark matter with the pico experiment and the pico-0.1 calibration chamber," Ph.D. dissertation, 2018.

[89] J. J. Aubert *et al.*, "Experimental observation of a heavy particle J," *Phys. Rev. Lett.*, vol. 33, pp. 1404–1406, 23 Dec. 1974. DOI: 10.1103/PhysRevLett.33.1404.

[90] M. F. Albakry *et al.*, "A Strategy for Low-Mass Dark Matter Searches with Cryogenic Detectors in the SuperCDMS SNOLAB Facility," in *Snowmass 2021*, Mar. 2022. arXiv: 2203.08463 [physics.ins-det].

[91] J. E. Kim and G. Carosi, "Axions and the strong CP problem," *Rev. Mod. Phys.*, vol. 82, pp. 557–601, 1 Mar. 2010. DOI: 10.1103/RevModPhys.82.557.

[92] B. W. Lee and S. Weinberg, "Cosmological lower bound on heavy-neutrino masses," *Phys. Rev. Lett.*, vol. 39, pp. 165–168, 4 Jul. 1977. DOI: 10.1103/PhysRevLett.39.165.